

**UNIVERSITY OF MISKOLC**  
**FACULTY OF MECHANICAL ENGINEERING AND INFORMATICS**



**THE IMPACT OF NANOPARTICLES ON THE FLUID FLOW  
PROPERTIES**

PH.D. THESES

Prepared by

**Mohamad Klazly**

Engineering of Mechanical and Electrical (BSc),  
Engineering of Mechanical and Manufacturing (MSc)

**ISTVÁN SÁLYI DOCTORAL SCHOOL OF MECHANICAL ENGINEERING SCIENCES**  
**TOPIC FIELD OF MECHANICAL ENGINEERING SCIENCES**  
**TOPIC GROUP OF DESIGN OF MACHINES AND ELEMENTS**

Head of Doctoral School

**Dr. Gabriella Vadászné Bognár**  
DSc, Full Professor

Head of Topic Group

**Dr. Gabriella Vadászné Bognár**

Scientific Supervisor

**Dr. Gabriella Vadászné Bognár**

**Miskolc**  
**2022.**

## CONTENTS

CONTENTS.....	I
SUPERVISOR'S RECOMMENDATIONS.....	III
LIST OF SYMBOLS AND ABBREVIATIONS.....	4
<b>1. INTRODUCTION .....</b>	<b>5</b>
1.1 BLASIUS FLOW.....	6
1.2 SAKIADIS FLOW.....	6
1.3 BACKWARD-FACING STEP NANOFLUID FLOW.....	7
1.4 THERMOPHYSICAL PROPERTIES OF NANOFLUIDS .....	9
1.5 DEVELOPMENT OF THE VISCOSITY MODELS .....	12
<b>2. MATHEMATICAL MODELING AND NUMERICAL SIMULATIONS.....</b>	<b>17</b>
2.1 THE EQUATION OF CONTINUITY .....	17
2.2 MOMENTUM EQUATION.....	17
2.3 ENERGY EQUATION.....	19
2.4 DISCRETIZATION.....	20
2.5 FINITE VOLUME METHOD (FVM).....	21
2.6 CFD CODE.....	21
<b>3. CFD MODELLING.....</b>	<b>23</b>
3.1 SINGLE-PHASE MODELS.....	23
3.1.1 NEWTONIAN SINGLE-PHASE MODEL.....	23
3.1.2 NON-NEWTONIAN SINGLE-PHASE MODEL.....	23
3.2 TWO-PHASE MODELS.....	24
3.2.1 MIXTURE MODEL.....	25
3.2.2 EULERIAN MODEL.....	26
3.2.3 VOLUME OF FLUID (VOF) MODEL .....	27
3.3 MODELLING THE THERMOPHYSICAL PROPERTIES OF NANOFLUIDS.....	28
3.3.1 CONSTANT THERMO-PHYSICAL PROPERTIES .....	28
3.3.2 TEMPERATURE-DEPENDENT THERMO-PHYSICAL PROPERTIES.....	29
<b>4. FLOW OVER FLATE PLATE (FLUID WITH CONSTANT PROPERTIES) .....</b>	<b>30</b>
4.1 SIMILARITY ANALYTIC SOLUTIONS.....	31
4.2 NUMERICAL PROCEDURE (CFD) .....	33
4.3 RESULTS .....	34
4.4 COMPARISON OF SIMILARITY AND CFD RESULTS.....	35
<b>5. SAKIADIS FLOW OF NANOFLUID .....</b>	<b>39</b>
5.1 SIMILARITY ANALYTIC SOLUTION.....	39
5.2 RESULTS .....	40
5.3 COMPARISON OF SIMILARITY AND CFD SOLUTIONS.....	45
<b>6. BACKWARD-FACING STEP (FLUID WITH TEMPERATURE-DEPENDENT PROPERTIES).....</b>	<b>48</b>
6.1 PROBLEM DESCRIPTION .....	48

---

6.2	<i>EXPERIMENTAL BACKGROUND</i> .....	49
6.3	<i>GOVERNING EQUATIONS</i> .....	50
6.4	<i>NUMERICAL PROCEDURE AND MESH INDEPENDENCE TEST</i> .....	50
6.5	<i>VALIDATION</i> .....	51
6.6	<i>TEMPERATURE-DEPENDENT PROPERTIES</i> .....	53
6.7	<i>PERFORMANCE EFFICIENCY INDEX</i> .....	64
<b>7</b>	<b>COMPARISON OF DIFFERENT NANOFLUID MODELINGS</b> .....	<b>66</b>
7.1	<i>NEWTONIAN AND NON-NEWTONIAN SINGLE-PHASE MODELS</i> .....	66
7.2	<i>COMPARISON OF CFD RESULTS WITH EXPERIMENTAL DATA</i> .....	72
	7.2.1 <i>RESULTS USING TEMPERATURE DEPENDENT THERMO-PHYSICAL PROPERTIES</i> ..	72
	7.2.2 <i>RESULTS USING CONSTANT THERMO-PHYSICAL PROPERTIES</i> .....	74
<b>8</b>	<b>A NEW VISCOSITY EQUATION FOR NANOFLUIDS</b> .....	<b>77</b>
8.1	<i>METHODOLOGY</i> .....	77
8.2	<i>RESULTS AND DISCUSSION</i> .....	81
	8.2.1 <i>WATER-BASED NANOFLUIDS</i> .....	82
	8.2.2 <i>EG -BASED NANOFLUIDS</i> .....	84
	8.2.3 <i>OTHER BASE FLUIDS</i> .....	88
8.3	<i>APPLICATION OF THE NEW MODEL IN NUMERICAL SIMULATION</i> .....	95
	<b>NEW SCIENTIFIC RESULTS OF THE THESES</b> .....	<b>97</b>
	<b>ACKNOWLEDGEMENTS</b> .....	<b>99</b>
	<b>REFERENCES</b> .....	<b>100</b>
	<b>LIST OF PUBLICATIONS RELATED TO THE TOPIC OF THE RESEARCH FIELD</b> .....	<b>109</b>

## SUPERVISOR'S RECOMMENDATIONS

PhD candidate Mohamed Klazly has been under my supervision for almost four years. Since September 2018, he has been pursuing his PhD studies at the Institute of Mechanical and Product Design at the Sályi István Sályi School of Mechanical Engineering, part of the Faculty of Mechanical Engineering and Informatics, under the "Stipendium Hungaricum" scholarship programme. His research work on the analysis of nanofluid flow conditions is a very important and active research area today due to its wide range of practical industrial applications.

As a novel strategy to improve heat transfer characteristics of fluids by the addition of nano sized solid particles, nanofluids exhibit unprecedented heat transfer properties and are being considered as potential working fluids to be used in high heat flux systems such as electronic cooling systems, solar collectors, heat pipes, and nuclear reactors.

His work involved a review and analysis of fundamental studies on nanofluids in areas such as thermophysical properties and heat transfer performance. At present, no agreement has been reached on a unified understanding of the mechanism underlying the heat enhancement of nanofluids.

For the analysis of fluid flow, CFD predictions of laminar flows were compared using two single-phase models (Newtonian and non-Newtonian) and three different two-phase models (Volume of Fluid, Mixture, Eulerian). The thermo-physical properties of the fluid were assumed to be either constant or temperature-dependent. Numerical predictions were compared with published experimental data to assess the accuracy of all five models.

The viscosity of nanofluids has received increasing attention in recent years. I consider the new viscosity equation obtained as one of the most outstanding results of the candidate.

The results of the candidate's research have been published and presented in scientific journals, doctoral seminars, doctoral forums and international conferences, as well as in conference proceedings. His publications have appeared in journals, such as the International Communication of Heat and Mass Transfer, the Alexandria Journal of Engineering, or, most recently, the Journal of Molecular Liquids. The work has room for extension, as additional questions that could not be answered within the scope of the PhD training were raised during the work and further results are in the process of being published.

In 2020, he successfully passed the complex examination. He obtained the pre-degree certificate with an outstanding 422.5 credits on 29 April 2022. He successfully passed the departmental discussion on 17 June 2022.

The candidate worked independently and very often took the initiative, always following instructions. During his doctoral studies he further developed his knowledge, research affinity and presentation skills. He has acquired new knowledge and competences which he will be able to use in his future academic life.

21 June 2022

Supervisor

**LIST OF SYMBOLS AND ABBREVIATIONS**

	<b>Nomenclature</b>				
$a$	Radii of the primary particles	nm	$n$	Power-law index	
$a_a$	Radii of the aggregates	nm	Nu	Nusselt number	
$c_1, c_2, c_3, c_4$	Constants		$Nu_x$	Local Nusselt number	
$C$	Correction factor		P	Pressure	Pa
$C_d$	drag coefficient		Pr	Prandtl number	
$C_f$	Skin friction coefficient		$r_p$	Radius of a particle	
$C_p$	Specific heat	J/kg.K	Re	Reynolds number	m
$d_p$	Nanoparticles' diameter	nm	$T$	Temperature	K
D	fractal index		$u$	Component of the $\vec{V}$ in the x-direction	m/s
$f$	Function		$v$	Component of the $\vec{V}$ in the y-direction	m/s
$f_{drag}$	drag function		$V$	Velocity vector	m/s
$F$	force	N	$V_B$	Brownian velocity	m/s
$F_{col}$	particle–particle interaction force	Pa m <sup>-1</sup>	$H$	Enthalpy	
$F_d$	drag force	Pa m <sup>-1</sup>	<b>Greek symbols</b>		
$F_{vm}$	virtual mass force	Pa m <sup>-1</sup>			
$g$	gravity acceleration	m/s <sup>2</sup>			
$h$	Inlet height	m	$\alpha_{nf}$	Thermal diffusivity	m <sup>2</sup> /s
$h_{av}$	Average heat transfer	W/m <sup>2</sup> .K	$\delta$	Distance between the nanoparticles	nm
$h_x$	Local heat transfer	W/m <sup>2</sup> .K	$\mu$	Intrinsic viscosity	Pa.s
$h_s$	Inter particle spacing	m	$\rho$	Density	kg/m <sup>3</sup>
H	Channel height	m	$\varphi$	Volume fraction	
$k$	Thermal conductivity	W/m. K	$\varphi_m$	Maximum particles packing fraction	
$K$	Consistency	Pa s <sup>n</sup>	$\tau$	Stress	Pa.s
$K_B$	Boltzmann constant		$\psi$	Stream function	
	<b>Subscripts</b>				
$b$	Base fluid		$nf$	Nanofluid	
$d$	Downstream wall		$p$	Solid particles	
$dynamic$	Dynamic viscosity		$Static$	Static viscosity	
$e$	Effective volume fraction				

## 1. INTRODUCTION

The traditional fluids (e.g., water, ethylene, oil, etc.) have limited heat transfer capabilities due to their poor thermo-properties such as relatively small thermal conductivity, which led researchers to try to overcome this barrier by improving the thermal conductivity of these fluids to have more efficient heat exchanger systems. The list of the industrial applications where better generation of heat transfer fluids could be utilized in for example, in hot rolling, drying of paper, biomedicine, food processing, nuclear reactors, etc. Generally, the thermal conductivity of metal particles is higher than that of the base fluid. Therefore, many techniques have been implemented to enhance the thermal performance of traditional fluids.

One of the early methods is via suspension of nanoparticles in the base fluid. The addition of particles of various materials that have higher thermal conductivity than the base fluid can enhance the thermal properties. This method was introduced by Cho [1], who coined the term nanofluid. Nanofluids have a bigger effective thermal conductivity due to the extremely large surface area of nanoparticles and leading them to be among the potential candidates considered in the heat transfer media. This thermal performance enhancement method has attracted considerable attention in a wide range of industrial applications and academic fields. The analysis of the thermo-physical properties of nanofluids includes several parameters, for instance: volume fraction, base fluid, nanoparticles size and shape, and particle migration patterns. All these parameters play vital role in the final nanofluid performance.

Nanofluid applications have attracted a significant number of researchers to investigate potential applications. Various applications have been examined in this way, including industrial, commercial, and transportation applications. Areas of application for these fluids are wide-ranging. They include functions such as engine cooling, electronic cooling, generator cooling, vehicle thermal management, nuclear system cooling, machining coolant, refrigeration, cooling, and heating in buildings, thermal storage, lubrication, solar heating, drug reduction, transformer cooling, heat pipes, biomedical applications, and maritime engineering. The aim of this thesis is to discuss nanofluid applications in boundary layers, microchannels, and heat exchangers as examples of its utilisation.

## 1.1 BLASIUS FLOW

The development of boundary layer theory was initiated by Ludwig Prandtl [2] in the early 1900s, and many world-renowned scientists, including Blasius [3], have worked on further development. The name “boundary layer” comes from Prandtl, and in this layer, we find a significant change in velocity close to the surface of a solid body. However, there is another type of boundary layer, and in addition to the change in velocity, a thermal boundary layer, which can also be defined based on temperature change. Prandtl’s theory led to the conclusion that usually the losses of fluid flowing in a pipe or duct occur almost entirely in a very thin boundary layer adhering to the wall. The analytical solution technique to the boundary layer problem comes from Blasius who introduced the similarity method [4].

Prandtl’s boundary layer theory has been applied to many practical engineering problems to predict skin friction drag. In metallurgical, petrochemical, and plastics processing applications, boundary layer theory is very important. The surface-driven flow in a fluid at rest plays an important role in many material processing processes, e.g., hot rolling, metalworking, and continuous casting [5].

The flow in the boundary layer of a plane moving at a uniform velocity in the Newtonian fluid was investigated analytically by Sakiadis [6]. His results were experimentally verified by Tsou et al. [7], and the continuous extrusion of polymer sheets from a die to the winding cylinder was investigated. The slit and the winding cylinder are placed at a finite distance from each other. Sakiadis assumed that after a certain period of time after the start of the process, a steady state is established. Tsou et al. [7] showed in their studies containing both analytical and experimental results that the laminar velocity field determined by the analytical solution for Newtonian fluid show an excellent agreement with the experimental data.

## 1.2 SAKIADIS FLOW

The Sakiadis problem of a fluid flow along sheet surfaces has been extended in many ways in recent decades. In the case of linear stretching, Crane [8] provided a solution to Sakiadis’ problem for heat and mass transfer in a closed form with an exponential function. Chakrabarti and Gupta [9] investigated flow characteristics over a linearly stretched surface through a transverse magnetic field. When the surface is stretched nonlinearly. The flow characteristics of non-Newtonian power law-type fluids over a stretched sheet were investigated by Bognár et al. [10],[11]. Haider et al. [12] analyzed magnetohydrodynamic viscous fluid flow due to exponentially stretching sheets with the homotopy analysis method. In [13], Mahabaleshwar examined the flow properties of fluid flow through porous media for a variety of boundary conditions. Among the different rheological models, the Walters-B

fluid model is applied for the description of the complex flow behavior of various polymer solutions. Andersson [14] investigated the Walters-B flow characteristics along a linearly stretching surface. In [15], Tonekaboni et al. solved the Walters-B Sakiadis boundary layer flow. An incompressible and electrically conducting isothermal viscoelastic Walters-B fluid flow due to a stretching surface with quadratic velocity was studied by Siddheshwar [16]. The boundary layer equations through a porous medium over a stretching plate with superlinear stretching velocity were investigated by Singh et al. [17]. The influence of variable viscosity is analyzed in heat and mass transfer properties in [18],[19].

### **1.3 BACKWARD-FACING STEP NANOFLUID FLOW**

One example of a separation flow model is the Backward-Facing Step (BFS) flow. It is a fundamental model that incorporates the essential characteristics of a separated flow: free shear flow separation, vortex evolution, and re-attachment. It has importance in both theoretical and engineering processes. Various BFS flow implementations in our everyday lives include airfoils with a high attack angle, spoiler flows, separation flow behind a car, engine inlet tunnel flow, or within a condenser/combustor and heat transfer systems [20] [21]. The flow separation near the BFS can cause additional flow resistance and noise and stalling of an aircraft under certain conditions. A general understanding of the physics in BFS flow has become a hot topic in recent years [22],[23]. Removing heat from system components and achieving a successful design for maximum cooling has become increasingly important as the size of the system components has shrunk, and the amount of heat generated by these devices has increased. New methods of thermal load management and optimization processes are necessary to meet the problem of maintaining optimal system equipment performance. The invention of the nanofluid compensated for the incapability of traditional fluids, such as water, in critical heat flux situations. Choi [1] was the first to propose the novel concept of mixing metallic and non-metallic nano-powders into a base fluid, which has several possible benefits, including increased heat transfer and smaller heat transfer systems. When studying the fundamental physical mechanisms of fluid flow and heat transfer, several factors are considered: sizing effect, rarity effects, surface roughness, viscous effect, axial heat conduction in the channel wall, surface geometry, and measurement errors, and heat transfer in a microchannel. The published findings are not always consistent, and many questions about nanofluid properties and behavior in particular systems remain unanswered. One of these concerns is the proper modeling of nanofluids in CFD. Studies focus primarily on the heat transfer of such fluids. The numerical analysis of heat convection transfer can be divided into single-phase and two-phase methods.



The single-phase method considers the nanofluid to be homogeneous with zero relative velocity and thermal equilibrium between the particles and base liquid [24][25],[26]. This model has been used to study the laminar and turbulent flow of  $\text{Al}_2\text{O}_3$  with water base fluid and ethylene glycol nanofluids [27]. Compared to the experimental result, the numerical results reported a reasonable agreement with a maximum error of 10%. The magnetized micropolar nanofluid flow over a stretching surface in Porous Media. A detailed parametric study on stream function, velocity, microrotation, temperature, and nanoparticle concentration using a single-phase model was reported in [28]. The laminar and steady flow of hybrid  $\text{Al}_2\text{O}_3$ –Cu water nanofluid for the volume fraction of solid nanoparticles 0–2% in a double-layered microchannel with sinusoidal walls. [29]. The unique properties of the mixture, such as volume fraction, base fluid type, diameter, and shape of the nanoparticles, influence the nanofluid modeling [30],[31]. Several studies have shown that nanofluids have non-Newtonian properties concerning the power law of shear-thinning performance [32]. The non-Newtonian rheology is presented in the power-law model with a flow index of less than 1. The relationship between shear stress and the rate has been experimentally documented by Putra et al. [33] for  $\text{Al}_2\text{O}_3$ –water nanofluid. Many researchers have applied the power-law model in numerical works [32], [34]. Rahmati et al. [35] investigated the non-Newtonian slip flow of CMC–water nanofluid in a two-dimensional microtube using a single-phase method. They reported that the increase in volume fraction of nanoparticles and the slip length greatly influence the heat transfer rate. Z. Li et al. [36] studied power-law for non-Newtonian with the two-phase method in a porous H-shaped cavity. They reported that using the two-phase method with power-law indexes shows completely acceptable results.

CFD simulations for nanofluids have concentrated on considering a two-phase flow. Only a few studies have compared the effects of single-phase and two-phase models. Lotfi et al. [37] compared the predictions of the single-phase model with two-phase models for  $\text{Al}_2\text{O}_3$ –water nanofluid with a 1% volume fraction. They compared the Nusselt number predictions to several correlations and experimental values from Wen and Ding [38] and concluded that the Mixture model is more accurate than the other two models.

Also, Akbari et al. [39] reported that the two-phase approaches better agree with experimental results for laminar mixed convection with low particle volume fraction and temperature-dependent density and viscosity. According to their findings, the two-phase models would predict unreasonably high heat transfer coefficients with moderate and large particle volume fractions. The rate of increase of the heat transfer coefficient with particle volume fraction predicted by two-phase models is significantly higher than the corresponding experimental value.

Behzadmehr et al. [40] investigated the behavior of Cu–water nanofluid in a tube with a two-phase mixture model. The authors stated that the models which assume that the base fluid and particles behave separately produced more accurate results than a single-phase method.

## **1.4 THERMOPHYSICAL PROPERTIES OF NANOFLUIDS**

Nanofluids are a new type of thermal fluids that are produced by dispersing nanoscale particles in a base fluid. Chemical processing, automobiles, air conditioning, solar panel, and power generation are all examples of heat transfer and fluid flow applications. In various industrial practices, water, oil, and ethylene/propylene glycol are common thermal fluids used in many engineering applications, including power generation, electronics applications, air conditioning, chemical manufacturing processes, heating, cooling operations, nuclear power system cooling, military, transport, and microelectronic applications. These liquids have poor thermal properties compared to solids. Nanofluids have aroused great interest as they show promising results in improving heat transfer. The properties of fluids are described by four main parameters: viscosity, thermal conductivity, density, and specific heat capacity. Nanofluids' viscosity and rheological properties are extremely important due to thermal and energetic applications. In practice, viscosity is the main cause of pressure drop and pumping performance. Forced convective heat transfer plays a major role in heat exchange applications with the nanofluid flow. The improvement of forced convective heat transfer can reduce the energy loss and hence scale down the size of a system. The effectiveness of heat exchangers is estimated by the non-dimensional Colburn  $j$  factor. Determining the viscosity of a nanofluid can significantly affect dimensionless and dynamic parameter numbers such as the Reynolds number, the Prandtl number, the Brinkman number, and the Rayleigh number used in numerical analysis studies of thermal and fluid dynamics research. As a result, accurate statistics on the effective viscosity of nanofluids are essential for industrial nanofluid applications. The effective viscosity is influenced by the viscosity of the base fluid and several parameters.

### **1.4.1 THE EFFECT OF BASE FLUID**

In this section, we shall consider water, ethylene glycol, and some other fluids as the base fluid for nanofluids.

#### **1.4.1.1 Water**

Several studies have suggested water as a base fluid since the addition of nanoparticles to water affects the thermo-physical properties of water. The effect of different nanoparticles on water has been

extensively studied; e.g., Nguyen et al. [41] investigated the effect of  $\text{Al}_2\text{O}_3$  particle concentration on the dynamic viscosity of water with particle diameters of 36 and 47 nm. They showed that the dynamic viscosity of nanofluids increased significantly from 1% to 9.4% with particle volume fraction, but the temperature decreased with an increase in the range of 295–348 K. The nanofluid volume concentration of  $\text{TiO}_2$  in water showed a similar result (0.2–2%) [42]. Esfe et al. [43] studied the thermo-physical properties of MWCNT-water, including dynamic viscosity, measured at different temperatures and volume fractions, and showed that an increase in the volume fraction of the nanofluid results enhancement in the heat transfer and effective viscosity. A suspension of  $\text{Fe}_3\text{O}_4$  and  $\text{MgO}$  nanoparticles in water as base fluid was also considered, and their viscosity was found to increase on increasing concentration of the nanoparticles (see [44], [45]).

#### 1.4.1.2 Ethylene glycol (EG)

Lee et al. [46] examined the viscosity of ZnO-EG nanofluids with particles size less than 100 nm. The results reported that ZnO-EG nanofluids show a Newtonian behaviour in the small volume fraction ( $\phi \leq 0.05$ ) and the effective viscosity increases with increasing particle concentration. Another experiment on the rheological behavior of copper nanoparticles suspended in EG with a volume fraction of 0 to 2 % shows that an increase in the volume fraction increases the effective viscosity (see [47]). Esfe et al. [48] showed that for the dynamic viscosity of Fe-EG normalized to the viscosity of an EG-based fluid with a particle size of 35–45 nm at 328 K, an increase in volume fraction results in an increase in effective viscosity.

#### 1.4.1.3 Other base fluids

The effect of particle concentration and temperature on the viscosity of nanofluids composed of magnetite nanoparticles dispersed in toluene was investigated by Singh [49]. The viscosity of these nanofluids increases with increasing particle concentration. The impact of iron volume concentration (0–0.5%) in a temperature range of 298–338 K was presented, and the results showed that the viscosity of nanofluids with 0.5% iron was improved as compared to the base fluid and the viscosity significantly decreased while the temperature of the nanofluid increased. Li et al. [50] studied a mixture of 60% water and 40% EG to find the benefits of using two different conventional heat transfer fluids to improve the performance of the energy system. They presented experimental data on the viscosity properties of SiC-EG-water in the ration 60:40 with a particle size of 30 nm. Their finding for viscosity was that the nanofluid behaves as a Newtonian fluid and the viscosity decreases with increasing temperature. The viscosity of  $\text{Al}_2\text{O}_3$ -propylene glycol (PG) was investigated in [51]. Experimental results on viscosity at

different shear rates, temperatures, nanoparticle diameters, and concentrations have been reported, and it has been found that viscosity increases with increasing particle concentration. Copper oxide nanofluids based on coconut oil have been studied in [12]. It has been reported that the viscosity of nanofluid increases with the loading of nanoparticles and decreases exponentially with increasing temperature. The viscosity of CuO-gear oil nanofluids was studied by Kole and Dey [53]. The effect of CuO nanoparticles on the viscosity of nanofluids in the different volume fractions (0.5-2.5%) and temperature range 283 to 353 K has been shown. The results of the study showed that the viscosity of nanofluids of CuO with a volume fraction of 0.025 improved to about three times that of the base fluid but decreased greatly with increasing temperature.

#### **1.4.2 THE EFFECT OF VOLUME FRACTION**

The most important component of any nanofluid mixture is the concentration of the nanoparticles, which directly affects the effective viscosity of the nanofluids. Several studies have shown that the viscosity of nanofluids increases with increasing particle concentration due to the weight percentage of nanoparticles.

#### **1.4.3 THE EFFECT OF SHEAR RATE**

Shear rate is another factor that can affect the viscosity of non-Newtonian nanofluids. Halelfadl et al. [54] investigated experimentally the viscosity of carbon nanotubes in water-based nanofluids. The results showed that nanofluids have a shear-thinning property under high particle loading. Nanofluids behaved like Newtonian fluids at lower particle concentrations. The ratio of the nanofluid viscosity to the viscosity of the base fluid at high shear rates is almost unaffected by temperature. The effect of shear rate on the viscosity of Fe<sub>3</sub>O<sub>4</sub>-MWCNTs/EG was investigated by Ahmad et al. [55]. The results showed that low volume concentration nanofluids have Newtonian behaviour. Non-Newtonian behaviour is observed at higher volume concentrations of Fe<sub>3</sub>O<sub>4</sub>-MWCNT/EG. The effect of shear rate on the viscosity of EG-based nanofluids containing ZnO nanoparticles was investigated by Yu et al. [56]. ZnO-EG nanofluids with low volume fractions show Newtonian behaviour. At higher volume fractions (greater than 3%), ZnO-EG nanofluids are non-Newtonian.

#### **1.4.4 THE EFFECT OF MORPHOLOGY AND PARTICLE SIZE**

Both the shape and size of the nanoparticles can affect the viscosity and pumping power of the cooling system. Chevalier et al. [57] found that the decrease in nanoparticle size increased the effective viscosity. Three different SiO<sub>2</sub>-water nanoparticle diameters were considered: 35, 94, and 190 nm. The stability and dispersion of nanofluids prepared by dispersing CuO nanoparticles in water have been

studied. It has been found that the effect of particle size on density is small but not negligible, but the differences in viscosity are very large and should be taken into account in all practical applications [58].

#### 1.4.5 THE EFFECT OF TEMPERATURE

Temperature is one of the most important parameters influencing viscosity. Based on the experimental results, several models have been proposed, but few models can be used to measure the approximate viscosity of nanofluids. Table 1.1 lists the models of nanofluid viscosity for different nanofluids derived by various authors considering the volume fraction and temperature

Based on previous studies, the viscosity of nanofluid increases significantly with increasing particle concentration and decreases with increasing temperature. Nanoparticle types and base fluids affect the viscosity of the nanofluid. Analysis of several experimental studies shows that the governing viscosity equations consistently underestimate the effective viscosity. There is a big difference between the theoretical and experimental values. Many factors were not taken into account. One such factor is the Brownian motion. Experimental viscosity models are currently of limited use. In chapter 7 we shall return to reduce the limitations of existing formulas using regression analysis based on experimental and theoretical data available in the literature.

### 1.5 DEVELOPMENT OF THE VISCOSITY MODELS

Among the theoretical formulas used to estimate the particle suspension in the base fluid, Einstein's equation was the first on the rheological behaviour of a nanofluid containing dilute, suspended microparticles with low (0-2%) volume fraction and spherical shape. The limitation of the model is that Einstein did not consider the interaction of particles in the suspensions. This phenomenon may have a significant effect at a higher volume fraction, and the interaction of the particles may affect the viscosity of the nanofluid. Einstein's formula is written as [59]

$$\frac{\mu_{nf}}{\mu_b} = 1 + \mu \varphi, \quad (1.1)$$

and equation (1.1) becomes as

$$\frac{\mu_{nf}}{\mu_b} = 1 + 2.5 \varphi. \quad (1.2)$$

Several studies have suggested taking into account the hydrodynamic interaction caused by higher concentrations in suspension. In 1952, Brinkman generalized the Einstein correlation to higher concentrations. The underlying formula is also valid only for low (0-4%) particle volume fractions [60] and is given by

$$\frac{\mu_{nf}}{\mu_b} = \frac{1}{(1-\varphi)^{2.5}}. \quad (1.3)$$

In 1959, Krieger and Dougherty [61] derived the following semi-empirical relation for the viscosity covering the full range of particle volume fractions:

$$\frac{\mu_{nf}}{\mu_b} = \left(1 - \left(\frac{\varphi}{\varphi_m}\right)\right)^{-[\mu]\varphi_m}. \quad (1.4)$$

Chen et al. [62] proposed to modify equation (4) in the form

$$\frac{\mu_{nf}}{\mu_b} = \left(1 - \left(\frac{\varphi_a}{\varphi_m}\right)\right)^{-2.5 \varphi_m}, \quad (1.5)$$

$$\varphi_a = \varphi \left(\frac{a_a}{a}\right)^{3-D}. \quad (1.6)$$

In 1967, Frankel and Acrivos [63] proposed the following correlation:

$$\frac{\mu_{nf}}{\mu_b} = \frac{9}{8} \left[ \frac{\left(\frac{\varphi}{\varphi_m}\right)^{\frac{1}{3}}}{1 - \left(\frac{\varphi}{\varphi_m}\right)^{\frac{1}{3}}} \right]. \quad (1.7)$$

In 1972, a formula based on Taylor series as a function of  $\varphi$  was introduced by Lundgren [64]. The equation is referred to the reduction of Einstein's formula:

$$\frac{\mu_{nf}}{\mu_b} = 1 + 2.5\varphi + \frac{25}{5}\varphi^2 + f(\varphi^3), \quad (1.8)$$

In 1977, Batchelor [65] studied the interaction of particle pairs and the effect of Brownian motion of rigid and spherical particles on a nearly isotropic suspension of rigid and spherical particles and developed the following relation:

$$\frac{\mu_{nf}}{\mu_b} = 1 + 2.5\varphi + 6.5 \varphi^2. \quad (1.9)$$

Graham [66] generalized the formula given by Frankel and Acrivos [63] in 1981. A correlation has been shown for the low concentrations developed by Einstein as follows:

$$\frac{\mu_{nf}}{\mu_b} = 1 + 2.5\varphi + 4.5 \left[ \left(\frac{h_p}{d_p}\right) \left(2 + \frac{h_p}{d_p}\right) \left(1 + \frac{h_p}{d_p}\right)^2 \right]^{-1}, \quad (1.10)$$

In 1999, Wang et al. [67] expressed a model to predict the viscosity of nanofluids as follows:

$$\frac{\mu_{nf}}{\mu_b} = (1 + 7.3 \varphi + 123 \varphi^2). \quad (1.11)$$

In 2007, the relationship between normalized shear viscosity and the viscosity of a 0-10% nanofluid was studied and was introduced by regression of experimental data by Tseng et al. [68]:

$$\frac{\mu_{nf}}{\mu_b} = 1 + 10.6 \varphi + 10.6 \varphi^2. \quad (1.12)$$

In 2007, Nguyen et al. [69] have shown that both the Brinkman and Batchelor formulas severely underestimate the viscosity of the nanofluid, except for very low particle volume fractions of less than 1%. These models give very low values compared to the experimental results. Thus, two separate correlations have been proposed for water-based nanofluids of  $\text{Al}_2\text{O}_3$  nanoparticles with 47 nm and 36 nm as follows:

$$\frac{\mu_{nf}}{\mu_b} = 1 + 0.025 \varphi + 0.015 \varphi^2 \quad \text{for } d_p=47\text{nm}, \quad (1.13)$$

$$\frac{\mu_{nf}}{\mu_b} = 0.904e^{0.148\varphi} \quad \text{for } d_p=36\text{nm}. \quad (1.14)$$

Avsec and Oblac [70] derived a mathematical model for calculating nanofluids viscosity with the help of the exponential formula of Cheng and Law [71],

$$\frac{\mu_{nf}}{\mu_b} = 1 + 2.5\varphi_e + 2.5 \varphi_e^2 + 2.5\varphi_e^3 + 2.5\varphi_e^4, \quad (1.15)$$

where the effective volume fraction is calculated as

$$\varphi_e = \varphi \left(1 + \frac{h}{r}\right)^3 \quad (1.16)$$

Masoumi et al. [72] developed a new theoretical model for predicting the viscosity of nanofluids taking into account Brownian motion. With this model, the effective viscosity can be calculated based on temperature  $T$ , average particle diameter  $d_p$ , nanoparticle volume fraction  $\varphi$ , nanoparticle density  $\rho_p$ , and physical properties of the base fluid. With this model, the viscosity of a fluid consisting of two different fluids can also be predicted, and we have

$$\frac{\mu_{nf}}{\mu_b} = 1 + \frac{\rho_p V_B d_p^2}{72\delta C}, \quad (1.17)$$

where the  $V_B$ ,  $\delta$  and  $C$  are defined as

$$V_B = \frac{1}{d_p} \sqrt{\frac{18K_b T}{\pi \rho_p d_p}}, \quad (1.18)$$

$$\delta = \sqrt[3]{\frac{\pi}{6\varphi}} d_p, \quad (1.19)$$

$$C = [(c_1 d_p - c_2)\varphi + (c_3 d_p - c_4)]. \quad (1.20)$$

Masoumi et al. [72] gave the correction factor  $C$  for a very limited number of experimental data (for eight data), and the formula is limited for

$$\varphi < \frac{c_3 d_p - c_4}{c_1 d_p - c_2}. \quad (1.21)$$

Table 1.2 presents a list of viscosity models for different nanofluids, which depend on volume fractions.

Table 1.1 Viscosity correlations as a function of volume fraction and temperature

Author	Nanoparticle types	Base fluid	Viscosity correlations	Temperature range [K]
Kulkarni et al. [73]	CuO	Water-EG	$\ln \mu_{nf} = -(2.8751 + 53.548 \varphi - 107.12 \varphi^2) + (1078.3 + 15857 \varphi + 2087 \varphi^2) T^{-1}$	278–323
Namburu et al. [74]	CuO, Al <sub>2</sub> O <sub>3</sub> and SiO <sub>2</sub>	Water - EG	$\log \mu_{nf} = Ae^{-BT}$	238-323
Karimipour et al. [75]	CuFe <sub>2</sub> O <sub>4</sub> /SiO <sub>2</sub>	Water - EG	$\frac{\mu_{nf}}{\mu_{bf}} = 43947802.6097 \varphi^{3.3239} T^{-1.2107} + 22.7550 T^{-0.5891} - 0.9317$	303-323
Akbari et al. [76]	SiO <sub>2</sub>	EG	$\frac{\mu_{nf}}{\mu_{bf}} = -24.81 + 3.23 T^{0.08014} \exp(1.838 \varphi^{0.002334}) - 0.0006779 T^2 + 0.024 \varphi^3$	303-323
Alrashed et al. [77]	CuFe <sub>2</sub> O <sub>4</sub> /SO <sub>2</sub>	Water	$\mu_{nf} = 233.2713 \varphi^{0.8623} T^{-0.08263} - 2.6698 \varphi^{0.4821} + 0.9145$	303-323
Ghasemi et al. [78]	CuO	Water	$\frac{\mu_{nf}}{\mu_{bf}} = -1.735 T^{-0.017} - 0.027 \varphi^{0.418} + 0.039 \varphi^{1.543} T^{-0.033} + 2.956$	283-373
Abu-Nada [79]	Al <sub>2</sub> O <sub>3</sub>	Water	$\frac{\mu_{nf}}{\mu_{bf}} = -0.155 - 19.582 T^{-1} + 0.794 \varphi + 209447 T^{-2} + 0.192 \varphi^2 - 8.11 \varphi T^{-1} - \frac{27463}{T^2} + 0.0127 \varphi^3 + 1.6044 \varphi^2 T^{-1} + 2.175 \varphi T^{-2}$	294-343
Toghraie et al. [44]	Fe <sub>3</sub> O <sub>4</sub>	Water	$\frac{\mu_{nf}}{\mu_{bf}} = 1.01 + (0.007165 T^{1.171} \varphi^{1.509}) \exp(-0.00719 T \varphi)$	293-328
Esfe et al. [80]	Fe	Water	$\frac{\mu_{nf}}{\mu_{bf}} = 1 + (0.1008 \times \varphi^{0.69574} \times d_p^{0.44708})$	dp=37-98nm
Azmi et al [81]	Al <sub>2</sub> O <sub>3</sub> , CuO	Water	$\frac{\mu_{nf}}{\mu_{bf}} = C_1 \left(1 + \frac{\phi}{100}\right)^{11.3} \left(1 + \frac{T_{nf}}{70}\right)^{-0.038} \left(1 + \frac{d_p}{170}\right)^{-0.061}$	273-373
Khanafer and Vafai [82]	Al <sub>2</sub> O <sub>3</sub>	Water	$\frac{\mu_{nf}}{\mu_{bf}} = -0.4491 + \frac{28.837}{T} + 0.574 \varphi - 0.1634 \varphi^2 + 23.053 \frac{\varphi^2}{T^2} + 0.0132 \varphi^3 - 2354.735 \frac{\varphi}{T^3} + 23.498 \frac{\varphi^2}{d_p^2} - 3.0185 \frac{\varphi^3}{d_p^2}$	283-343 d <sub>p</sub> =13-131 nm



Table 1.2. Viscosity models for different nanofluids

	Author	Year	Viscosity formula	Theo/ Exp.	Notes	$\varphi$
1	Einstein [59]	1906	$\frac{\mu_{nf}}{\mu_{bf}} = 1 + 2.5 \varphi$	Theoretical	Infinitely suspension	<2%
2	De Bruijn [83]	1942	$\frac{\mu_{nf}}{\mu_{bf}} = 1 + 2.5\varphi + 4.698\varphi^2$	Theoretical	Spherical nanoparticles	0-7%
3	Vand [84]	1948	$\frac{\mu_{nf}}{\mu_{bf}} = 1 + 2.5\varphi + 7.349 \varphi^2$	Theoretical	Spherical nanoparticles	NA
4	Saito [85]	1950	$\frac{\mu_{nf}}{\mu_{bf}} = 1 + 2.5\varphi + 2.5 \varphi^2$	Theoretical	Spherical particles	<2.5%
5	Brinkman [60]	1952	$\frac{\mu_{nf}}{\mu_{bf}} = (1 - \varphi)^{-2.5}$	Theoretical	Spherical particles	<2%
6	Lundgren [64]	1972	$\frac{\mu_{nf}}{\mu_{bf}} = (1 - 2.5 \varphi)^{-1}$	Theoretical	Dilute Concentration	0-3%
7	Batchelor [65]	1977	$\frac{\mu_{nf}}{\mu_{bf}} = 1 + 2.5\varphi + 6.5 \varphi^2$	Theoretical	Rigid and spherical particles	0-2%
8	Drew and Passman [86]	1999	$\frac{\mu_{nf}}{\mu_{bf}} = 1 + 2.5 \varphi$	Theoretical	Al <sub>2</sub> O <sub>3</sub> - TiO <sub>2</sub> . CuO	5%
9	Buongiorno[87]	2006	$\frac{\mu_{nf}}{\mu_{bf}} = 1 + 5.45\varphi + 108.2 \varphi^2$	Theoretical	TiO <sub>2</sub> -water	1-3%
10	Maiga et al. [27]	2005	$\frac{\mu_{nf}}{\mu_{bf}} = 1 - 0.19\varphi + 306\varphi^2$	Numerical	Al <sub>2</sub> O <sub>3</sub> / EG	0-8%
11	Pak and Cho [88]	1998	$\frac{\mu_{nf}}{\mu_{bf}} = 1 + 39.11 \varphi + 533.9 \varphi^2$	Experimental	Al <sub>2</sub> O <sub>3</sub> /TiO <sub>2</sub> /water	0-7.5%
12	Wang and Xu [67]	1999	$\frac{\mu_{nf}}{\mu_{bf}} = 1 + 7.3\varphi + 123 \varphi^2$	Experimental	CuO/ Al <sub>2</sub> O <sub>3</sub> -water	<10%
13	Prasher et al. [51]	2006	$\frac{\mu_{nf}}{\mu_{bf}} = 1 + 56.5\varphi$	Experimental	SiO <sub>2</sub> -water	NA
14	Nguyen et al. [69]	2007	$\frac{\mu_{nf}}{\mu_{bf}} = 1 + 0.025\varphi + 0.015 \varphi^2$	Experimental	Al <sub>2</sub> O <sub>3</sub> /d=36 nm	0-14%
15	Nguyen et al. [69]	2007	$\frac{\mu_{nf}}{\mu_{bf}} = 1.475 - 0.319\varphi + 0.051\varphi^2 + 0.009\varphi^3$	Experimental	CuO-water	0-14%
16	Chen et al. [62]	2007	$\frac{\mu_{nf}}{\mu_{bf}} = 1 + 10.6\varphi + 112.36 \varphi^2$	Experimental	TiO <sub>2</sub> -EG	0-8%
17	Grag et al. [89]	2008	$\frac{\mu_{nf}}{\mu_{bf}} = 1 + 11\varphi$	Experimental	Cu-EG	0-10%
18	Rea et al. [90]	2009	$\frac{\mu_{nf}}{\mu_{bf}} = 1 + 46.801\varphi + 550.82\varphi^2$	Experimental	Zirconia-water	0-3%
19	Esfe et al. [91]	2014	$\frac{\mu_{nf}}{\mu_{bf}} = 1 + 3.575 \varphi + 6032.93\varphi^2 - 1153669\varphi^3$	Experimental	DWCNTs/water	0-0.04%
20	Esfe et al. [45]	2014	$\frac{\mu_{nf}}{\mu_{bf}} = 1 + 11.61 \varphi + 109 \varphi^2$	Experimental	MgO (40nm)-water	0-1%
21	Li and Zou [50]	2016	$\frac{\mu_{nf}}{\mu_{bf}} = 1 + 2.5\varphi_v + 6.5 \varphi_v^2$	Experimental	SiC-EG-water	0-1%

## 2. MATHEMATICAL MODELING AND NUMERICAL SIMULATIONS

In this chapter, the mathematical models and the numerical approaches employed in the present research are discussed. The governing equations of the flow, the numerical code, and the CFD solution method will be presented. The geometry creation and the mesh generation are also reported. A built-in C-code incorporated in the CFD code is used. This C-code is known as a user-defined function (UDF). Computational Fluid Dynamic (CFD) is a robust tool for the analysis of systems comprising external or internal fluid flow and heat transfer. The analysis is made by computer-based simulation with higher accuracy. This method has been extended to a wide range of applications, such as aerodynamics, combustion, environment, medicine, agriculture, and many other applications. The mathematical formulation of the underlying flow problem is described through the governing equations of fluid flow and heat transfer [92], [93]. The equations of conservation laws can be summarized in the following subsections.

### 2.1 THE EQUATION OF CONTINUITY

The equation of continuity results from applying the law of conservation of mass to the control volume of the fluid and is given by

$$\frac{\partial \rho}{\partial t} + \nabla \cdot (\rho \mathbf{V}) = 0, \quad (2.1)$$

where  $\rho$  is the density and  $\mathbf{V}$  is the velocity of the fluid.

Using the Lagrangian approach, equation (2.1) can be written as:

$$\frac{D\rho}{Dt} + \rho(\nabla \cdot \mathbf{V}) = 0. \quad (2.2)$$

For incompressible flow  $\frac{D\rho}{Dt} = 0$ , and (2.2) can be mathematically written:

$$(\nabla \cdot \mathbf{V}) = 0. \quad (2.3)$$

Alternatively, it can be simplified in the Cartesian coordinate system to:

$$\frac{\partial u}{\partial x} + \frac{\partial v}{\partial y} + \frac{\partial w}{\partial z} = 0. \quad (2.4)$$

### 2.2 MOMENTUM EQUATION

The momentum equation can be obtained by applying Newton's second law of motion on a fluid passing an infinitesimal control volume, and is given by

$$\frac{\partial}{\partial t}(\rho \mathbf{V}) + \nabla \cdot \rho \mathbf{V} \mathbf{V} = \rho \mathbf{f} + \nabla \cdot \mathbf{P}_{ij}, \quad (2.5)$$

where  $\frac{\partial}{\partial t}(\rho \mathbf{V})$  denotes the rate of increase of momentum in the control volume. The rate of momentum per unit volume lost by convection is represented by the second term in the equation and can be expressed as:

$$\nabla \cdot \rho \mathbf{V} \mathbf{V} = \rho \mathbf{V} \cdot \nabla \mathbf{V} + \mathbf{V}(\nabla \cdot \rho \mathbf{V}). \quad (2.6)$$

Substituting this term in equation (2.5), the momentum equation can be simplified to the following form:

$$\rho \frac{D\mathbf{V}}{Dt} = \rho \mathbf{f} + \nabla \cdot \mathbf{P}_{ij}, \quad (2.7)$$

where  $\rho \mathbf{f}$  denotes the body force per unit volume of the fluid,  $\mathbf{V}(\nabla \cdot \rho \mathbf{V})$  is the surface force per unit volume. These forces are resulted from the external stresses to the fluid element.

In Newtonian fluids, the relation between the stress tensor and pressure and velocity can be written as:

$$P_{ij} = -p\delta_{ij} + \mu \left( \frac{\partial u_i}{\partial x_j} + \frac{\partial u_j}{\partial x_i} \right) + \delta_{ij} \mu' \frac{\partial u_k}{\partial x_k}, \quad (2.8)$$

where  $i, j, k = 1, 2, 3$ , and  $u_1, u_2, u_3$  are the three components of the velocity vector  $\mathbf{V}$ ,  $x_1, x_2, x_3$  represent the three components of the position vector;  $\delta_{ij}$  is the Kronecker delta function.  $\mu$  represents the coefficient of dynamic viscosity.  $\mu'$  is the second coefficient of viscosity. The Navier-Stokes equation can be written as:

$$\rho \frac{D\mathbf{V}}{Dt} = \rho \mathbf{f} - \nabla p + \frac{\partial}{\partial x_j} \left[ \mu \left( \frac{\partial u_i}{\partial x_j} + \frac{\partial u_j}{\partial x_i} \right) - \frac{2}{3} \delta_{ij} \mu' \frac{\partial u_k}{\partial x_k} \right]. \quad (2.9)$$

In the Cartesian coordinate system, the Navier-Stokes equation can be written in three different scalar equations [94]:

$$\rho \frac{Du}{Dt} = \rho f_x - \frac{\partial p}{\partial x} + \frac{\partial}{\partial x} \left[ \frac{2}{3} \mu \left( 2 \frac{\partial u}{\partial x} - \frac{\partial v}{\partial y} - \frac{\partial w}{\partial z} \right) \right] + \frac{\partial}{\partial y} \left[ \mu \left( \frac{\partial u}{\partial y} + \frac{\partial v}{\partial x} \right) \right] + \frac{\partial}{\partial z} \left[ \mu \left( \frac{\partial w}{\partial x} + \frac{\partial u}{\partial z} \right) \right], \quad (2.10)$$

$$\rho \frac{Dv}{Dt} = \rho f_y - \frac{\partial p}{\partial y} + \frac{\partial}{\partial y} \left[ \frac{2}{3} \mu \left( 2 \frac{\partial v}{\partial y} - \frac{\partial u}{\partial x} - \frac{\partial w}{\partial z} \right) \right] + \frac{\partial}{\partial x} \left[ \mu \left( \frac{\partial v}{\partial x} + \frac{\partial u}{\partial y} \right) \right] + \frac{\partial}{\partial z} \left[ \mu \left( \frac{\partial v}{\partial z} + \frac{\partial w}{\partial y} \right) \right], \quad (2.11)$$

$$\rho \frac{Dw}{Dt} = \rho f_z - \frac{\partial p}{\partial z} + \frac{\partial}{\partial z} \left[ \frac{2}{3} \mu \left( 2 \frac{\partial w}{\partial z} - \frac{\partial u}{\partial x} - \frac{\partial v}{\partial y} \right) \right] + \frac{\partial}{\partial x} \left[ \mu \left( \frac{\partial w}{\partial x} + \frac{\partial u}{\partial z} \right) \right] + \frac{\partial}{\partial y} \left[ \mu \left( \frac{\partial v}{\partial z} + \frac{\partial w}{\partial y} \right) \right]. \quad (2.12)$$

For incompressible flow and constant viscosity equation (2.9) can be simplified to:

$$\rho \frac{D\mathbf{V}}{Dt} = \rho \mathbf{f} + \nabla p + \mu \nabla^2 \mathbf{V}. \quad (2.13)$$

### 2.3 ENERGY EQUATION

The energy equation can be obtained by applying the first law of thermodynamics to a fluid passing through an infinitesimal control volume. Mathematically we have

$$\frac{\partial E_t}{\partial t} + \nabla \cdot \mathbf{E}_t \mathbf{V} = \frac{\partial Q}{\partial t} - \nabla \cdot \mathbf{q} + \rho \mathbf{f} \cdot \mathbf{V} + \nabla \cdot (P_{ij} \cdot \mathbf{V}), \quad (2.14)$$

where  $\frac{\partial E_t}{\partial t}$  is the rate of increase of total energy,

$\nabla \cdot \mathbf{E}_t \mathbf{V}$  is the rate of total energy lost by convection,

$\frac{\partial Q}{\partial t}$  the rate of heat produced by external forces,

$\nabla \cdot \mathbf{q}$  represents the rate of heat lost by conduction,

$\rho \mathbf{f} \cdot \mathbf{V}$  the work done body forces on the control volume,

$\nabla \cdot (P_{ij} \cdot \mathbf{V})$ : the work done by the surface forces on the control volume.

It is worth mentioning that the first law of thermodynamics is equation (2.14). The total energy per unit volume  $E_t$  is given by:

$$E_t = \rho \left( e + \frac{V^2}{2} + \text{potential energy} + \dots \right), \quad (2.15)$$

where  $e$  is the internal energy per unit mass.

For the Cartesian coordinate system, equation (2.14) can be written as:

$$\begin{aligned} & \frac{\partial E_t}{\partial t} - \frac{\partial Q}{\partial t} - \rho(f_x u + f_y v + f_z w) \\ & + \frac{\partial}{\partial x} (E_t u + p u - u \tau_{xx} - v \tau_{xy} - w \tau_{xz} + q_x) \\ & + \frac{\partial}{\partial y} (E_t v + p v - u \tau_{xy} - v \tau_{yy} - w \tau_{yz} + q_y) \\ & + \frac{\partial}{\partial z} (E_t w + p w - u \tau_{xz} - v \tau_{yz} - w \tau_{zz} + q_z) = 0. \end{aligned} \quad (2.16)$$

Using equation (2.2), the left-hand side of equation (2.14) can be expressed as:

$$\rho \frac{D}{Dt} \left( \frac{E_t}{\rho} \right) = \frac{\partial E_t}{\partial t} + \nabla \cdot E_t \mathbf{V}. \quad (2.17)$$

Equation (2.17) takes the following form:

$$\rho \frac{D}{Dt} \left( \frac{E_t}{\rho} \right) = \rho \frac{De}{Dt} + \rho \frac{D}{Dt} \left( \frac{V^2}{2} \right). \quad (2.18)$$

Considering only the kinetic energy and internal energy in equation (2.15) and using the scalar product in equation (2.6), we have

$$\rho \frac{DV}{Dt} \cdot \mathbf{V} = \rho \mathbf{f} \cdot \mathbf{V} - \nabla \cdot V + (\nabla \cdot t_{ij}) \cdot \mathbf{V}. \quad (2.19)$$

After some manipulation, the following equation can be obtained:

$$\rho \frac{De}{Dt} + p(\nabla \cdot \mathbf{V}) = \frac{\partial Q}{\partial t} - \nabla \cdot \mathbf{q} + \Phi, \quad (2.20)$$

where  $\Phi$  is called the dissipation function, and is defined as the rate when the mechanical energy is expanded in the deformation of fluid because of the viscosity. Equation (2.19) can be rearranged to the following form:

$$\rho \frac{DH}{Dt} = \frac{Dp}{Dt} + \frac{\partial Q}{\partial t} - \nabla \cdot \mathbf{q} + \Phi, \quad (2.21)$$

where  $H$  is the enthalpy which is given by

$$H = e + \frac{p}{\rho}.$$

In the Cartesian coordinate system, the dissipation function takes the following form:

$$\begin{aligned} \Phi = \mu \left[ 2 \left( \frac{\partial u}{\partial x} \right)^2 + 2 \left( \frac{\partial v}{\partial y} \right)^2 + 2 \left( \frac{\partial w}{\partial z} \right)^2 + \left( \frac{\partial v}{\partial x} + \frac{\partial u}{\partial y} \right)^2 + \left( \frac{\partial w}{\partial y} + \frac{\partial v}{\partial z} \right)^2 \right. \\ \left. + \left( \frac{\partial u}{\partial z} + \frac{\partial w}{\partial x} \right)^2 - \frac{2}{3} \left( \frac{\partial u}{\partial x} + \frac{\partial v}{\partial y} + \frac{\partial w}{\partial z} \right)^2 \right]. \end{aligned} \quad (2.22)$$

If the flow is incompressible and the thermal conductivity is constant, the energy equation takes the following form:

$$\rho \frac{De}{Dt} = \frac{\partial Q}{\partial t} + k \nabla^2 T + \Phi. \quad (2.23)$$

## 2.4 DISCRETIZATION

The discretization method is defined as the approach of approximating the differential equations by a set of algebraic equations for the variables at some set of discrete locations in space and time [95]. The governing equations can be discretized using three main methods as Finite difference method, Finite volume method, and the Finite element method. The CFD code (ANSYS Fluent) which has been used in this work is based on the finite volume approach.

## 2.5 FINITE VOLUME METHOD (FVM)

A finite volume is a numerical approach to solving partial differential equations. These partial differential equations are calculated by the conserved variables averaged values in the control volume. That distinguishes the finite volume method from the finite difference is the control volume. The FVM is described as follows:

By the divergence theorem, we have

$$\iiint_R \frac{\partial u}{\partial x} dR = \oint_S \mathbf{V} \cdot \mathbf{n} dS, \quad (2.24)$$

where the divergence is the derivative of the vector  $\mathbf{V}$  in one dimension. The purpose of the divergence is to find the finite volume representation of  $\frac{\partial u}{\partial x}$ . At point  $i$  the control volume boundaries are selected as halfway between point  $i$  and its neighbours.

When approximating the averaged derivative at point  $i$ , we use the following form:

$$\left. \frac{\partial u}{\partial x} \right|_i \cong \frac{u_{i+1/2} - u_{i-1/2}}{\Delta x}. \quad (2.25)$$

The values are approximated as:

$$u_{i+1/2} \cong \frac{u_{i+1} + u_i}{2}, \quad (2.26)$$

$$u_{i-1/2} \cong \frac{u_{i-1} + u_i}{2}. \quad (2.27)$$

Equation (2.25) can be modified for equally spaced points to the following:

$$\left. \frac{\partial u}{\partial x} \right|_i \cong \frac{u_{i+1} - u_{i-1}}{2\Delta x}. \quad (2.28)$$

## 2.6 CFD CODE

The equations of continuity, momentum, and energy are discretized and solved using ANSYS 18. For the computational domain and mesh, the computational domain geometry was generated using Design Modeler, and grids were generated using ANSYS Fluent mesh. The pre-processing module for the Fluent software is given in [23]. Throughout this research, each model was analyzed by three main solution steps, namely: ANSYS pre-processing, ANSYS solution, and ANSYS post-processing. Figure 2.6.1. Presents the CFD flow chart.

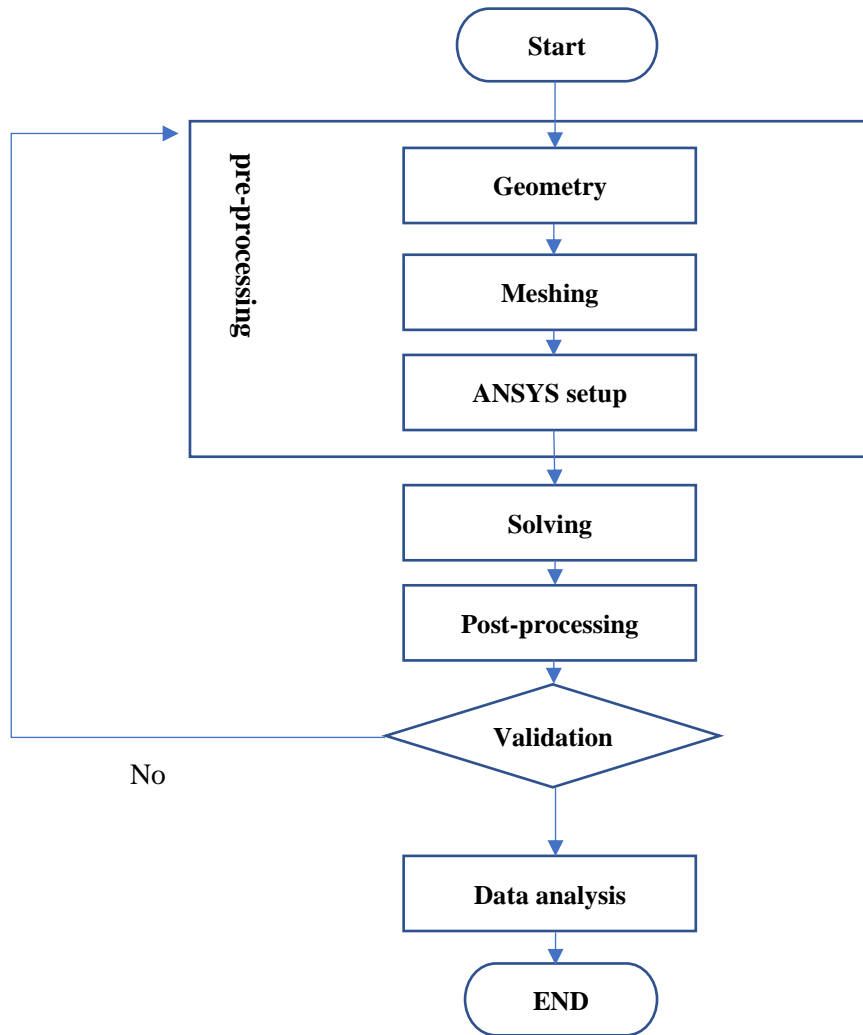


Figure 2.1. CFD flow chart

### 3. CFD MODELLING

Both the single-phase and two-phase modelling of the nanofluids will be considered in our simulations.

#### 3.1 SINGLE-PHASE MODELS

This model is the simplest one for simulating a nanofluid flow and involves the assumption that the nanofluid is considered as a homogeneous fluid with effective properties. However, it is worth to mention that there is no universal correlation that can predict the nanofluid properties with high accuracy for any combination of independent variables such as the diameter of particles. There are many formulas in the literature leading to the same conclusion. The studies show that the nanofluid's properties depend on the volume fraction of the nanoparticles, the base fluid, and the solid particles. The governing equations of the flow are the equations of the continuity, momentum, and energy which are given by

$$\nabla(\rho_{nf} \mathbf{V}_m) = 0, \quad (3.1)$$

$$\nabla(\rho_{nf} \mathbf{V}_m \mathbf{V}_m) = -\nabla P + \nabla(\mu_{nf} \nabla \mathbf{V}_m), \quad (3.2)$$

$$\nabla(\rho_{nf} C_{pnf} \mathbf{V}_m T) = -\nabla(k_{nf} \nabla T). \quad (3.3)$$

##### 3.1.1 NEWTONIAN SINGLE-PHASE MODEL

The Newtonian Single-Phase (NSP) model is applied for a Newtonian fluid. The relationship between the shear rate and the stress in two-dimension is given by (see [97])

$$\tau_{xx} = -2\mu_{nf} \left( \frac{du}{dx} \right), \quad (3.4)$$

$$\tau_{yy} = -2\mu_{nf} \left( \frac{dv}{dy} \right), \quad (3.5)$$

$$\tau_{yx} = \tau_{xy} = -2\mu_{nf} \left( \frac{du}{dy} + \frac{dv}{dx} \right). \quad (3.6)$$

##### 3.1.2 NON-NEWTONIAN SINGLE-PHASE MODEL

In this model, the fluid is treated rheologically as a power-law fluid. The relationship between shear stress and shear rate is given for the power law of two parameters (see [34],[98]) as follows:

$$\tau = -K \left[ \sqrt{\frac{1}{2} (\dot{\gamma} \dot{\gamma})} \right]^{n-1} \dot{\gamma}, \quad (3.7)$$



$$\frac{1}{2}(\dot{\gamma} \dot{\gamma}) = 2 \left\{ \left( \frac{\partial u}{\partial x} \right)^2 + \left( \frac{dv}{dy} \right)^2 \right\} + \left( \frac{\partial v}{\partial x} + \frac{du}{dy} \right)^2. \quad (3.8)$$

The elements of the stress tensors are defined as follows:

$$\tau_{xx} = -2 \left\{ K \left[ 2 \left\{ \left( \frac{\partial u}{\partial x} \right)^2 + \left( \frac{dv}{dy} \right)^2 \right\} + \left( \frac{\partial v}{\partial x} + \frac{du}{dy} \right)^2 \right]^{1/2} \right\}^{(n-1)} \frac{\partial u}{\partial x}, \quad (3.9)$$

$$\tau_{yx} = \tau_{xy} = - \left\{ K \left[ 2 \left\{ \left( \frac{\partial u}{\partial x} \right)^2 + \left( \frac{dv}{dy} \right)^2 \right\} + \left( \frac{\partial v}{\partial x} + \frac{du}{dy} \right)^2 \right]^{1/2} \right\}^{(n-1)} \frac{\partial u}{\partial y} + \frac{\partial v}{\partial x}, \quad (3.10)$$

$$\tau_{yy} = \tau_{xy} = -2 \left\{ K \left[ 2 \left\{ \left( \frac{\partial u}{\partial x} \right)^2 + \left( \frac{dv}{dy} \right)^2 \right\} + \left( \frac{\partial v}{\partial x} + \frac{du}{dy} \right)^2 \right]^{1/2} \right\}^{(n-1)} \frac{\partial v}{\partial y}, \quad (3.11)$$

The parameters  $n$  and  $K$  are empirical constants. The values of these constants depend on the type of nanofluid used. The experimental work [33] has reported the relations between the shear strain and stress for different volume fractions of  $\text{Al}_2\text{O}_3$ -water nanofluid. Table 3.1 shows the two parameters for volume fractions 1- 4% for  $\text{Al}_2\text{O}_3$ .

Table 3.1. The values of the fluid consistency coefficient  $K$  and the power-law index  $n$  of different volume fractions

$\varphi$ [%]	$K$ [Pa s <sup>n</sup> ]	$n$ [-]
0	0.00100	1
1	0.00230	0.830
2	0.00347	0.730
3	0.00535	0.625
4	0.00750	0.540

### 3.2 TWO-PHASE MODELS

The flow of solid-liquid mixture is modelled with two main approaches. The most appropriate approach for mixture fluid with low solid volume fractions is the Lagrangian-Eulerian method, where the Eulerian assumption is used to analyse the base fluid's phase and Lagrangian for the particles' phase. The most suitable method for a mixture with a high-volume fraction is the Eulerian-Eulerian. To model the nanofluid, the following facts should be considered: the number of the nanoparticles in the computational domain is extremely large even for small volume fraction due to the nano-sized particles and the use of the Lagrangian method is unapplicable due to the software limitations, CPU and memory.

The Eulerian-Eulerian method with models Mixture, Eulerian and Volume of Fluid will be used in this study.

### 3.2.1 MIXTURE MODEL

The essential consideration of the mixture model is that only one set of velocity component is solved from the differential equations for mixture momentum conservation. The velocities of dispersed phases are inferred from the algebraic balance equations. This reduces the computational effort considerably. In the mixture model, the primary phase influences the secondary phase via drag and turbulence, while the secondary phase in turn influences the primary phase via reduction in mean momentum and turbulence. The mixture model is based on the following assumptions:

- A single pressure is shared by all phases, and the secondary dispersed phases are assumed to consist of spherical particles of uniform particle size being specified during calculations.
- The interactions between different dispersed phases are neglected.
- The concentrations of the secondary dispersed phases are solved from scalar equations taking into account the correction due to phase slip.

The mixture model has the following limitations and requirements:

- There is no possibility for phase change.
- The flow compressibility is not accounted for.
- Pressure boundary condition cannot be specified because the ideal gas law cannot be employed.
- Neither the turbulence generation in the secondary phases is not accounted for, nor the turbulence of primary phase directly affected by the presence of secondary phase

In the modelling the assumptions that the coupling between phases is strong, and particles closely follow the flow. The two-phases are assumed to be interpenetrating, meaning that each phase has its own velocity vector field, and within any control volume there is a volume fraction of primary phase and also a volume fraction of the secondary phase. Instead of utilizing the governing equations of each phase separately, the continuity, momentum, and fluid energy equations for the mixture are employed. Therefore, the steady-state governing equations describing a mixture fluid flow and the heat transfer in mini-channel are presented as follows:

$$\nabla(\rho_m \mathbf{V}_m) = 0, \quad (3.12)$$

$$\nabla(\rho_m \mathbf{V}_m \mathbf{V}_m) = -\nabla P + \nabla(\mu_m \cdot \nabla \mathbf{V}_m) + \nabla \cdot \left( \sum_{q=1}^n \varphi_q \rho_q \mathbf{V}_{dr,q} \mathbf{V}_{dr,q} \right) - \rho_{m,i} \beta_m g(T - T_i), \quad (3.13)$$

$$\nabla \sum_{q=1}^n (\rho_q C_{pq} \varphi_q \mathbf{V}_q T) = \nabla(k_m \nabla T), \quad (3.14)$$

the mixture density and mixture viscosity are given by

$$\rho_m = \sum_{q=1}^n \varphi_q \rho_q, \quad \mu_m = \sum_{q=1}^n \varphi_q \mu_q, \quad (3.15)$$

respectively, where the volume fraction equation satisfies the following:

$$\nabla(\varphi_p \rho_p \mathbf{V}_m) = -\nabla(\varphi_p \rho_p \mathbf{V}_{dr,p}). \quad (3.16)$$

The mass average velocity and the drift velocity for the secondary phase (nanoparticles velocity) are

$$\mathbf{V}_m = \frac{\sum_{q=1}^n \varphi_q \rho_q \mathbf{V}_q}{\rho_m}, \quad \mathbf{V}_{dr,q} = \mathbf{V}_{pf} - \sum_{q=1}^n \frac{\varphi_q \rho_q}{\rho_m} \mathbf{V}_{fq}. \quad (3.17)$$

The slip, the relative velocity is defined as the velocity of a secondary phase (nanoparticle,  $p$ ) relative to the velocity of the primary phase (fluid,  $b$ ):

$$\mathbf{V}_{pf} = \mathbf{V}_p - \mathbf{V}_b = \frac{\rho_p d_p (\rho_p \rho_m)}{18 \mu_b f_{drag} \rho_p} a. \quad (3.18)$$

The drag of the solid particle is

$$f_{drag} = f(x) = \begin{cases} 1 + 0.15 \text{Re}_p^{0.687}, & \text{Re}_p \leq 1000, \\ 0.0183 \text{Re}_p, & \text{Re}_p > 1000, \end{cases} \quad (3.19)$$

where  $\text{Re}_p = \frac{V_m d_p}{\nu_m}$ . The acceleration:  $a = g - (\mathbf{V}_m \nabla) \mathbf{V}_m$ . (3.20)

### 3.2.2 EULERIAN MODEL

There are various coupling mechanisms between the solid and fluid phases in the Eulerian model. Both phases share the same pressure, while different continuity, momentum, and energy equations are used for various phases, including fluid and solid phase. By integrating the volume fraction through the studied domain, the volumes of the fluid and solid phases are calculated. At the same time, all the volume fractions are equal to unity in the summation. For both processes, the governing equations (mass, momentum, and energy) are the following:

$$\nabla(\rho_b \varphi_b \mathbf{V}_b) = 0, \quad \nabla \cdot (\rho_p \varphi_p \mathbf{V}_p) = 0, \quad \varphi_b + \varphi_p = 1, \quad (3.21)$$

$$\nabla(\rho_b \varphi_b \mathbf{V}_b \mathbf{V}_b) = -\varphi_b \nabla P + \nabla[\varphi_b \mu_b (\nabla \mathbf{V}_b + \nabla \mathbf{V}_b T)] - F_d + F_{vm}, \quad (3.22)$$

$$\nabla(\rho_p \varphi_p \mathbf{V}_p \mathbf{V}_p) = -\varphi_p \nabla P + \nabla[\varphi_p \mu_p (\nabla \mathbf{V}_p + \nabla \mathbf{V}_p T)] - F_d + F_{vm} + F_{col}. \quad (3.23)$$

In our analysis the lift force is neglected due to the nano-size of the particles. The drag force between the phases is

$$F_d = -\beta(\mathbf{V}_b - \mathbf{V}_p), \quad (3.24)$$

where the drag force between the phases is calculated as:

$$\beta = \frac{3}{4} C_d \frac{\varphi_1(1-\varphi_1)}{d_p} \rho_1 |\mathbf{V}_b + \mathbf{V}_p| \varphi_1^{-2.65} , \quad (3.25)$$

and the friction coefficient

$$C_d = \begin{cases} \frac{24}{Re_p} (1 + 0.15 Re_p^{0.687}), & Re_p < 1000 , \\ 0.44, & Re_p \geq 1000 , \end{cases} \quad (3.26)$$

where

$$Re_p = \frac{\varphi_b \rho_b |\mathbf{V}_b - \mathbf{V}_p| d_p}{\mu_b} . \quad (3.27)$$

The energy equations are written in (36)-(37), considering the base liquid and nanoparticle phases as incompressible fluids, and ignoring viscous dissipation and radiation

$$\nabla(\rho_b \varphi_b C_{pb} T_b \mathbf{V}_b) = \nabla(\varphi_b k_{nf,b} \nabla T_b) - h_v (T_b - T_p), \quad (3.28)$$

$$\nabla(\rho_p \varphi_p C_{pp} T_p \mathbf{V}_p) = \nabla(\varphi_p k_{nf,p} \nabla T_p) - h_v (T_b - T_p). \quad (3.29)$$

For nano-dispersed spherical particles,  $h_v$  can be calculated from:

$$h_v = \frac{6(1-\varphi_b)}{d_p} h_p , \quad (3.30)$$

where  $h_p$  is the fluid-particle heat transfer coefficient and calculated from empirical correlations [99].

### 3.2.3 VOLUME OF FLUID (VOF) MODEL

The VOF model solves the single set of the momentum equation for the fluid phase and solid phase and tracks their volume fraction with the domain of the study by solving the continuity equation for the solid phase. The total summation of the volume fractions for all phases is equal to unity. The magnitude of the primary phase volume fraction will be calculated. The physical properties are calculated by a weighted average of different phases based on their volume fraction through each control volume. The velocity components shared by all phases are determined using a single set of momentum equations:

$$\nabla(\varphi_q \rho_q \mathbf{V}_q) = 0, \quad (3.31)$$

where  $\sum_{q=1}^n \varphi_q = 1$ . All the properties are calculated as the number of the phases,  $N = \sum_{q=1}^n \varphi_q N_q$ .

The conservation of momentum and energy equations are similar as equations (3.2) and (3.3).

### 3.3 MODELLING THE THERMOPHYSICAL PROPERTIES OF NANOFLUIDS

#### 3.3.1 CONSTANT THERMO-PHYSICAL PROPERTIES

Equations (3.32)–(3.34) are applied for estimating the density and specific heat capacity of the nanofluids as introduced in [82], [100].

Here the physical properties of the nanofluid are given with the dimensionless nanoparticle concentration  $\varphi$  as follows:

- Density and heat capacity

The effective density of the nanofluid is given by [18]:

$$\rho_{nf} = (1 - \varphi)\rho_b + \varphi\rho_p, \quad (3.32)$$

where density base fluid, and nanoparticles, and the heat capacity of the nanofluid is assumed as below[19]:

$$C_{pnf} = \frac{\varphi(\rho C_p)_p + (1-\varphi)(\rho C_p)_b}{\rho_{nf}}. \quad (3.33)$$

- Thermal conductivity

The thermal conductivity of nanofluid, is given as follows [20]:

$$k_{nf} = k_b \frac{k_p + 2k_b - 2\varphi(k_b - k_p)}{k_p + 2k_b + \varphi(k_b - k_p)}. \quad (3.34)$$

- The effective viscosity of nanofluid:

$$\mu_{nf} = \frac{\mu_b}{(1-\varphi)^{2.5}}. \quad (3.35)$$

The effective viscosity of  $\text{Al}_2\text{O}_3$  nanofluids, which depends only on the volume fraction, is based on the experimental data presented by Maiga et al. [27] as follow:

$$\mu_{nf} = \mu_b(1 + 7.3\varphi + 123\varphi^2), \quad (3.36)$$

The effective viscosity of  $\text{TiO}_2$  nanofluids, which depends only on the volume fraction, is based on the experimental data presented by [102] as follow:

$$\mu_{nf} = \mu_b(1 + 5.45\varphi + 108.2\varphi^2). \quad (3.37)$$

### 3.3.2 TEMPERATURE-DEPENDENT THERMO-PHYSICAL PROPERTIES

Reasonable concepts of thermo-physical property relations for nanofluids have a great impact on this model. For calculating the thermal and physical properties of the water, the following formulas are used [103]:

$$\rho_b(T) = 1000[1 - T + 15.7914508928.2T - 205.0204(T - 277.1363)^2], \quad (3.38)$$

$$C_{pb}(T) = 9616.873445 - 48.73648329T + 0.1444662T^2 - 0.000141414T^3, \quad (3.39)$$

$$\mu_b(T) = 0.02165 - 0.0001208T + 1.7184 \times 10^{-7}T^2, \quad (3.40)$$

$$k_b(T) = -1.1245 + 0.009734T - 0.00001315 \times T^2. \quad (3.41)$$

Corcione [104] obtained correlation (3.42) for nanofluid thermal conductivity through regression analysis with a standard deviation error of 1.86 %, where  $T$  denotes the temperature in Kelvin.

$$\frac{k_{nf}}{k_b} = 1 + 4.4\text{Re}^{0.4}\text{Pr}^{0.66}\left(\frac{T_{nf}}{T_{fr}}\right)^{10}\left(\frac{k_s}{k_f}\right)^{0.03}\varphi^{0.66}, \quad (3.42)$$

$$\text{Re} = \frac{2\rho_b k_b T_{nf}}{\pi \mu_b^2 d_p}, \quad (3.43)$$

$$\text{Pr} = (\mu_b C_{pb})/k_b. \quad (3.44)$$

Table 3.1. Thermo-physical properties of the nanoparticles

Parameter	Fe <sub>3</sub> O <sub>4</sub>	TiO <sub>2</sub>	Al <sub>2</sub> O <sub>3</sub>	SiO <sub>2</sub>	H <sub>2</sub> O
$\rho$ (kg/m <sup>3</sup> )	5180	4250	3970	2200	997.1
$C_p$ (J/kg. K)	670	686.2	765	703	4179
$k$ (W/m. K)	9.7	8.9538	40	1.2	0.613
$\mu$ (Pa. s)	—	—	—		0.001

#### 4. FLOW OVER FLATE PLATE (FLUID WITH CONSTANT PROPERTIES)

In a steady and incompressible flow, we consider a semi-infinite flat plate at  $y = 0$  with a stream with velocity  $U_{nf}$  parallel to the plate and with constant pressure. Applying the Blasius description [105] for Newtonian fluid flows, we study similarity solutions. As the free stream velocity is assumed constant, thus the pressure gradient along the plate can be neglected. For large values of the Reynolds number, the longitudinal viscous stresses are negligible compared to the transverse viscous terms in the momentum equation and the boundary layer can be described by the equations (4.1)-(4.3).

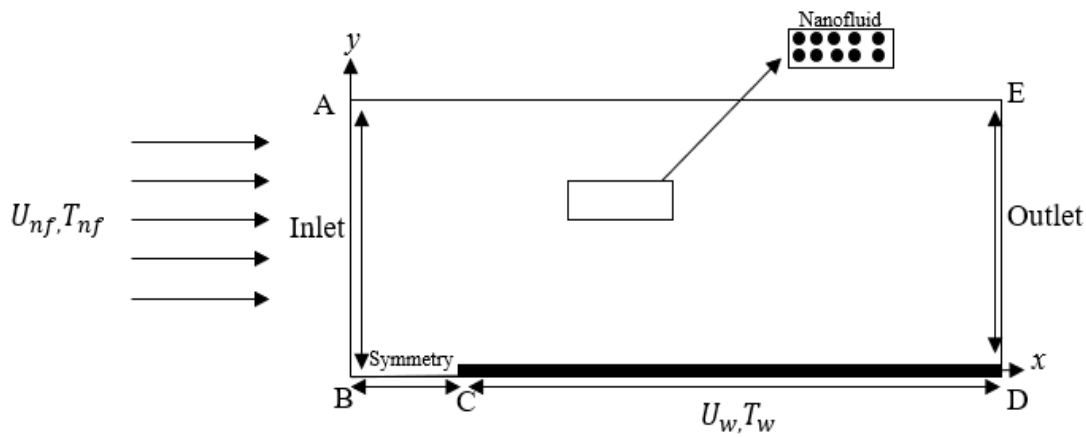


Figure 4.1. Flow configuration

We study analytically and numerically the boundary layer flow and heat transfer next to a stable flat plate with forced convection, assuming that the base fluid and the nanoparticles are in thermal equilibrium and there is no slip between them. The nanofluid is assumed to be incompressible, and the viscous dissipation and radiation effects are neglected. A two-dimensional laminar flow of aqueous nanofluids containing  $\text{Al}_2\text{O}_3$ ,  $\text{TiO}_2$ , and  $\text{Fe}_3\text{O}_4$  nanoparticles is considered. The nanofluids are assumed to be Newtonian fluid, and their thermophysical properties are independent of the liquid temperature.

To solve the governing equations, the nanofluid properties we need the density, heat capacity, viscosity, and thermal conductivity. The relationships used to describe the physical properties of the nanofluid are shown in Chapter 3 by equations (3.32)-(3.35).

#### 4.1 SIMILARITY ANALYTIC SOLUTIONS

Take a rectangular coordinate system  $(x, y)$  for a flow of nanofluid over a flat surface at a constant velocity parallel to the surface. The  $x$  coordinate is along the surface, and  $y$  is perpendicular to it. The flat surface is kept at a constant temperature  $T_w$ , while the temperature of the nanofluid away from the surface is  $T_{nf}$ . The system equations are described as follows:

$$\frac{\partial u}{\partial x} + \frac{\partial v}{\partial y} = 0, \quad (4.1)$$

$$u \frac{\partial u}{\partial x} + v \frac{\partial u}{\partial y} = \frac{\mu_{nf}}{\rho_{nf}} \frac{\partial^2 u}{\partial y^2}, \quad (4.2)$$

$$u \frac{\partial T}{\partial x} + v \frac{\partial T}{\partial y} = \alpha_{nf} \frac{\partial^2 T}{\partial y^2}. \quad (4.3)$$

At the solid surface, the usual impermeability and no-slip are applied, and outside the viscous boundary layer, the streamwise velocity component  $u$  should approach the exterior streaming speed  $U_{nf}$ . So, the boundary conditions are given by

$$u(x, 0) = 0, \quad v(x, 0) = 0, \quad T(x, 0) = T_w, \quad \lim_{y \rightarrow \infty} u(x, y) = U_{nf}, \quad \lim_{y \rightarrow \infty} T(x, y) = T_{nf}. \quad (4.4)$$

The solution is not defined at  $x = 0$ , as an infinite velocity gradient is required at the leading edge of the plate. Applying self-similarity method, we introduce the stream function  $\psi$  defined by  $u = \frac{\partial \psi}{\partial y}$ ,  $v = -\frac{\partial \psi}{\partial x}$ , and thereby automatically satisfying the continuity equation (4.1).

The dimensionless similarity variable is defined as follows:

$$\eta = \left( \frac{U_{nf}}{\nu_{nf} x} \right)^{1/2} y, \quad (4.5)$$

where  $\nu_{nf} = \frac{\mu_{nf}}{\rho_{nf}}$  is the kinematic viscosity.

The stream function and the dimensionless temperature are expressed as:

$$\psi = (U_{nf} \nu_{nf} x)^{1/2} f(\eta), \quad \theta(\eta) = \frac{T - T_{nf}}{T_w - T_{nf}}. \quad (4.6)$$

From (4.2) we obtain a third-order, homogeneous ordinary differential equation for  $f$  as follows:

$$\frac{\rho_b}{\rho_{nf}} \frac{\mu_{nf}}{\mu_b} f''' + \frac{1}{2} f f'' = 0, \quad (4.7)$$



where the prime denotes the differentiation with respect to the similarity variable  $\eta$ . The boundary conditions reduce to the following:

$$f(0) = 0, \quad f'(0) = 0, \quad \lim_{\eta \rightarrow \infty} f'(\eta) = 1. \quad (4.8)$$

The velocity components are obtained by  $f$  as follows:

$$u(x, y) = U_{nf} f'(\eta), \quad (4.9)$$

$$v(x, y) = v^*(x) [\eta f'(\eta) - f(\eta)], \quad (4.10)$$

with  $v^*(x) = \frac{U_{nf}}{2} Re_x^{-\frac{1}{2}}$ , and the local Reynolds number  $Re_x$  is defined by  $Re_x = \frac{U_{nf} x}{\nu_{nf}}$ .

If  $\rho_{nf} = \rho_b$ , and  $\mu_{nf} = \mu_b$ , then (4.7) is the famous Blasius' equation [105]:

$$f''' + \frac{1}{2} f f'' = 0. \quad (4.11)$$

Applying similarity functions (4.6) to energy equation (4.3), one can obtain

$$\alpha_{nf} \frac{\rho_b}{\mu_b} \theta'' + \frac{1}{2} f \theta' = 0, \quad (4.12)$$

subjected to boundary conditions:

$$\theta(0) = 1, \quad \lim_{\eta \rightarrow \infty} \theta(\eta) = 0. \quad (4.13)$$

In the case of similarity solutions, the equations (4.8) and (4.13) have the form for nanofluid flow:

$$\frac{1}{(1-\varphi)^{2.5}(1-\varphi+\varphi\rho_p/\rho_b)} f''' + \frac{1}{2} f f'' = 0, \quad (4.14)$$

$$\frac{1}{Pr} \frac{k_{nf}/k_b}{(1-\varphi)^{2.5}(1-\varphi+\varphi(\rho C_p)_p/(\rho C_p)_b)} \theta'' + \frac{1}{2} f \theta' = 0, \quad (4.15)$$

where  $Pr = \frac{\nu_b}{\alpha_b}$  is the Prandtl number. System of equations (4.1) -(4.15) was solved with boundary conditions (4.8) and (4.13) applying MATLAB for all three nanofluids for different volume fractions.

The wall shear stress ( $\tau_w$ ) and heat flux ( $q_w$ ) are given by

$$\tau_w = \mu_{nf} \left( \frac{\partial u}{\partial y} \right)_{y=0}, \quad q_w = -k_{nf} \left( \frac{\partial T}{\partial y} \right)_{y=0}, \quad (4.16)$$

and the skin friction coefficient ( $C_f$ ) and the local Nusselt number ( $Nu$ ) are defined as

$$C_f = \frac{\tau_w}{\rho_b U_{nf}^2}, \quad Nu = \frac{x q_w}{k_{nf} (T_w - T_{nf})}. \quad (4.17)$$

Applying the similarity variables, we obtain

$$Re_x^{1/2} C_f = \frac{1}{(1-\phi)^{2.5}} f''(0), \quad Re_x^{-\frac{1}{2}} Nu = -\frac{k_{nf}}{k_b} \theta'(0). \quad (4.18)$$

## 4.2 NUMERICAL PROCEDURE (CFD)

To determine the nanofluid flow characteristics, we perform CFD simulations as shown in Fig.4.1. The equations of the continuity, momentum, and energy equations (4.1) – (4.3) are discretized and solved with the use of ANSYS R18.1 program. The geometry of the computational domain is created using the Design Modeler, and the grids are generated using the ANSYS Fluent mesh. The inlet and outlet are split into 200 divisions by the division method. The behaviour is set to hard with a bias factor of 10 to increase the number of subdomains above the plate. The types of boundary conditions used are shown in Table 4.1 The EA and BC edges are set symmetrical, and the CD edge is set as the wall. The edges AE and CD are divided into 440 and 400 divisions, respectively, in a similar manner. The dimensions of the geometry establish a model that can be implemented correctly according to the equations and the boundary conditions. The length of the sheet is  $x = 1$  m. The dimension in  $y$  is  $y = 0.5$  m, which is enough far away above the plate to have little influence on the result when the maximum boundary thickness is about 0.05 m.

In the numerical simulations, a laminar flow is investigated by the pressure-velocity coupling. In our calculations, we choose a relaxation factor of 1 for density, body strength, and energy. A single-phase approach is used for all thermophysical properties of the nanofluids. We determine the local Nusselt number to check the grid sensitivity.

Table 4.1. The boundary conditions

Edge	Boundary condition
AB	inlet
BC	symmetry
CD	wall
DE	outlet
EA	symmetry

The purpose of the mesh sensitivity test is to minimize the numerical effects of the mesh size. For five meshes, mesh sensitivity analysis was performed with 7000, 9600, 14,400, 20,000, and 26,400 elements. The Nusselt number on the flat surface is compared for these meshes. It can be stated that the

Nusselt number for the mesh containing 20,000 elements is sufficient for a solution accuracy that ensures the independence of the grid in the simulations.

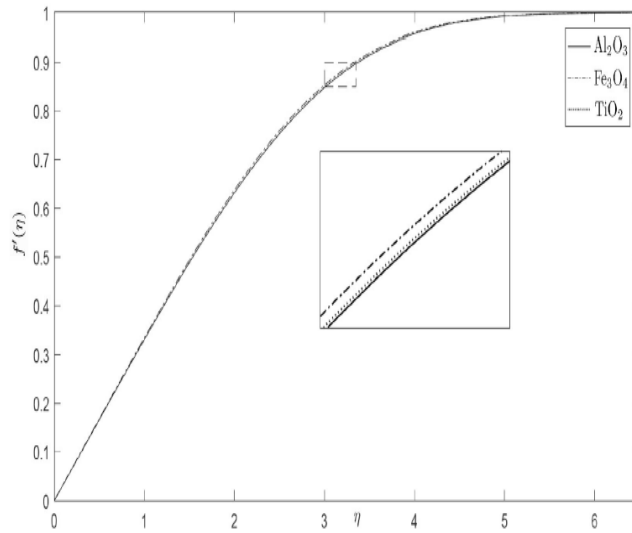


Figure 4.2. The dimensionless velocity profiles  $f'$  for three types of nanofluids ( $\phi = 0.02$ )

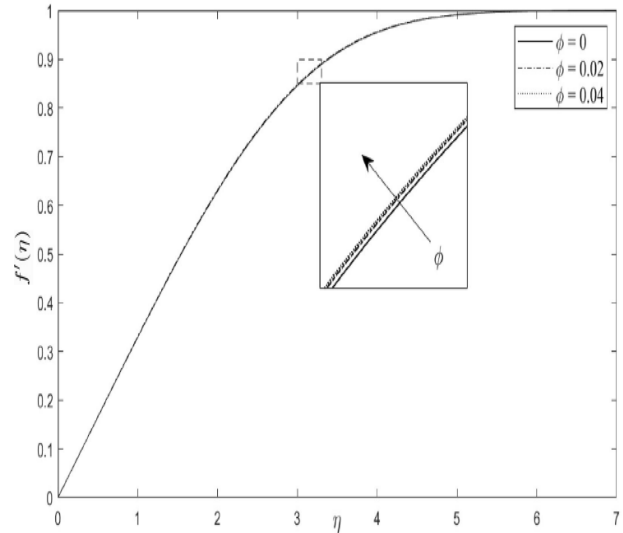


Figure 4.3. The dimensionless velocity profiles  $f'$  for different values of  $\phi$  ( $\text{Al}_2\text{O}_3$ )

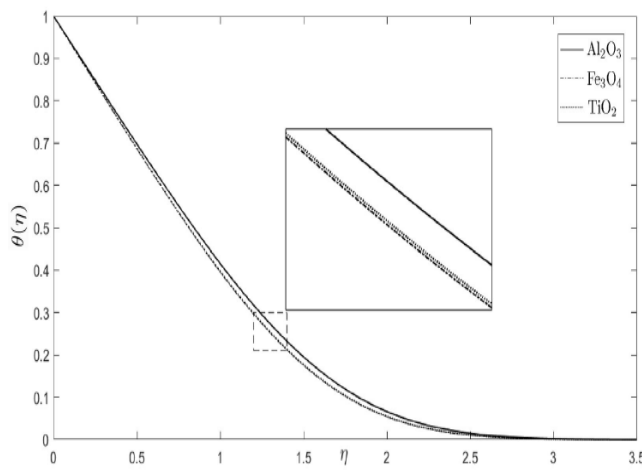


Figure 4.4. Temperature distribution for different nanoparticle materials

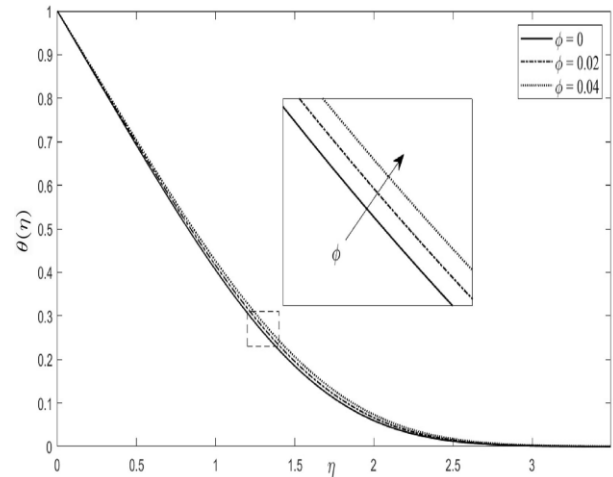


Figure 4.5. Temperature distribution for different values of  $\phi$  ( $\text{Al}_2\text{O}_3$ )

### 4.3 RESULTS

Figures 4.2–4.3 show the numerically compared solutions in the  $(\eta, f'(\eta))$  plane using (4.14) and (4.15). The velocity  $u$  is proportional to  $f'(\eta)$ , and  $\eta$  to the boundary layer thickness. Figure 4.2 illustrates the velocity for nanofluids containing the three types of nanoparticles studied for the volume

fraction  $\varphi = 0.02$ . The fastest velocity increase is observed for Fe<sub>3</sub>O<sub>4</sub>, and the largest boundary layer thickness is for Al<sub>2</sub>O<sub>3</sub>. Figures 4.4 and 4.5 show the dimensionless temperature  $\theta(\eta)$  for different nanoparticle's materials and for different volume fractions of Al<sub>2</sub>O<sub>3</sub>. On the contrary, for the temperature (see Fig. 4.4), we get the highest temperature value, the smallest thermal boundary layer thickness, and the fastest change in the temperature for TiO<sub>2</sub>.

#### 4.4 COMPARISON OF SIMILARITY AND CFD RESULTS

Figure 4.6 exhibits the skin friction coefficient  $C_f$  for Al<sub>2</sub>O<sub>3</sub> against the Reynolds number for three values of  $\varphi$  (0, 0.02, 0.04) obtained with CFD. Increase in  $\varphi$  causes elevation of the skin friction coefficient. The variation of  $C_f$  with  $\varphi$  is exhibited in Fig.4.7. For all three nanofluids, the skin friction grows with the volume fraction. The biggest growth is seen for Fe<sub>3</sub>O<sub>4</sub>. Figure 4.8 shows the Nusselt number obtained from the CFD simulations for increasing the amount of Al<sub>2</sub>O<sub>3</sub> nanoparticles. It can be seen that if the Reynolds number increases then the Nusselt number increases.

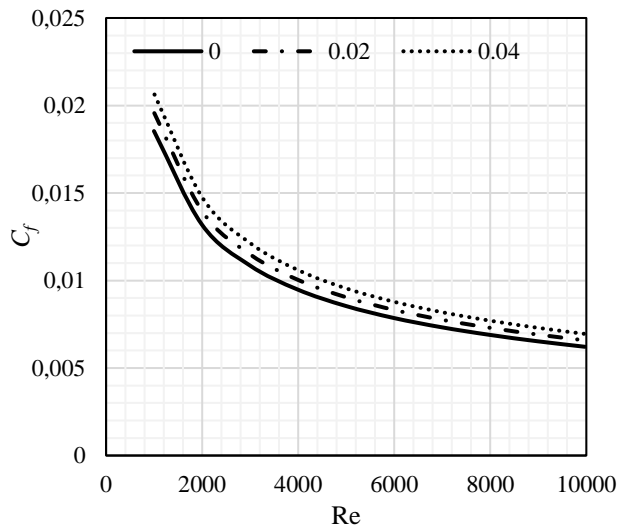


Figure 4.6. Variation of  $C_f$  for  $\varphi=0, 0.02, 0.04$  with Re (Al<sub>2</sub>O<sub>3</sub>)

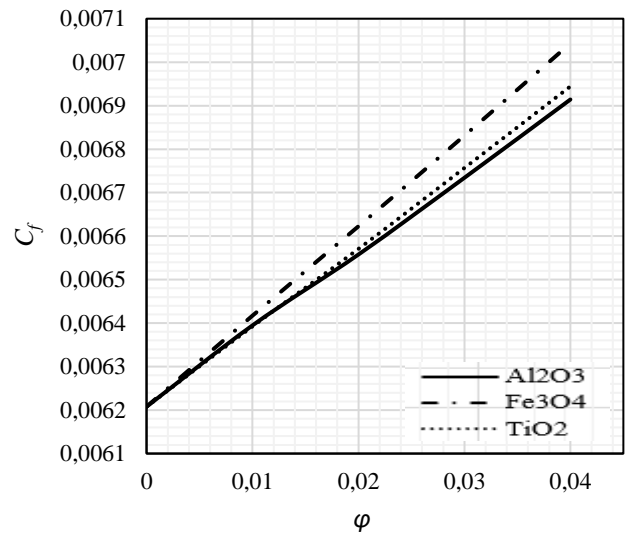


Fig. 4.7. Variation of skin friction  $C_f$  for  $\varphi=0, 0.02, 0.04$

The values of  $Re^{1/2}C_f$  are compared for the similarity solution to the Blasius problem and the CFD solutions for nanofluids in Table 4.2. For water ( $\varphi = 0$ ), we got from (4.14) the well-known value 0.332. Table 4.2 shows that the values obtained with CFD are always smaller than the analytic ones. Comparison of the CFD and similarity solutions in each nanofluid shows that the largest difference 6.7%, occurred for  $\varphi = 0$ . The difference decreases with increasing  $\varphi$ . For  $\varphi = 0.04$ , the smallest differences are 5.7% (Al<sub>2</sub>O<sub>3</sub>), 3.5% (TiO<sub>2</sub>), and 1.9% (Fe<sub>3</sub>O<sub>4</sub>).

We note that the similarity solutions obtained for  $\text{Al}_2\text{O}_3$  show a very good agreement with those reported in [106]. Variation of  $Re^{1/2}C_f$  with  $\varphi$  is plotted in Fig. 4.9.  $Re^{1/2}C_f$  with  $\varphi$  increase with  $\varphi$ . The line for  $\text{Fe}_3\text{O}_4$  is the steepest. We remark that no comparison with [106] is available. The reason is that in this work, the Prandtl number was fixed as  $Pr = 6.2$ , and in our calculations, the Prandtl number for the working fluid is  $Pr = 6.817$ .

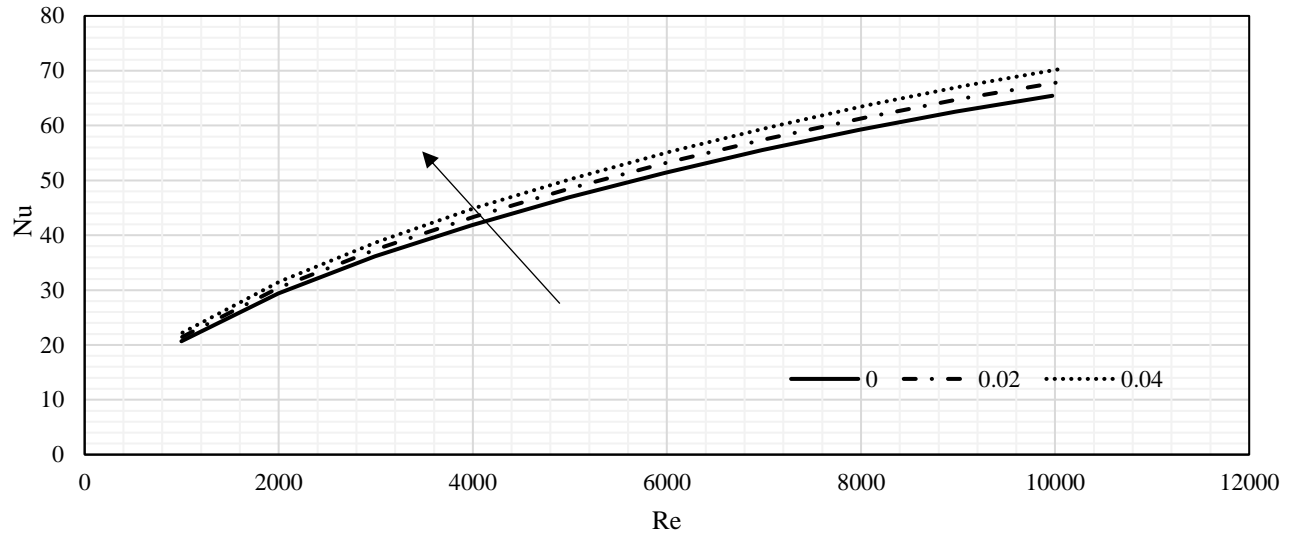


Fig. 4.8. Variation of  $Nu$  for  $\varphi=0, 0.02, 0.04$  with  $Re$  ( $\text{Al}_2\text{O}_3$ )

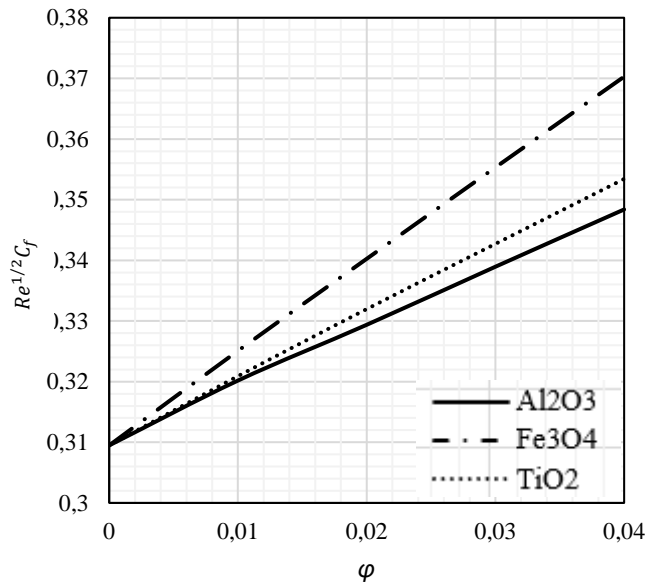


Fig. 4.9. Variation of  $Re^{1/2}C_f$  with  $\varphi$

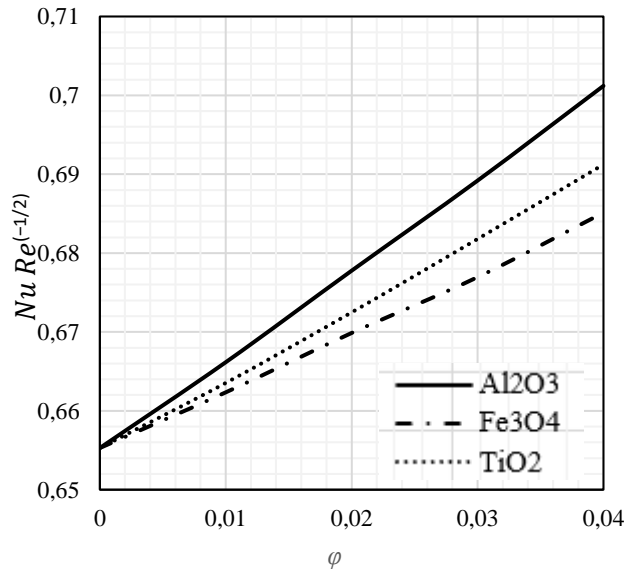


Fig. 4.10 Variation of  $Nu Re^{-1/2}$  with  $\varphi$

Table 4.2. Values of  $Re^{\frac{1}{2}} C_f$  for both methods

$\varphi$	<b>Al<sub>2</sub>O<sub>3</sub></b>			<b>TiO<sub>2</sub></b>			<b>Fe<sub>3</sub>O<sub>4</sub></b>		
	similarity	CFD	%	similarity	CFD	%	similarity	CFD	%
0.0	0.64020	0.65529	0.02302	0.64020	0.65529	0.02302	0.64020	0.65529	0.00988
0.01	0.65231	0.66616	0.02079	0.65079	0.66353	0.0192	0.65219	0.66234	0.00672
0.02	0.66439	0.67777	0.01974	0.66130	0.67248	0.01662	0.66409	0.66987	0.00387
0.03	0.67647	0.68919	0.01845	0.67177	0.68179	0.01469	0.67593	0.67695	0.00069
0.04	0.68854	0.70120	0.01805	0.68220	0.69123	0.01306	0.68771	0.68512	0.00177

Table 4.3. Values of  $Re^{-\frac{1}{2}} Nu$  for both methods

$\varphi$	<b>Al<sub>2</sub>O<sub>3</sub></b>			<b>TiO<sub>2</sub></b>			<b>Fe<sub>3</sub>O<sub>4</sub></b>		
	similarity	CFD	%	similarity	CFD	%	similarity	CFD	%
0.0	0.33205	0.309491	0.0679	0.33205	0.309491	0.06793	0.33205	0.309491	0.0679
0.01	0.34123	0.320174	0.0617	0.34169	0.320899	0.0608	0.34323	0.325079	0.0528
0.02	0.35055	0.329369	0.0604	0.35148	0.331960	0.05553	0.35454	0.340246	0.0403
0.03	0.36004	0.338946	0.0585	0.36061	0.34271	0.04963	0.36600	0.355318	0.0291
0.04	0.36969	0.348388	0.0576	0.37154	0.353414	0.04878	0.37762	0.370278	0.0194

In Table 4.3, in contrast to Table 4.2, CFD gives a little bit higher value. The degree of deviation is slightly reduced at an increase in the volume fraction of nanoparticles. For water, it is 2.3%. The smallest value for Fe<sub>3</sub>O<sub>4</sub> is 0.1% at  $\varphi = 4\%$ . Figures 4.9 and 4.10 show that for higher volume concentrations, the effect on both the skin friction and the heat transfer coefficient is more significant.

Both the similarity analysis and CFD simulation were performed for investigation of the impact of the nanoparticle material and the volume fraction of nanoparticles on a nanofluid flow over a steady sheet. The difference between the two types of models is discussed. In the application of the classical similarity method, when we take the usual Blasius neglects in the members of the Navier–Stokes equation, the governing equations are transformed to ordinary differential equations by the similarity method. For the CFD simulation solutions, the complete Navier–Stokes equation is used. The impact of several parameters controlling the velocity and temperature distributions are calculated by both methods, and the two types of solutions are compared for water-based nanofluids with three types of nanoparticles ( $\text{Al}_2\text{O}_3$ ,  $\text{Fe}_3\text{O}_4$ , and  $\text{TiO}_2$ ) and four-volume fraction concentrations. Some important observations are

listed below:

- The dimensionless velocity is greater if the volume fraction is larger.
- The highest velocity is obtained for the nanofluid with  $\text{Fe}_3\text{O}_4$  nanoparticles. As the volume fraction increases, the dimensionless temperature rises due to better heat transfer.
- The skin friction grows with the volume fraction.
- The highest skin friction coefficient is found in the case of  $\text{Fe}_3\text{O}_4$ .
- The Nusselt number increases with  $\varphi$ .
- The Nusselt number is the biggest for  $\text{Al}_2\text{O}_3$  nanoparticles and the smallest for  $\text{TiO}_2$ .
- We compared the change in the skin friction coefficient and local Nusselt number for the similarity and CFD methods. The differences depend on  $\varphi$ . The volume fraction enlarges the difference, but the maximum deviation in the studied  $\varphi$  range of is less than 6.7% for the skin friction and less than 2.3% for the Nusselt number.
- The calculated values were compared with the results obtained in [106].

## 5. SAKIADIS FLOW OF NANOFLUID

The Sakiadis problem has been analysed in both the physics and mathematics literature and has attracted interest in the analytical and numerical studies of boundary layers. For the Sakiadis problem, we study the similarity solutions and CFD simulation results by investigating the thermal and bulk properties and compare the obtained results to numerically justify the Blasius boundary layer approach. The geometry and dimensions used in this section are the same as those described in Section 4.

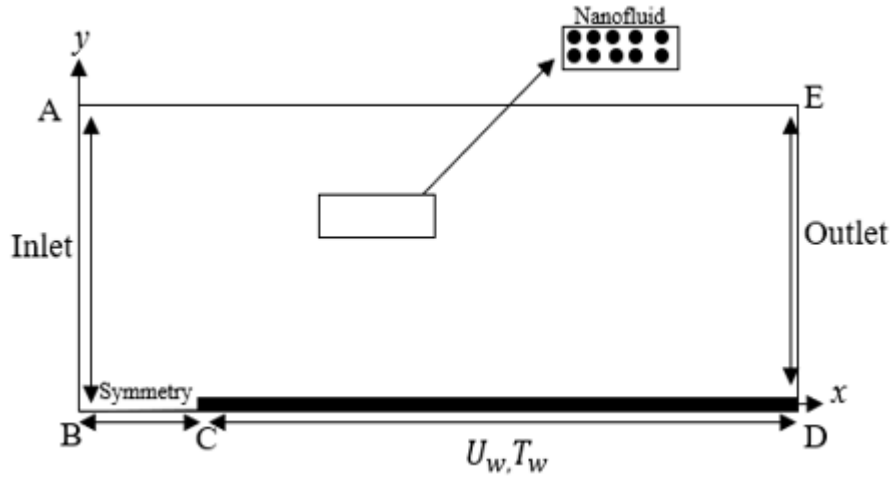


Figure 5.1. Flow configuration

### 5.1 SIMILARITY ANALYTIC SOLUTION

Consider a two-dimensional laminar boundary layer flow over a continuously moving flat surface for a water-based nanofluid containing three different types of nanoparticles. The nanoparticles are spherical and the average particle size is considered to be between 20-30 nm. It is assumed that the nanofluid is incompressible, the flow is laminar, and the effects of viscous distribution and radiation are negligible.

In the Cartesian coordinate system, the  $x$ -axis is chosen along the flow direction, while the  $y$ -axis is perpendicular to the surface. The nanofluid is confined above the horizontal surface, which surface coincides with the positive  $x$ -axis. The temperature  $T_\infty$ , of the surrounding fluid is constant and the temperature of the surface is  $T_w$ . In our case,  $T_w < T_\infty$ . The velocity components  $u$  and  $v$  are the velocity components parallel and perpendicular to the plate, respectively;  $\mu_{nf}$  is the dynamic viscosity,  $\rho_{nf}$  is the density, and  $\alpha_{nf}$  is the thermal diffusivity of the nanofluid.



In conventional boundary-layer theory, several assumptions are made: the momentum and thermal boundary layers are very thin relative to the length of the flow and increase in the direction of surface motion; the velocity parallel to the walls is much larger than the velocity component  $v$ , and the derivatives of the velocity components with respect to the wall are large [107]. The fluid flow components outside the thermal boundary layer is not affected by the heat transfer from the moving surface.

We are investigating the flow of a nanofluid in an otherwise quiescent medium along a plate moving at a constant speed  $U$ . We apply the conventional impermeability and slip resistance to the solid interface, and the flow velocity component  $u = 0$  to a viscous boundary layer. The boundary conditions for the velocity and temperature fields for the Sakiadis flow problem are as follows:

$$u(x, 0) = U_{nf}, \quad v(x, 0) = 0, \quad T(x, 0) = T_w, \quad \lim_{y \rightarrow \infty} u(x, y) = 0, \quad \lim_{y \rightarrow \infty} T(x, y) = T_\infty. \quad (5.1)$$

Applying the similarity transformation (4.6), we obtain a system of ordinary differential equations for  $f$  and  $\varphi$ , (similar to Blasius's equation):

$$\frac{\rho_b}{\rho_{nf}} \frac{\mu_{nf}}{\mu_b} f''' + \frac{1}{2} f f'' = 0, \quad (5.2)$$

$$\alpha_{nf} \frac{\rho_b}{\mu_b} \theta'' + \frac{1}{2} f \theta' = 0, \quad (5.3)$$

where the prime denotes the differentiation with respect to  $\eta$ . To satisfy conditions (5.1), the equations (5.2) and (5.3) are considered together with the following boundary conditions:

$$f(0) = 0, \quad f'(0) = 1, \quad \lim_{\eta \rightarrow \infty} f'(\eta) = 0, \quad (5.4)$$

$$\theta(0) = 1, \quad \lim_{\eta \rightarrow \infty} \theta(\eta) = 0. \quad (5.5)$$

The solution to (4.1) and (4.3) is obtained using the fourth-order method (bvp4c) of MATLAB with conditions (5.4) and (5.5), where the nanofluid properties are calculated according to the formulas (3.32)-(3.35) using the thermophysical values given in Table 3.1 for  $\text{Al}_2\text{O}_3$ ,  $\text{TiO}_2$ , and  $\text{Fe}_3\text{O}_4$  particles and the water base fluid. Our aim is to investigate the effect of volume fraction and nanoparticle material type on the heat and mass transfer characteristics.

## 5.2 RESULTS

Figure 5.2 exhibits the dimensionless velocity distributions for all three nanofluids for 2% additives in the base fluid. It shows that the velocity is greater for  $\text{Al}_2\text{O}_3$  than for the other two materials.

Figure 5.3 represents the temperature distribution for the same cases. Here, the  $\text{Al}_2\text{O}_3$  also shows greater values than other values. The effect of the volume fraction  $\phi$  is depicted in Figs. 5.4 and 5.5. It was observed that increasing  $\phi$  will slow down the fluid flow velocity and will increase the non-dimensional.

Figures 5.6 and 5.7 show the impact of the nanoparticles' material on the dimensional velocity and temperature profiles for  $\phi = 0.02$ , respectively. We remark that these figures are in correlation with Figures 5.2 and 5.3.

The impact of the nanoparticle's concentration was investigated on  $\text{Al}_2\text{O}_3$ –water nanofluid in Figs. 5.6 and 5.9. It follows, according to Figs. 5.4 and 5.5, that more additives will reduce the velocity and increase the non-dimensional temperature.

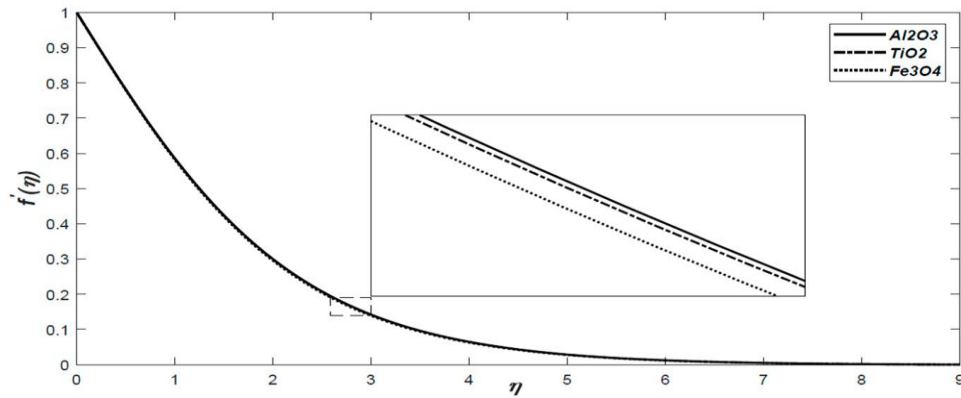


Figure 5.2 The dimensionless velocity profiles for  $\phi = 0.02$  for all three nanofluids

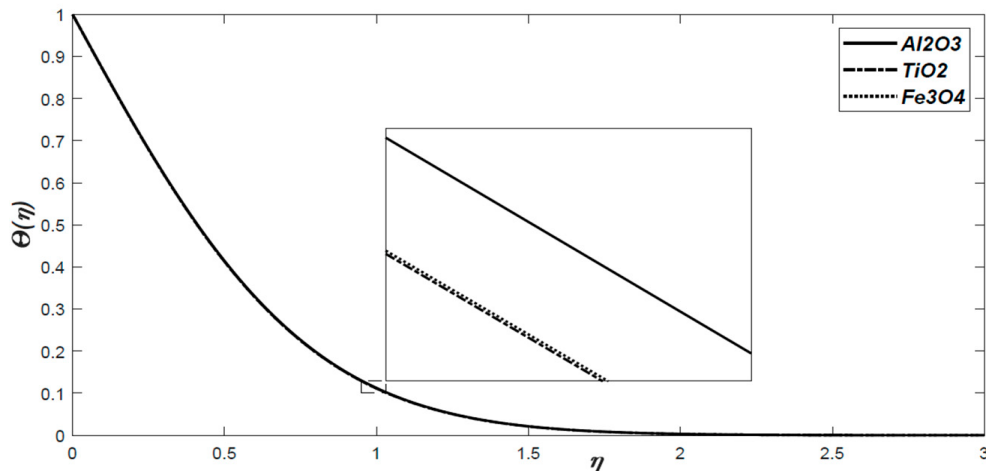


Figure 5.3 The dimensionless temperature profiles for  $\phi = 0.02$  for all three nanofluids

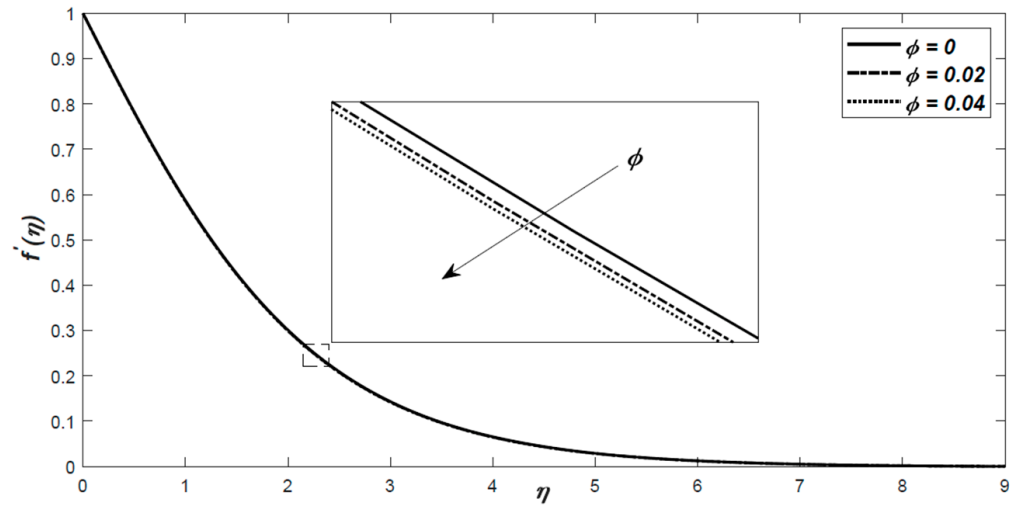


Figure 5.4. The dimensionless velocity profiles for  $\text{Al}_2\text{O}_3$ -water with respect to  $\eta$

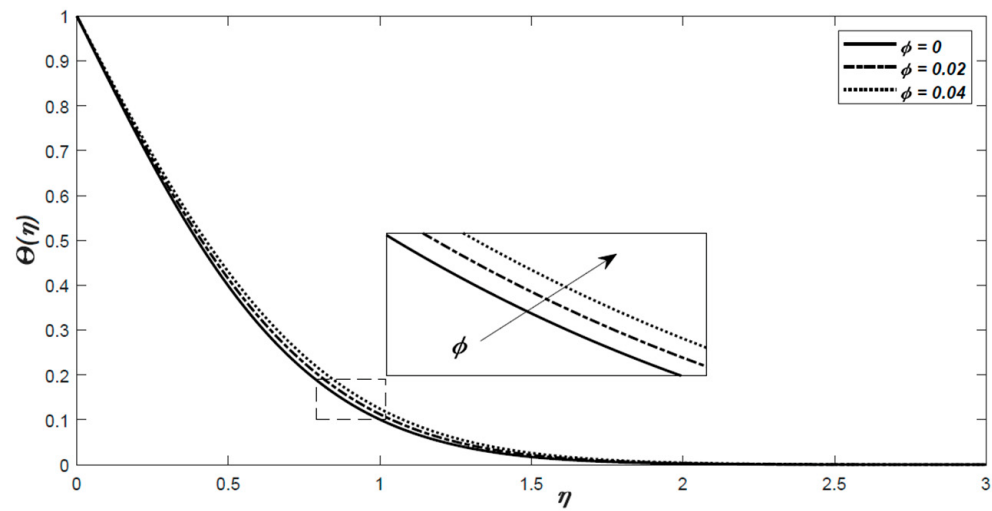


Figure 5.5. The dimensionless temperature profiles with - for  $\text{Al}_2\text{O}_3$ -water with respect to  $\eta$

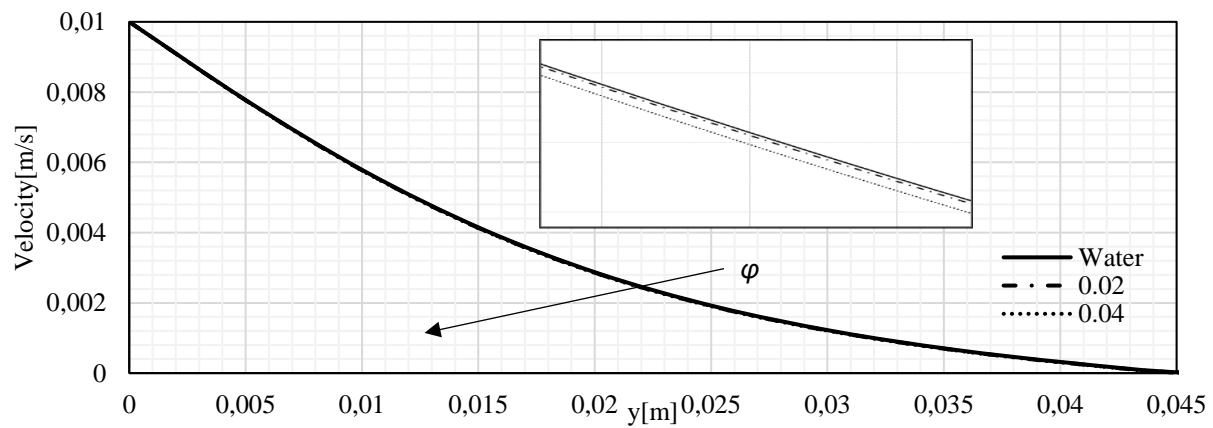


Figure 5.6. Velocity profile perpendicular to the sheet for  $\text{Al}_2\text{O}_3$ -water at different volume fractions

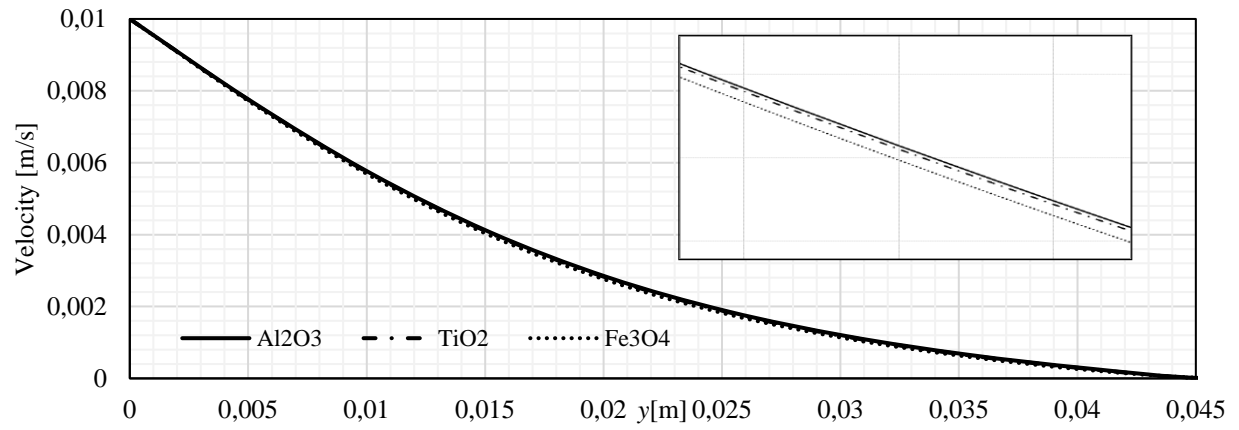
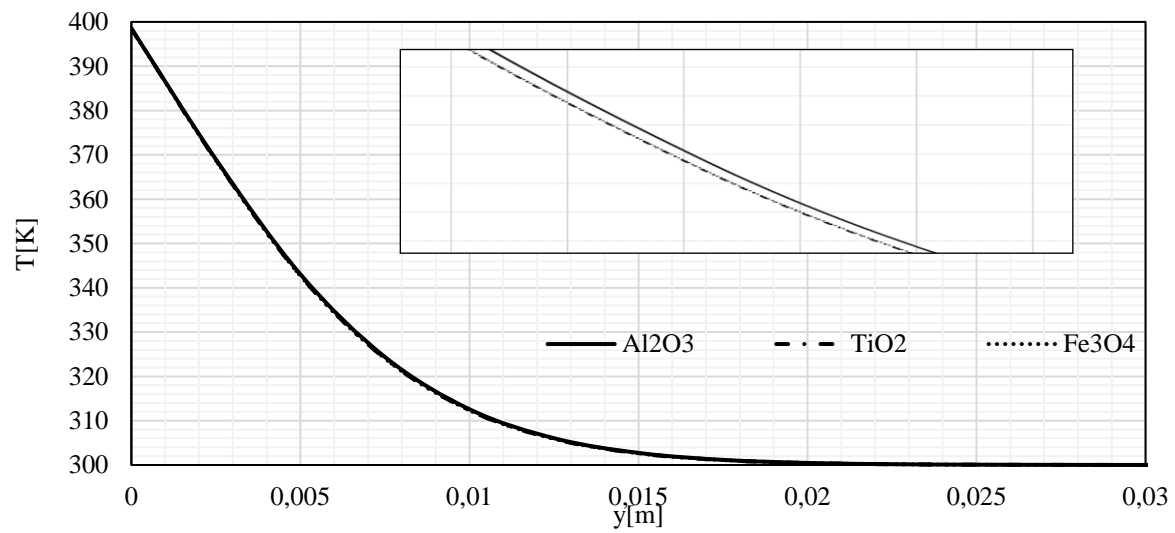
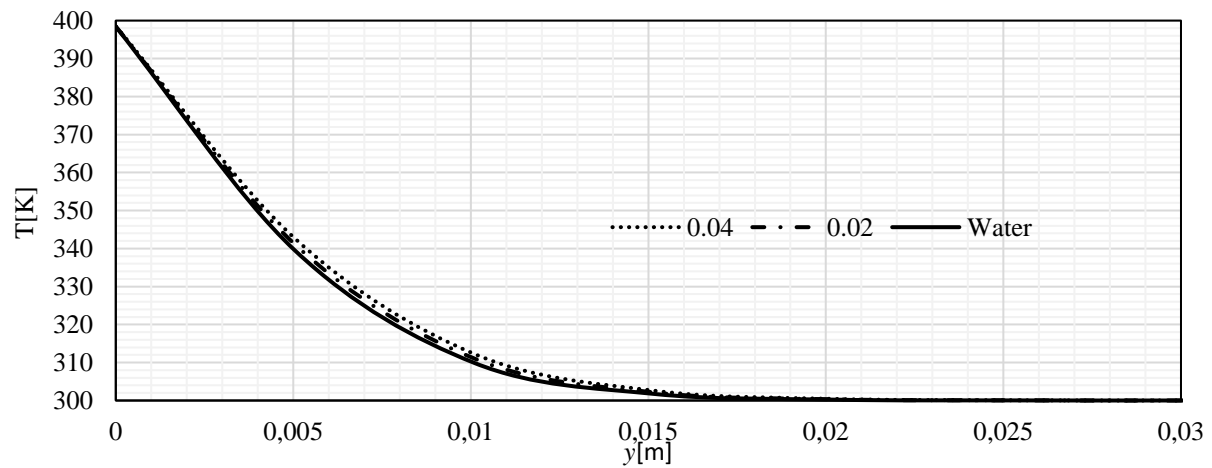
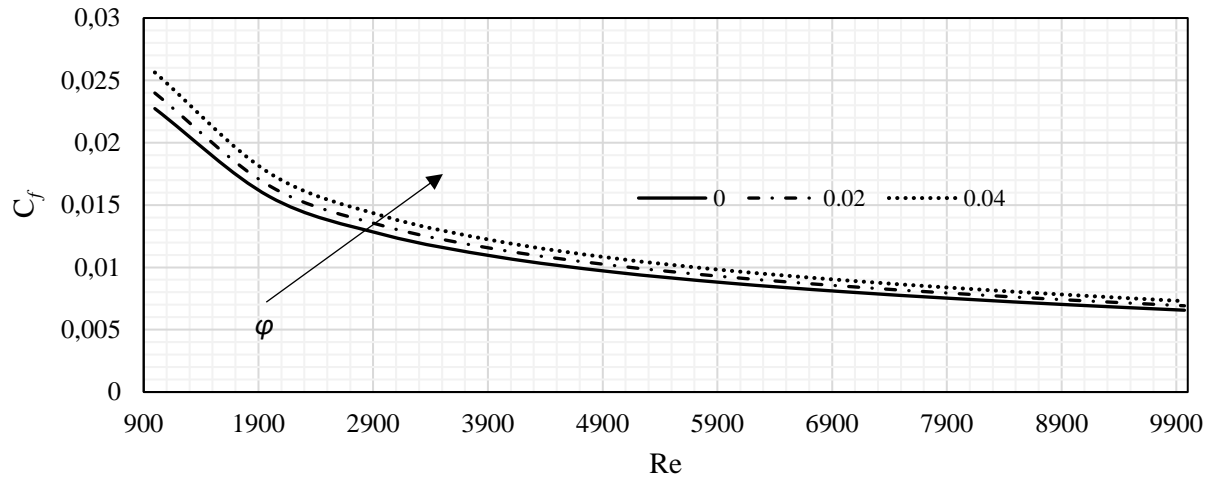
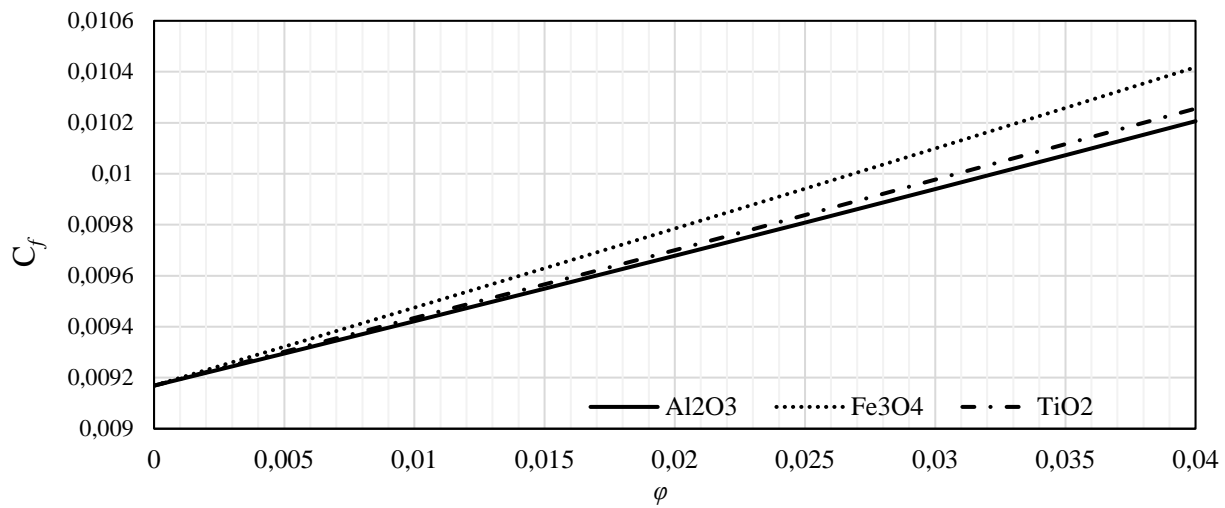
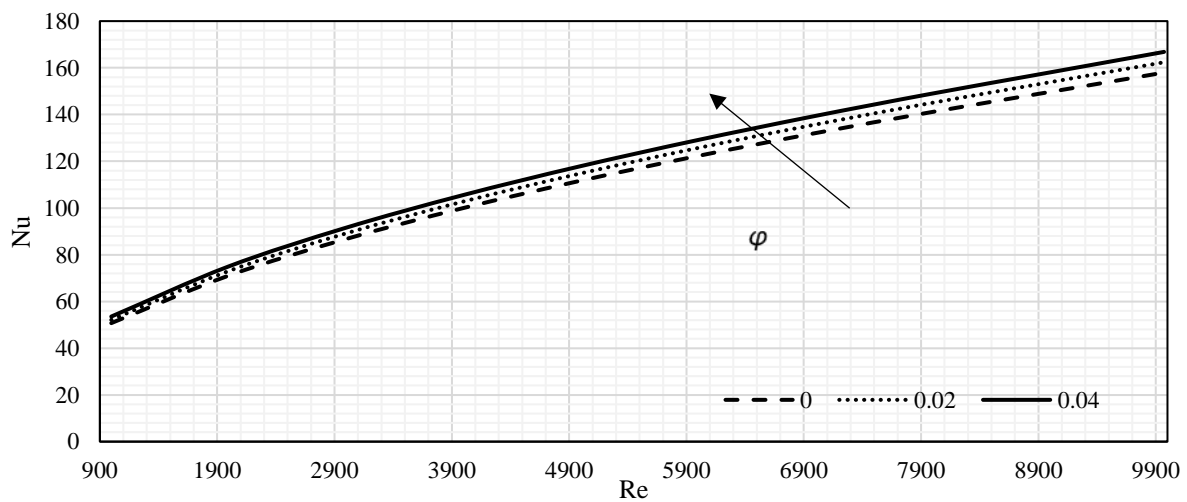


Figure 5.7. Velocity profiles for all three nanofluids at 0.02

Figure 5.8. Temperature profile perpendicular to the sheet for all three nanofluids  $\phi = 0.02$ Figure 5.9. Temperature profile perpendicular to the sheet for Al<sub>2</sub>O<sub>3</sub>-water at different volume fractions

Figure 5.10.  $C_f$  versus  $Re$  at different volume fractions ( $Al_2O_3$ )Figure 5.11. The skin friction versus  $\phi$  for all nanofluidsFigure 5.12. Variation of Nusselt number versus  $Re$  for  $Al_2O_3$ -water

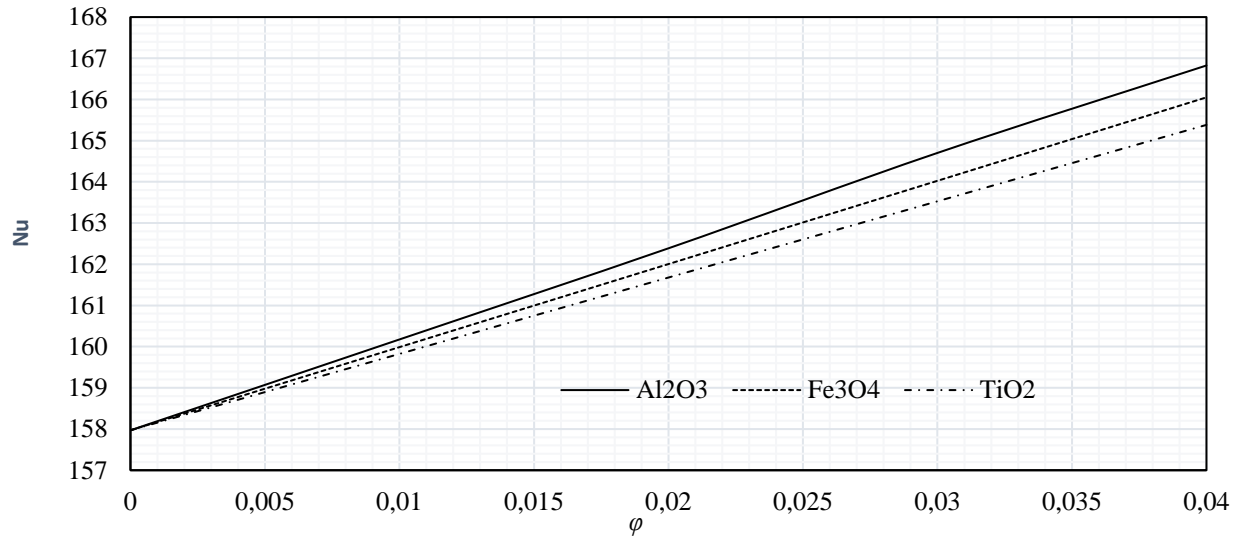


Figure 5.13 Variation of Nusselt number versus phi for all nanofluid

### 5.3 COMPARISON OF SIMILARITY AND CFD SOLUTIONS

The skin friction coefficient and the local Nusselt number are analysed using CFD simulations. Figure 5.11 exhibits the impact of the nanoparticle's material on  $C_f$  for  $\phi = 0.02$  along the flat surface. We found that the skin friction is higher Fe<sub>3</sub>O<sub>4</sub> than for Al<sub>2</sub>O<sub>3</sub> and TiO<sub>2</sub>. The skin friction coefficient variation with the Reynolds number is shown in Figure 5. 10 for Al<sub>2</sub>O<sub>3</sub> in the range of the corresponding Reynolds number. We can observe that the larger  $\phi$  is, the larger  $C_f$  is.

The effect of the nanoparticle's material on skin friction is examined in Figure 5.11, in the range 0.00–0.04. It was concluded that the highest values were obtained for Fe<sub>3</sub>O<sub>4</sub>, while the lowest was for Al<sub>2</sub>O<sub>3</sub>.

The variation of the Nusselt number along the sheet surface. A slight difference along the x-axis for all three nanofluids when  $\phi=0.02$  The bigger values for  $Nu$  were obtained for Al<sub>2</sub>O<sub>3</sub>.

The influence of the volume fraction on the local Nusselt number is investigated in Figure 5.12 for Al<sub>2</sub>O<sub>3</sub> in the range of Reynolds number 900–9000. It can be seen from the figure that the increase in  $\phi$  will induce an increase in the Nusselt number as well.

In Figure 5.13, the effect of the nanomaterial on the local Nusselt number is investigated. As the volume fraction increases, the local Nusselt number increases. However, the biggest values are obtained for Al<sub>2</sub>O<sub>3</sub>.

Table 5.1 and Table 5.2 show the comparison of  $Re_x^{1/2} C_f$  and  $Re_x^{-1/2} Nu$ , respectively. These values are determined by the similarity solutions with  $f''(0)$  and  $\theta'(0)$ , using the equations in (4.18) and with CFD simulations as well. We remark that in the range 0.00–0.02 for  $\phi$ , the values obtained with CFD

are slightly greater for both quantities than for the analytical solution obtained with the similarity method. However, the difference is small, less than 14.5%, and is especially small (2.7%) for  $Re_x^{1/2} C_f$ . The difference is due to boundary layer approximations. We consider that the CFD simulation results could be closer to the experimental results.

Table 5.1. Variation of  $Re_x^{1/2} C_f$  with  $\varphi$ 

$\varphi$	<b>Al<sub>2</sub>O<sub>3</sub></b>			<b>TiO<sub>2</sub></b>			<b>Fe<sub>3</sub>O<sub>4</sub></b>		
	<b>Similarity</b>	<b>CFD</b>	<b>%</b>	<b>Similarity</b>	<b>CFD</b>	<b>%</b>	<b>Similarity</b>	<b>CFD</b>	<b>%</b>
0.00	0.44455	0.45712	0.02749	0.44455	0.45712	0.02749	0.44455	0.45712	0.027498
0.01	0.45682	0.46971	0.02744	0.45743	0.47035	0.027469	0.45947	0.47238	0.02733
0.02	0.46929	0.48252	0.02741	0.47052	0.48361	0.027067	0.47458	0.48783	0.027161
0.03	0.48198	0.49556	0.027403	0.48382	0.49741	0.027322	0.48988	0.50349	0.027031
0.04	0.49490	0.50883	0.027376	0.49735	0.51129	0.027264	0.50540	0.51938	0.026917

Table 5.2. Variation of  $Re_x^{-1/2} Nu$  with  $\varphi$ .

$\varphi$	<b>Al<sub>2</sub>O<sub>3</sub></b>			<b>TiO<sub>2</sub></b>			<b>Fe<sub>3</sub>O<sub>4</sub></b>		
	<b>Similarity</b>	<b>CFD</b>	<b>%</b>	<b>Similarity</b>	<b>CFD</b>	<b>%</b>	<b>Similarity</b>	<b>CFD</b>	<b>%</b>
0.00	1.36704	1.58199	0.135873	1.36704	1.58199	0.135873	1.36704	1.58199	0.135873
0.01	1.38267	1.60408	0.138029	1.37974	1.60056	0.137964	1.38043	1.60221	0.138421
0.02	1.39833	1.62624	0.140145	1.39426	1.61913	0.138883	1.39387	1.62240	0.140859
0.03	1.41401	1.64942	0.142723	1.40520	1.63766	0.141946	1.40737	1.64264	0.143227
0.04	1.42975	1.67068	0.144211	1.41798	1.65624	0.143856	1.42093	1.66293	0.145526

The Sakiadis flow was investigated by determining the velocity and temperature in three types of nanofluids along a continuously moving sheet surface. The skin friction coefficient and the local Nusselt number were calculated. Two methods were used: one of them was analytically applying the traditional Blasius' similarity transformation and solving the obtained coupled ordinary differential equations; the other solution was obtained using CFD simulations. We found that the solid volume fraction significantly influences the fluid flow and heat transfer properties. Comparing the three nanoparticles' materials, we note that the  $\text{Al}_2\text{O}_3$  has significantly greater thermal conductivity. The larger velocity and temperature values are obtained in the boundary layer for alumina–water fluid than for the other two nanomaterials. Increasing the concentration of nanomaterials has produced a decrease in velocity and an increase in temperature in the momentum and thermal boundary layers, respectively. The skin friction decreases, and the Nusselt number increases with the Reynolds number. The values of  $C_f$  and  $Nu$  are depicted with the nanoparticle concentration. It was concluded that both linearly increase with. For  $\text{Al}_2\text{O}_3$ , the values of the skin friction coefficient are smaller than for titania ( $\text{TiO}_2$ ) and magnetite ( $\text{Fe}_3\text{O}_4$ ); conversely, the Nusselt number values are greater than those for the other two materials. It was found that the type of nanofluid is a key factor in improving heat transfer. The behaviour of the skin friction coefficient and the local Nusselt number is like that described by Ahmad et al. [108] and Bachok et al. [109]. The simulation results obtained by CFD gave lightly bigger values for  $Re_x^{1/2}C_f$  and  $Re_x^{-1/2}Nu$ , which indicates that the skin friction should be slightly higher in reality than the value calculated, according to boundary layer theory.



## 6. BACKWARD-FACING STEP (FLUID WITH TEMPERATURE-DEPENDENT PROPERTIES)

This section provides a numerical study of laminar flow in a micro-sized backward-facing step channel for water-based nanofluids containing  $\text{Al}_2\text{O}_3$  and  $\text{TiO}_2$  nanoparticles. We investigate the impact of the temperature differences between the inlet and the downward wall temperatures. In this section we introduce a temperature-dependent separation flow model.

### 6.1 PROBLEM DESCRIPTION

The two-dimensional flow geometry with BFS is presented in Figure 6.1. The laminar forced heat transfer flow will be investigated numerically. For the expansion ratio: 1.6667 was chosen in the geometry similarly as in [110]. The length of the downstream wall is  $L_d$ , and the upstream wall is  $L_u$ .  $H$  denotes the channel height downstream, and  $h$  is the height of the inflow channel. In the present study, the downstream wall is heated with constant heat flux, and the other walls are isothermal. For the case of temperature difference, the wall has a uniform temperature  $T_w$ . The other walls are insulated. The applied boundary conditions are summarized in Table 6.1. A single-phase approach will examine the solid particles in the nanofluid. Heat transfer and fluid flow properties are investigated in a two-dimensional, steady, laminar flow in the channel for non-compressible fluid.

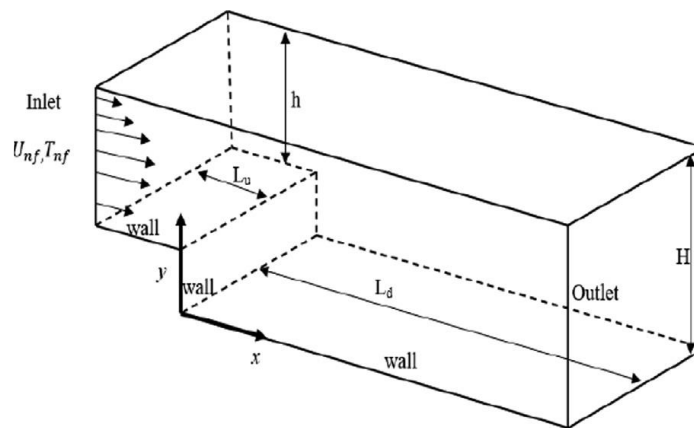


Fig. 6.1. Schematic diagram for the horizontal backward-facing step.

Table 6.1. Geometric data.

Notion	$L_d$	$L_u$	$s$	$h$	$H$	$T_w$	$T_{nf}$
Value [unit]	0.15[m]	0.1[m]	600[ $\mu\text{m}$ ]	400[ $\mu\text{m}$ ]	1000[ $\mu\text{m}$ ]	depend on case	274[K]

## 6.2 EXPERIMENTAL BACKGROUND

The experimental works on the heat transfer enhancement for water-based nanofluids were studied and reported by Kherbeet et al. [110]. Figure. 6.2 shows the experimental system of Kherbeet et al. The experiment consists of 0.25 m length of the annular aluminium duct. 1000  $\mu\text{m}$  inner diameter has been used as testing section the tested nanofluid flows inside the inner duct. The bottom wall of the test section was heated to provide a uniform heat flow through a heater connected to a digital power supply. The liquid is kept in a container and contacted with a high-pressure water pump. A microfilter is placed between the container and the pump to filter the nanofluid, preventing large nanoparticles from entering the channel. Two shafts are fixed at each end of the test section. Two valves are connected to the line between the pump and the inlet tank to control the flow rate and the other to reduce the high pressure in the return pipe to the tank. There are two digital pressure gauges at the inlet and outlet of the duct to measure the pressure drop along the duct. Seven thermocouples were used in the axial position downward. The mass flow rate of the test fluid was measured by a micro flow meter placed at the outlet of the duct. The temperature of the outlet tested fluid was reduced using a water heat exchanger before returning into the tank. At the outlet of the duct, a micro flowmeter is located.

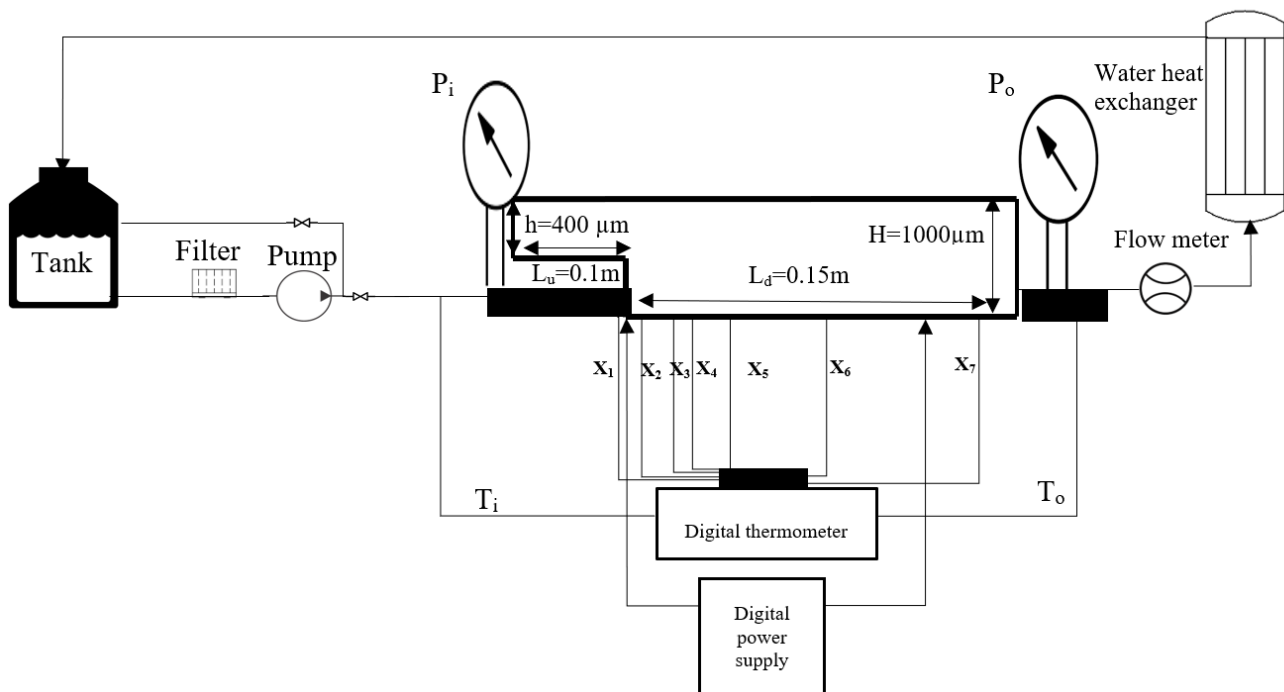


Figure 6.2. The schematic diagram of the experimental setup

### 6.3 GOVERNING EQUATIONS

In this model, it is assumed that the nanofluid is a homogeneous liquid. The following assumptions are used [111]:

- The flow is two dimensional steady-state,
- The fluid flow is laminar,
- The fluid and nanoparticles' phases are in thermal equilibrium,
- The relative velocity between the fluid and nanoparticles phases is zero.

Equations (3.1) to (3.3) represent the mathematical formulation of continuity, momentum, and energy used in a single-phase model.

### 6.4 NUMERICAL PROCEDURE AND MESH INDEPENDENCE TEST

In this study, the continuity, momentum, and energy equations are solved numerically using ANSYS Workbench R18.1. The thermal properties of various volume fractions for the nanofluids are introduced by writing a source code in C language and imported into ANSYS fluent as user-defined function (UDF). Mesh generation was done with ANSYS meshing. Seven meshes of various grids are checked to ensure the precision and accuracy of computation results. The edges of the geometry were divided using the number of division method. The grid is finer near the wall, with a base ratio of 10 for the inlet and outlet walls and near the step 30 and 20 for the steam wall and downstream wall, respectively. The outcome of the mesh independence test demonstrates that mesh 5 is satisfactory for resolving the analyzed parameters. The number of the elements is presented in Table 6.2 with an independent mesh test for friction and pressure. Figure 6.3 present the mesh independency study. It shows the prediction values of heat transfer with corresponding number of elements.

Table 6.2. Mesh independency test

Mesh	Element	Grid dy, dx, dy, dx	Friction factor	Pressure [Pa]
1	10000	20*100*40*200	0.0347	94.75
2	25000	25*200*50*400	0.0349	94.89
3	45000	30*300*60*600	0.0350	94.93
4	70000	35*400*70*800	0.0350	94.96
5	100000	40*500*80*1000	0.0350	94.88
6	135000	45*600*90*1200	0.0350	94.89
7	175000	50*700*100*1400	0.350	94.9

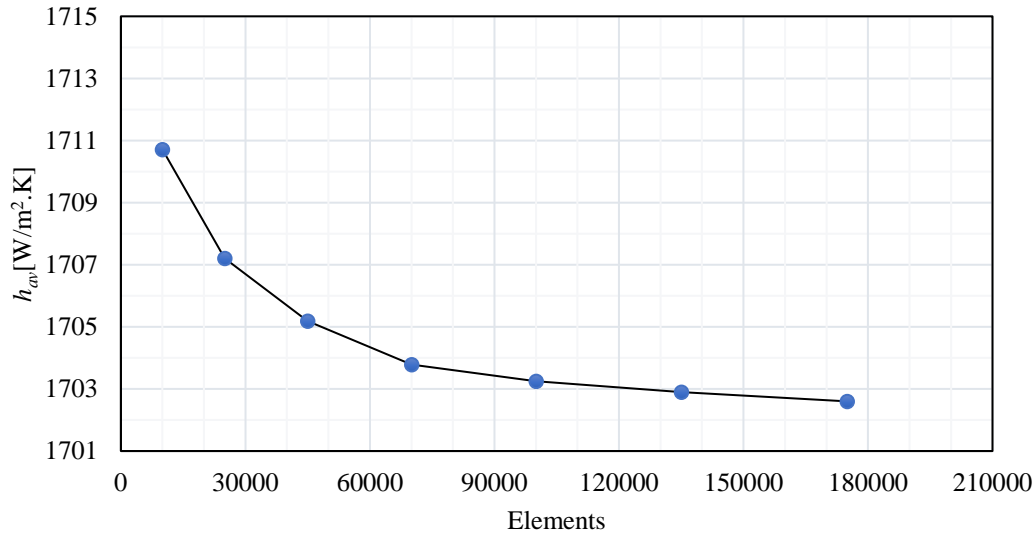


Figure 6.3. Mesh independency study

## 6.5 VALIDATION

The present numerical solution is validated with different previous studies, as shown in Figs..6.4–6.7. The first study used in the validation process presents the fluids' thermophysical properties and UDF code by comparing the prediction values with experiment results. The viscosity of distilled water and  $\text{Al}_2\text{O}_3$  was validated by comparing the result with the experiment data and ASHARE data [112], [113]. The second study by Al-Aswadi et al. [114]. They used different nanofluids as working fluids with  $\text{Re} = 175$ . All the presented results were completely identical, as shown in Fig.6.6, respectively. In addition, the Nusselt number at different  $\text{Re}$  numbers was compared with the experimental results for water [110], and the result shows a good agreement (see Fig.6.5). Eq. (6.1) is used to compute the local heat transfer coefficient (HTC), and Eq. (6.2) and (6.3) are used to calculate the average HTC and local Nusselt number, respectively,

$$h_x = \frac{q}{(T(x)_w - T(x)_b)}, \quad (6.1)$$

$$h_{\text{avg}} = \frac{1}{L} \int_0^L h(x) dx, \quad (6.2)$$

$$\text{Nu}_{nf} = \frac{h_{\text{avg}} D_h}{k_{nf}}. \quad (6.3)$$

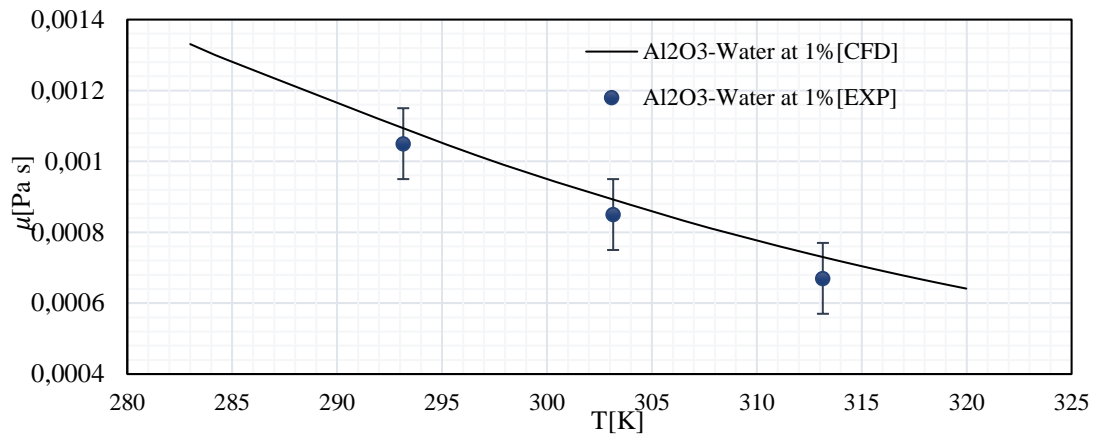


Figure 6.4. Comparison with the experimental viscosity data and ASHARE data(water) [112]

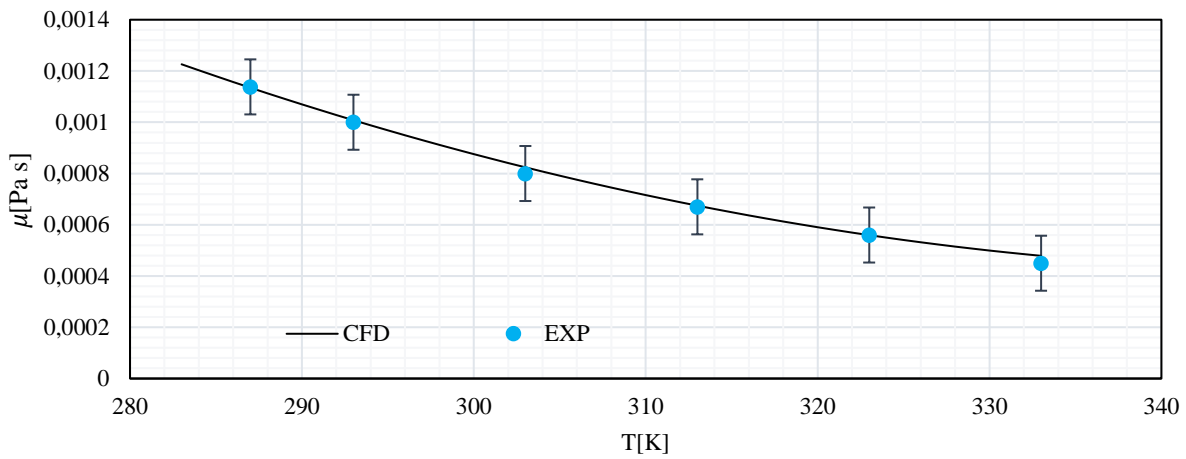
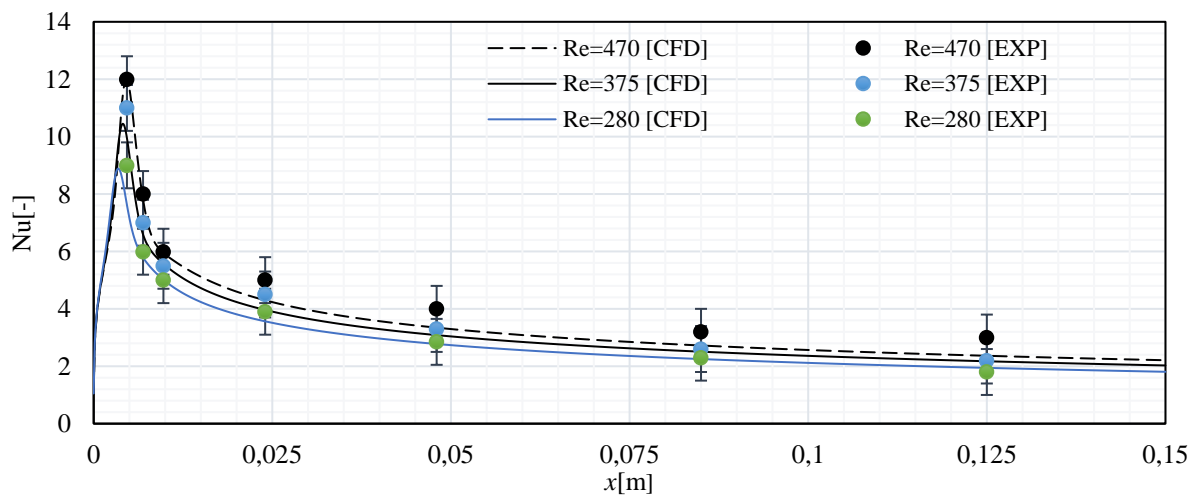
Figure 6.5 Comparison with the EXP for  $\text{Al}_2\text{O}_3$  -water at 1%

Figure 6.6. Comparison of Nu with experimental data at different Re = 470

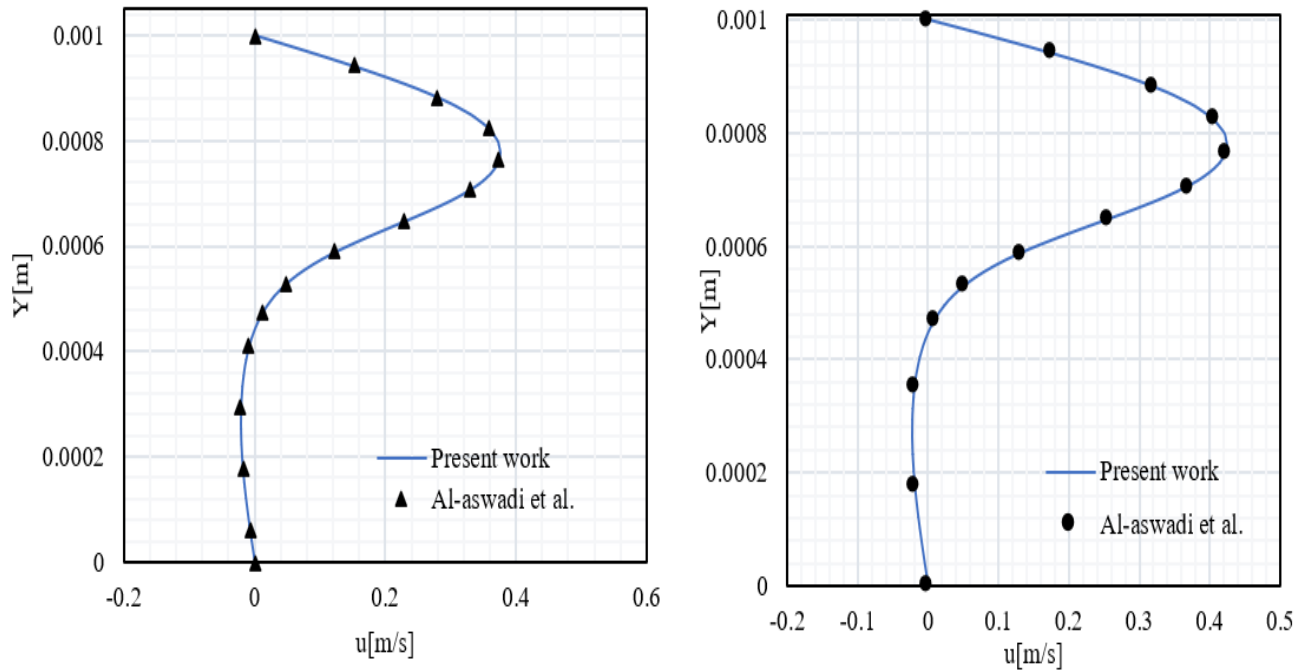


Figure 6.7. Comparison of velocity distributions with the results of Al-Aswadi et al. [114]

(Re = 175)

## 6.6 TEMPERATURE-DEPENDENT PROPERTIES

The change in the viscosities is presented, and the effect of the particle's concentration in the vertical direction at different locations is plotted in Fig. 6.8. The result shows that viscosity depends on the particle's concentration. As the volume fraction increases, the viscosity increases. The change of the nanofluids' viscosities shows the same trends at  $x = 0.1$  and  $x = 0.15$ . The highest viscosity value is reported for  $\varphi = 4\%$ . Fig. 6.9 presents the change in viscosity along the downstream wall for the nanofluids at different volume fractions. It can be seen that the viscosity increases gradually at the start of the recirculation zone and reaches its maximum value at the reattachment point. The values of the viscosity are different according to the volume fraction. The change in viscosity can be due to two reasons. The first one is the effect of the volume fraction, and the second one is the variation of the temperature along the wall.

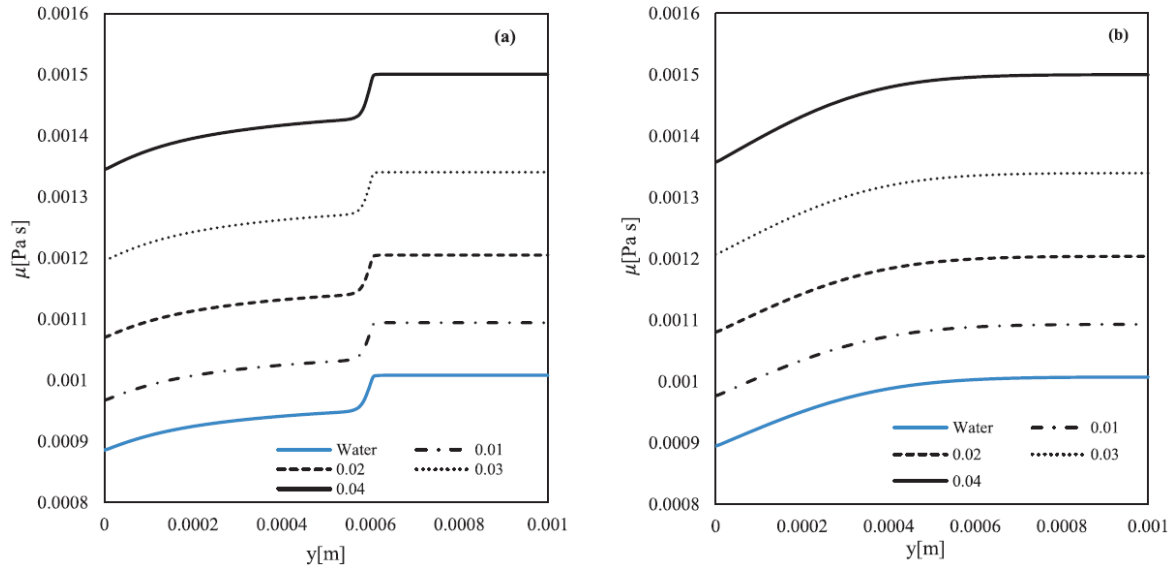


Fig. 6.8. Dynamic viscosity along  $y$  for  $\varphi = 0, 0.01, 0.02, 0.03, 0.04$ . (a) dynamic viscosity at the step, (b) dynamic viscosity at outlet

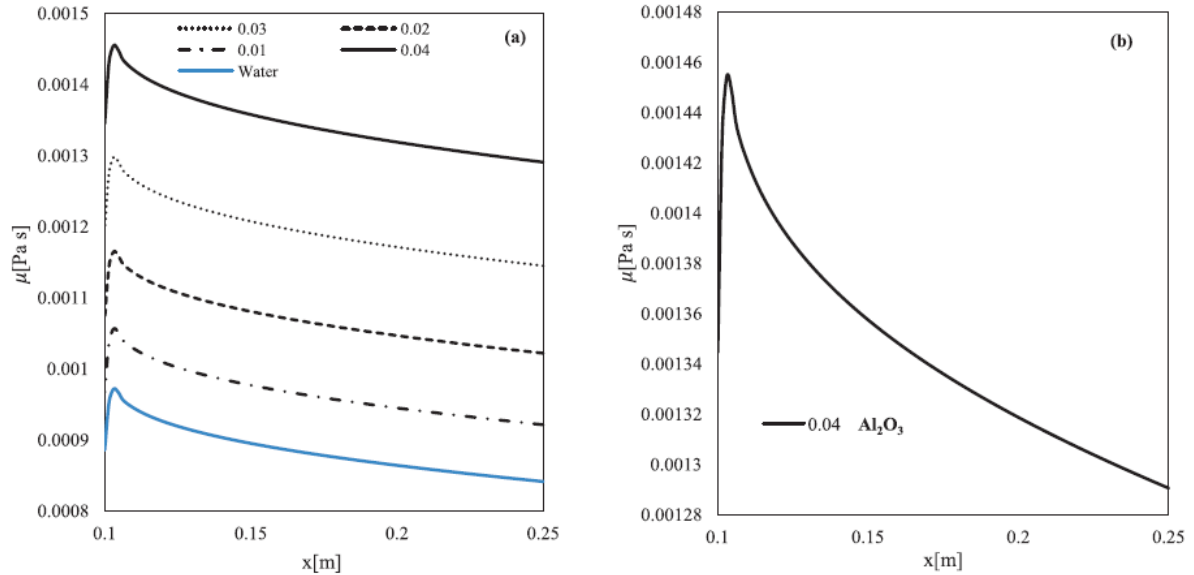


Figure 6.9. Dynamic viscosity along  $x$  for  $\text{Al}_2\text{O}_3$ . (a) dynamic viscosity for  $\varphi = 0, 0.01, 0.02, 0.03, 0.04$  ( $y=0$ ), (b) dynamic viscosity at  $\varphi=0.04$

The velocity distributions of the  $\text{Al}_2\text{O}_3$  nanofluid for various volume fractions are plotted for  $\text{Re} = 280$  at different cross-sections along the downstream wall in Fig. 6.10 until 4% of additives. The velocity increases as the nanofluid density increases. For a given Reynolds number, all the parameters are calculated to keep the Reynolds number constant. The velocity will be changing to keep the Reynolds number constant. The active role of the nanoparticle's volume fraction is obvious on the velocity distribution. The velocity increases with the increase in the nanoparticles' concentration. For  $\text{Re} = 280$

the lowest velocity distribution was obtained for water. Also, it was observed that there is no significant effect on the length of the reattachment point with increasing the nanoparticle's concentration or different nanoparticle's types at a constant Reynolds number. However, a comparison of the velocity profiles of  $\text{Al}_2\text{O}_3$  and  $\text{TiO}_2$  nanofluids of 0.04 volume fraction shows a higher velocity for  $\text{Al}_2\text{O}_3$  than for  $\text{TiO}_2$ , as can be seen in Fig. 6.10-d. At the downstream wall in the recirculation zone, the flow shows negative velocity near the downstream wall (Fig. 6.10-b). It reports a developed recirculation zone downstream the step. The velocity gradients are bigger in the negative sense for nanofluid with high volume fraction (i.e., the velocity gradients increase in the negative sense as  $\phi$  increases). In the downstream region after the recirculation zone, the flow starts to redevelop and approach a fully developed flow as the fluid flows towards the outlet.

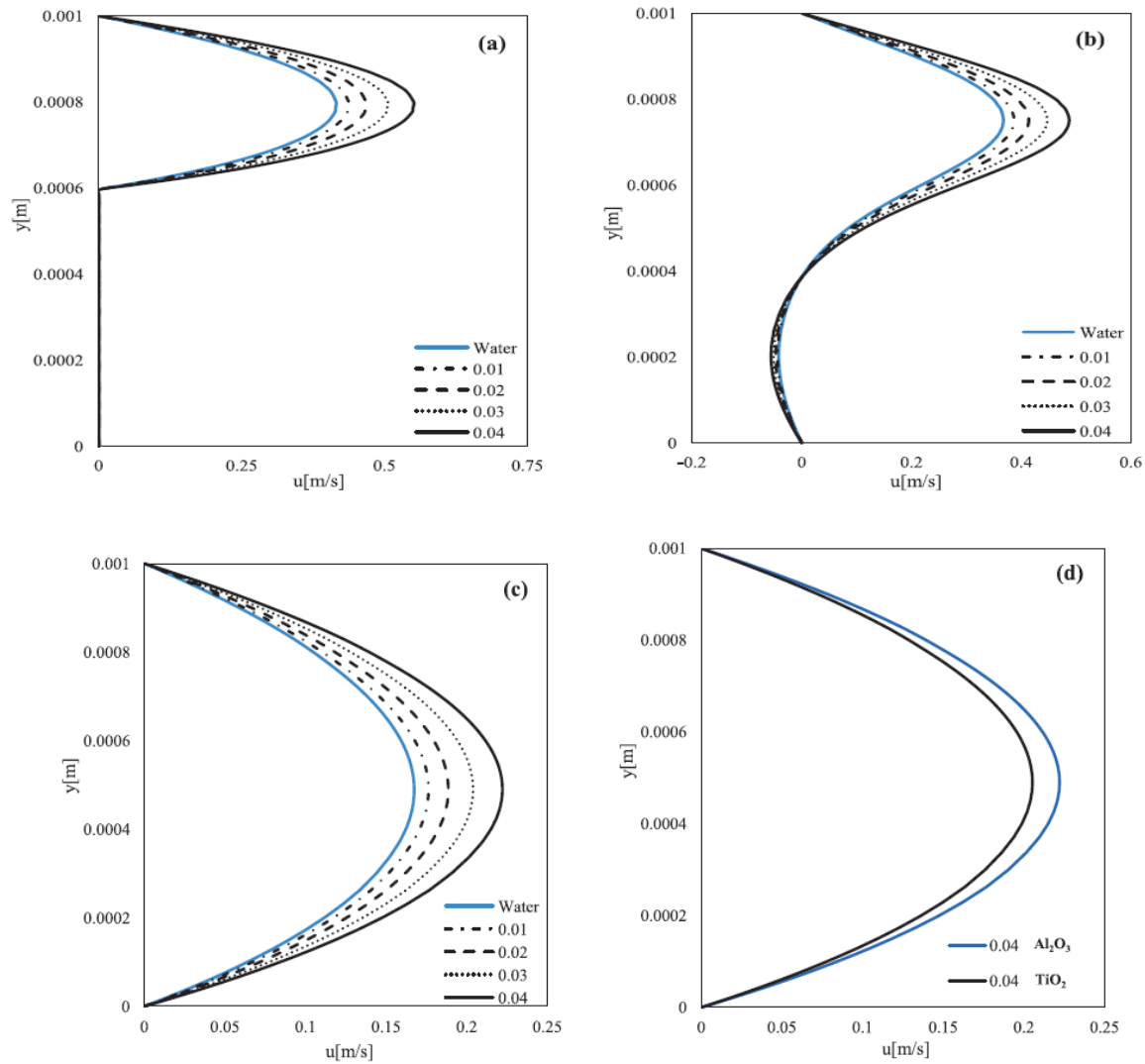


Figure 6.10. The velocity distribution of  $\text{Al}_2\text{O}_3$  nanofluid for  $\phi = 0, 0.01, 0.02, 0.03, 0.04$  (a)  $\text{Al}_2\text{O}_3$  at the step, (b)  $\text{Al}_2\text{O}_3$  at recirculation zone ( $x=0.15$ ), (c)  $\text{Al}_2\text{O}_3$  at the outlet, (d),  $\text{Al}_2\text{O}_3$  and  $\text{TiO}_2$  at the outlet for  $\phi = 0.04$



The sign of the wall shear stress presents the flow direction along the downstream wall, indicating that the particle concentration and particle type do not change the length of the reattachment point. As the volume fraction increased, the value of the wall shear stress became larger with taking the constant value of  $Re$  (see Fig. 6.11-a). Fig. 6.11-b presents the wall shear stress for constant  $Re$  and for 0.04 volume fraction for the two types of nanofluids. A comparison between the two nanofluids shows that  $Al_2O_3$  nanofluid has a higher wall shear stress than  $TiO_2$  along the downstream wall. In Fig. 6.12-a. The variation of the temperature at the downstream wall is plotted for constant Reynolds number  $Re = 280$ .

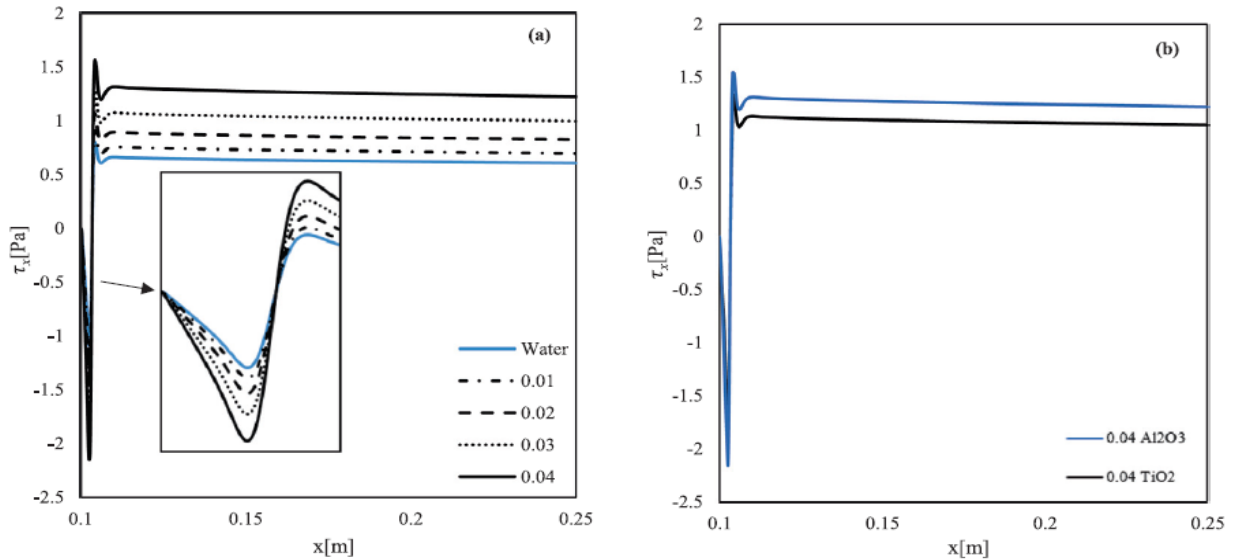


Figure 6.11. The wall shear stress. (a)  $Al_2O_3$  along the downstream for  $\phi = 0, 0.01, 0.02, 0.03, 0.04$ , (b)  $Al_2O_3$  and  $TiO_2$  along downstream for  $\phi = 0.04$

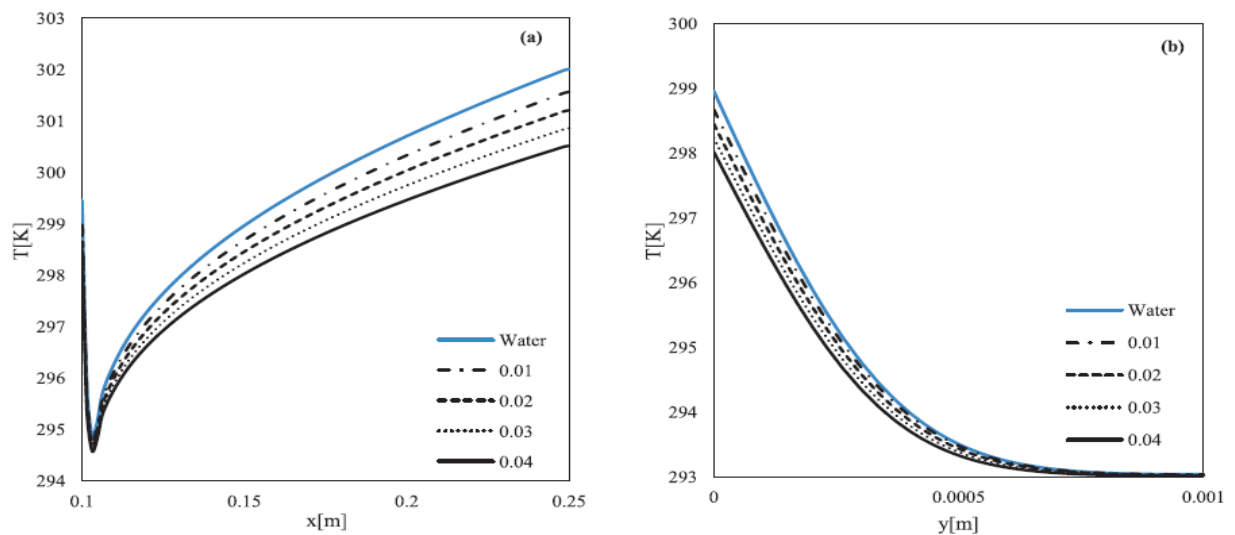


Figure 6.12 The temperature distribution for  $\phi = 0, 0.01, 0.02, 0.03, 0.04$  (a) along downstream wall  $y=0$ , (b) at the outlet  $x=0.25$

The result shows that the temperature is strongly affected by the volume fraction. The increase in the concentration shows a significant decrease in the temperature along the downstream wall. Additionally, higher heat transfer is achieved with the increase in the volume fraction at the downstream wall. The thermal boundary layer at the outlet is presented in Fig. 6.12-b. The impact of the volume fraction on the  $\text{Al}_2\text{O}_3$  nanofluid with different volume fractions on temperature profile report that the increase in the volume fraction decreases the thickness of the thermal boundary layer.

The comparison of the temperature contours for water and nanofluids of different volume fractions has been presented in Fig. 6.13. The temperature contour for the water fluid results in higher temperatures compared with the contour of the  $\text{Al}_2\text{O}_3$  nanofluids for all tested volume fractions. This observation is clear at the outlet section. The difference between the contours is due to the improvement of the thermal properties with the increase of the volume fraction, meaning that the heat transfer rate between the wall and the fluid is higher.

Fig.6.14 presents the impact of the volume fraction on the heat transfer. The result exhibits that the heat transfer along the downstream wall has improved significantly with increasing the volume fraction. Among the tested nanofluids,  $\text{Al}_2\text{O}_3$  nanofluid fluid for all volume fractions shows a higher heat transfer value than water and  $\text{TiO}_2$ . The relationship between heat transfer and volume fraction is strong. Heat transfer was significantly sensitive to volume fraction increase and nanoparticle type.

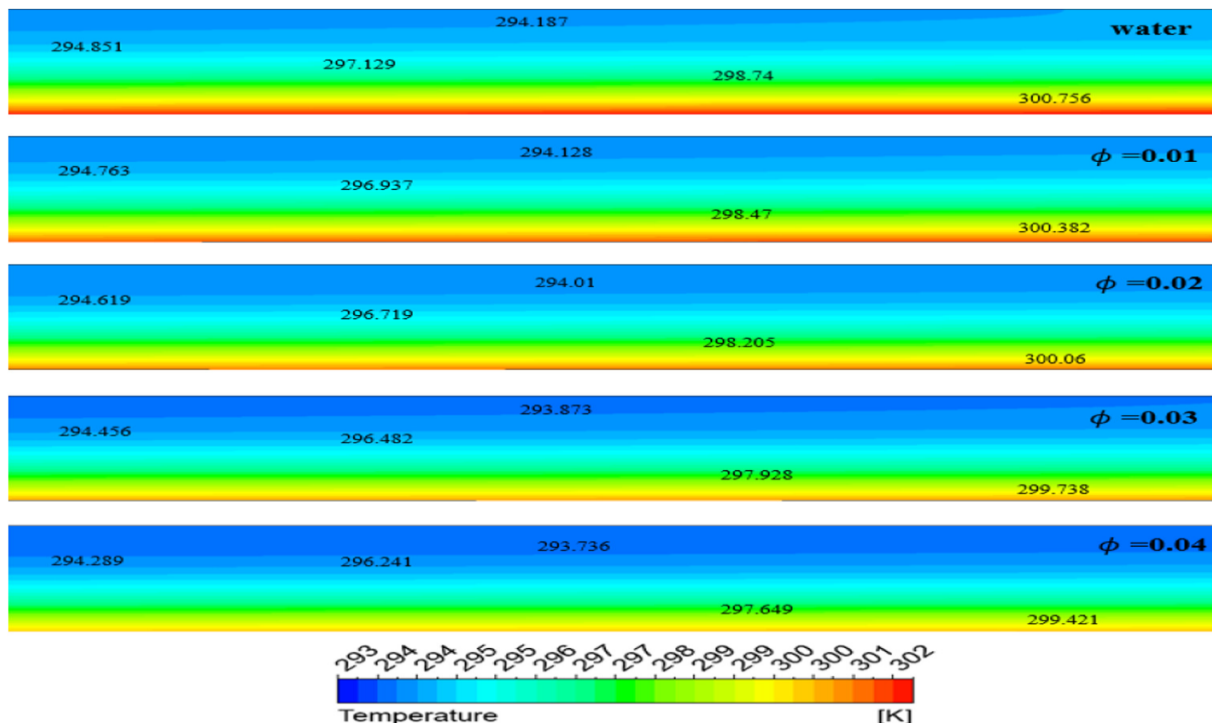


Figure 6.13. Temperature contour for different  $\phi$  at the downstream wall for  $\text{Al}_2\text{O}_3$ .

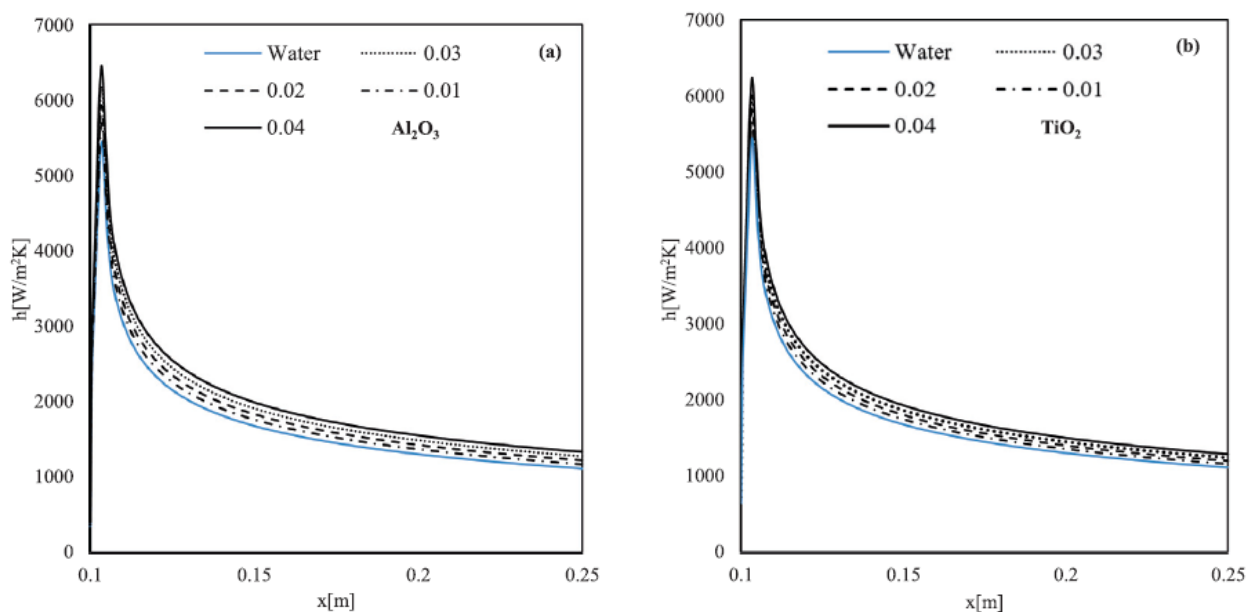


Figure 6.14. The average heat transfers along downstream wall

Table 6.3 compares the average heat transfer coefficient along the downstream wall for  $\text{Al}_2\text{O}_3$  and  $\text{TiO}_2$  for various volume fractions, showing that  $\text{Al}_2\text{O}_3$ -water has higher heat transfer enhancement than that of  $\text{TiO}_2$  for all volume fractions. According to the graph, the heat transfer gradually increased after the step until it reached a peak at the reattachment point.

The increase and decrease in heat transfer is due to the change in thermal conductivity. Fig. 6.15 reports the change in the thermal conductivity. It can be observed that the thermal conductivity increases as the volume fraction increases resulting in higher fluid conductivity. The velocity profiles of the nanofluid with a concentration of 0.04 at  $\text{Re} = 280$  with various temperature differences  $\Delta T = 0, 10, 20$ , and 30 at different locations along the wall  $L_d$  are presented in Fig. 6.16. The temperature difference of the inlet fluid and the downstream wall is denoted by  $\Delta T$ . At the step, the flow separates due to the sudden expansion. Then, above the step, the flow develops a parabolic flow, and the magnitude of the velocity increases as the temperature difference increases. After the step and downstream of the flow, a recirculation zone develops, where the flow is reversed. Our results show that also the change of the magnitude of the velocity is significant due to the temperature difference. Higher negative values are reported inside the recirculation zone and higher positive velocity values above the recirculation zone as the temperature difference increases. The effect of temperature difference on flow can be a function of temperature on the physical properties of nanofluids.

Table 6.3. Comparison between the average heat transfer coefficient along the downstream wall for  $\text{Al}_2\text{O}_3$  and  $\text{TiO}_2$ .

Volume fraction	$\text{Al}_2\text{O}_3$	$\text{TiO}_2$
0.01	1787.874	1772.205
0.02	1861.957	1830.466
0.03	1940.642	1892.926
0.04	2024.164	1960.240

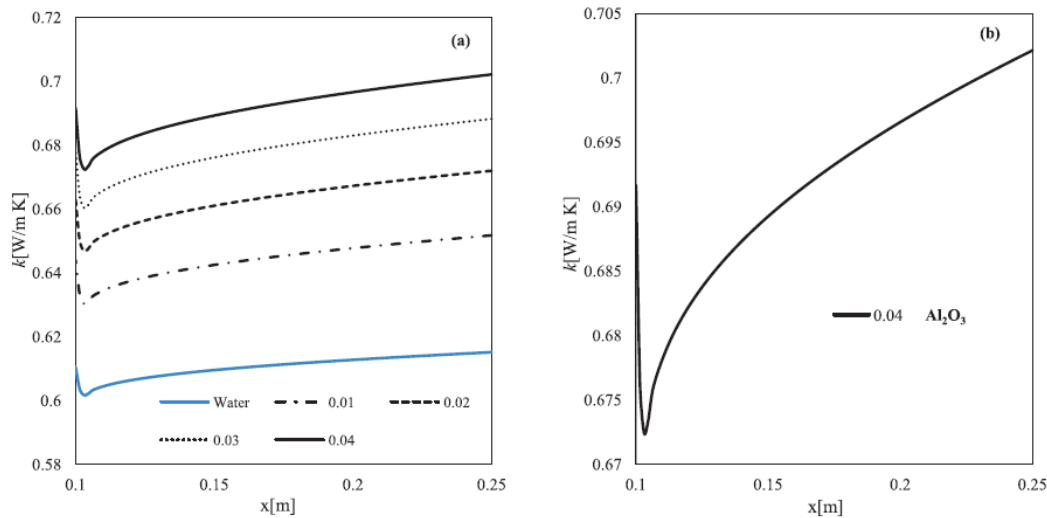
Figure 6.15. Thermal conductivity (a) for  $\text{Al}_2\text{O}_3$  along downstream wall for  $\phi = 0, 0.01, 0.02, 0.03, 0.04$ , (b)  $\text{Al}_2\text{O}_3$  at  $\phi = 0.04$ 

Fig. 6.16-c shows that the parabolic flow is to some extent bent toward the warm fluid above the downstream wall. Higher temperature difference reports greater bend. Fig. 6.16-d shows that the flow started to redevelop and became a fully parabolic profile at the outlet.

Figures 6.17 and 6.18 show the velocity streamlines and temperature contours of the  $\text{Al}_2\text{O}_3$  nanofluid with volume fraction 0.04 for  $\Delta T = 10, 20$ , and 30 K, respectively. The recirculation area turns up, and the size of the recirculation region  $X$  increases as the temperature difference increases. After the reattachment region, the flow starts to become fully developed parabolic flow. The comparison also shows that the secondary recirculation region has a bigger size for  $\Delta T = 30$  than for  $\Delta T = 10$ .

The wall shear stress for various temperature differences is presented in Fig. 6.19. It is found that wall shear stress decreases as the temperature difference increases. It was observed that wall shear stress is also sensitive to the vortices and recirculation regions. It can be seen that the wall shear stress decreases from the wall step until it reaches its minimum value in the recirculation region. Then, the

wall shear stress increases until it reaches its maximum peak value at the reattachment point. Then, it slightly decreases and increases until it reaches an almost constant value. The heat transfer rate along the stepped wall is plotted for different  $\Delta T$  with volume fraction 0.04 in Fig. 6.20. It can be seen that the fluid for higher temperature differences has a higher heat transfer rate along the downstream wall. It increases readily until it reaches its maximum at the reattachment point, and the highest peak value in the heat transfer was found for  $\Delta T = 30$ . After the peak, the heat transfer started to decrease. The increment and the decrements in the heat transfer rate and in wall shear stress can be due to the development of the vortex and the temperature difference.

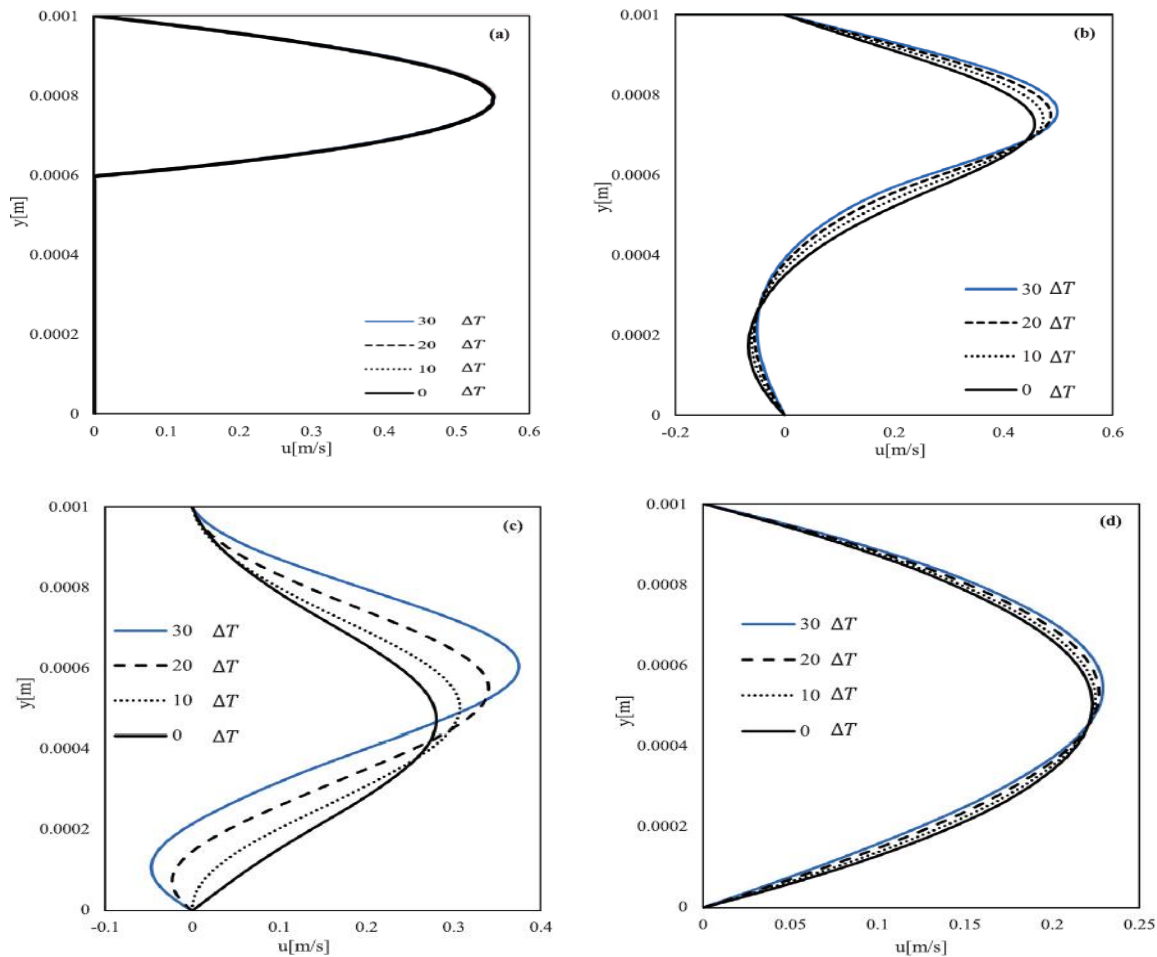


Figure 6.16 The velocity distribution of  $\text{Al}_2\text{O}_3$  nanofluid for different  $\Delta T$  (a)  $\text{Al}_2\text{O}_3$  at the step, (b)  $\text{Al}_2\text{O}_3$  at recirculation zone, (c)  $\text{Al}_2\text{O}_3$  ( $x=0.104$ ), (d),  $\text{Al}_2\text{O}_3$  at the outlet

Parameters such as the viscosity and thermal conductivity of the nanofluid are strongly affected by temperature variations. The decrease in viscosity of the nanofluid can be attributed to factors such as the movement of nanoparticles in the micron dimension. Studies show that the microconvection of nanoparticles in the base fluid reduces the intermolecular forces between the molecules of the base fluid.

As the temperature increases, the molecular velocity of the nanoparticles increases due to the Brownian motion of the nanoparticles [115]. Therefore, it is superficial that the Brownian motion of the nanoparticles increases with increasing temperature in the base fluid. Thus, an increase in the random velocity of the nanoparticles leads to a decrease in the intermolecular forces between the base fluid and the nanoparticle surface, and consequently to a higher viscosity at lower temperatures. This phenomenon has led to an increase in velocity with increasing volume fraction, resulting in higher heat transfer. The effect of temperature was clearly observed at different temperature differences, where the higher velocity and heat transfer observed at higher temperatures led to lower shear stress and higher thermal conductivity due to lower viscosity.

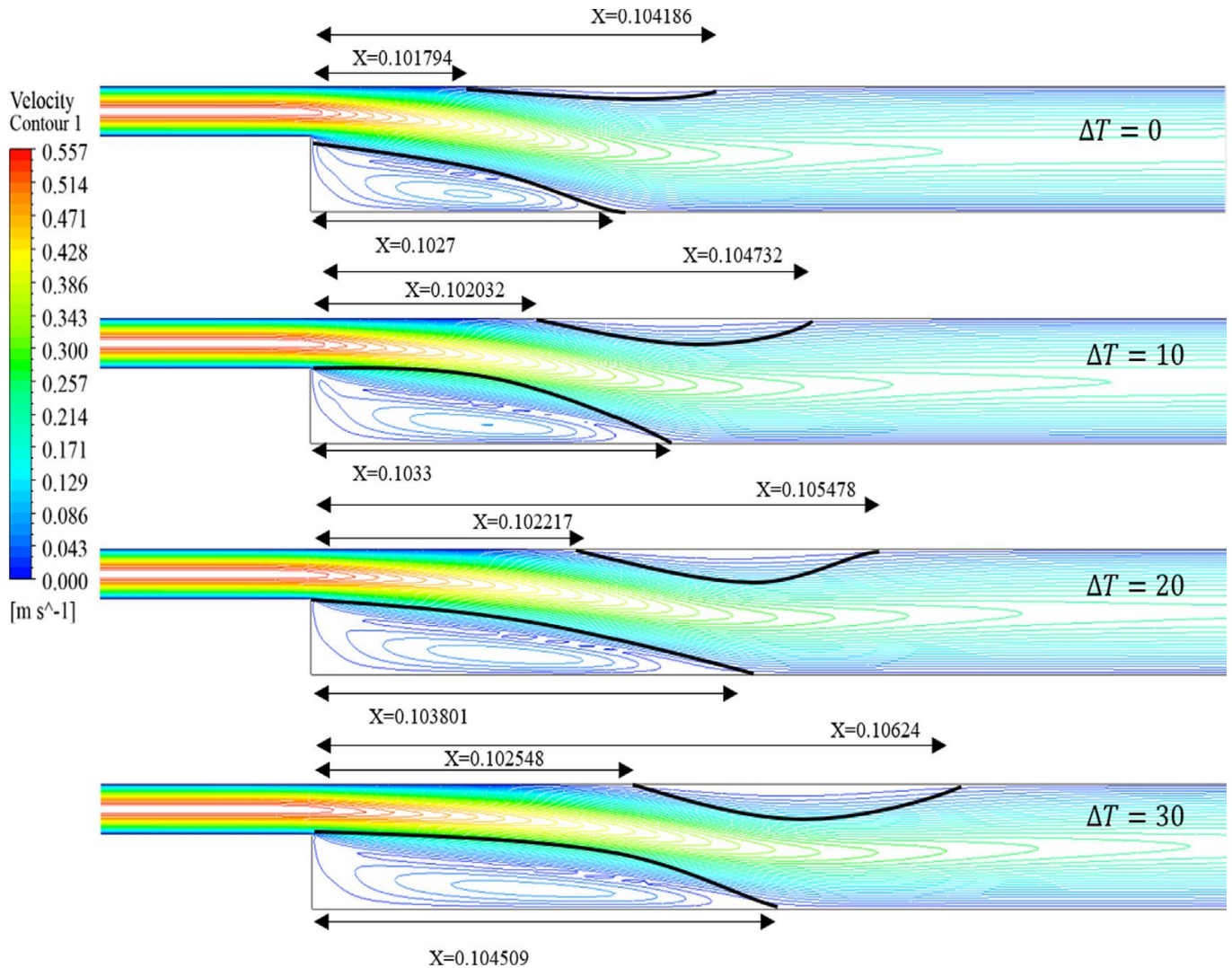
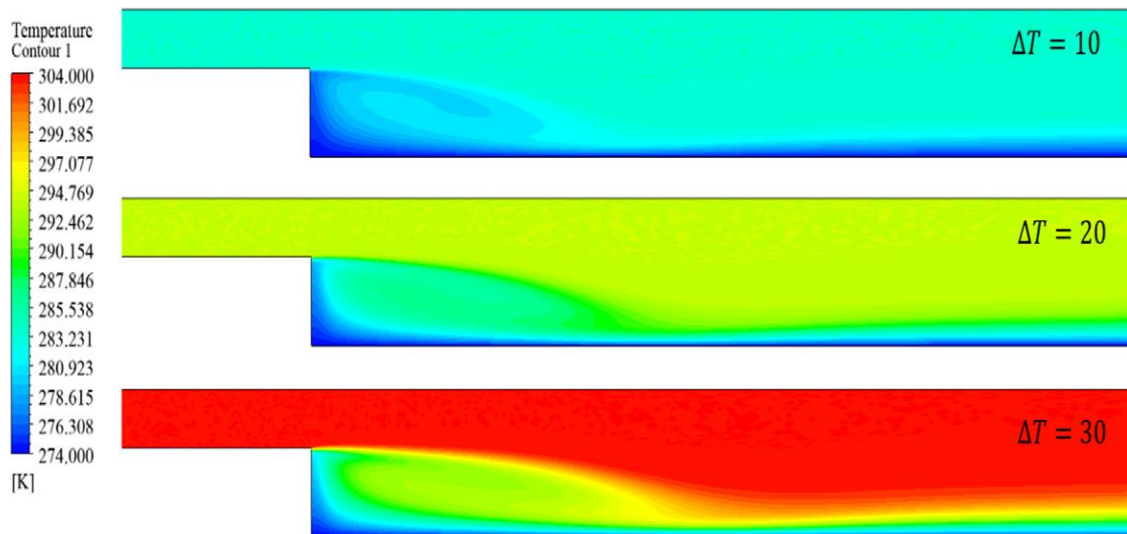
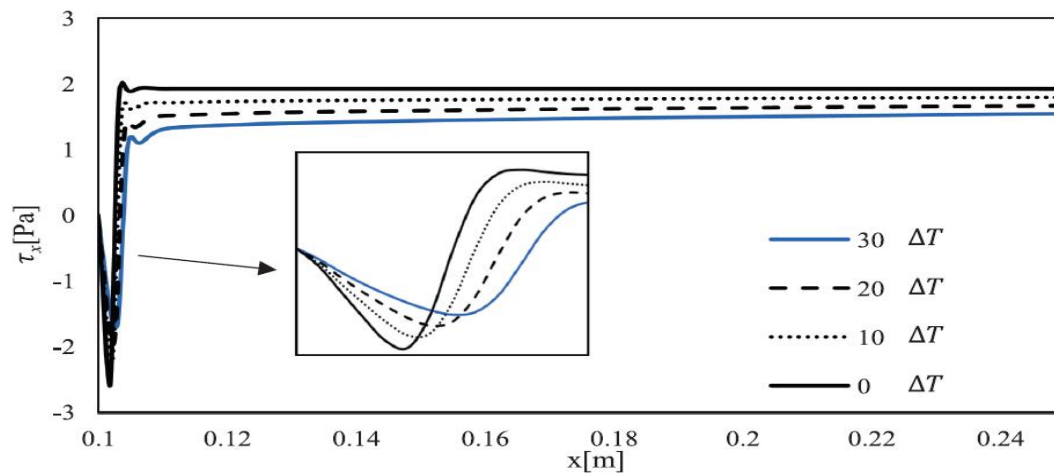
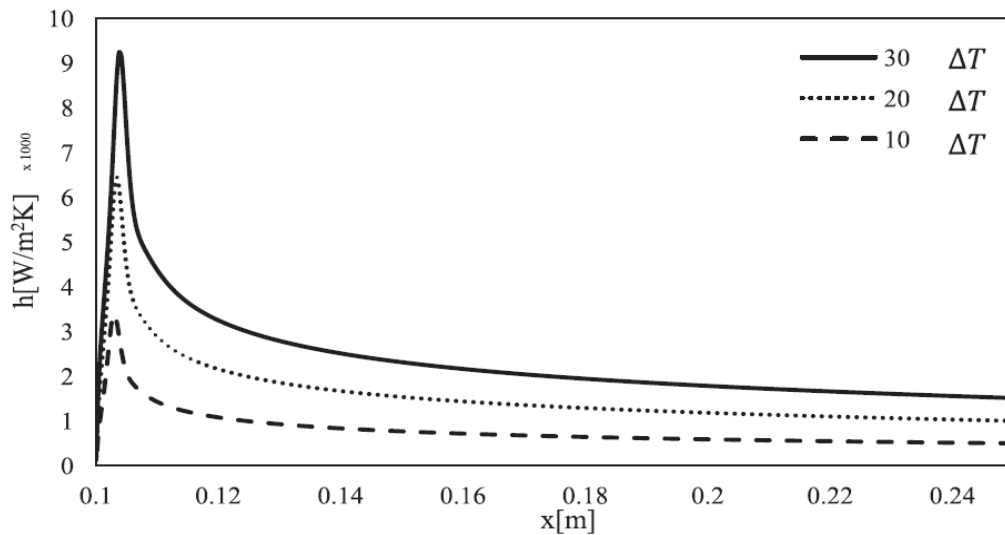


Figure 6.17 Velocity contours at different  $\Delta T=10$ , 20, and  $\Delta T=30$



Figure 6.18 Temperature contours at different values of  $\Delta T=0 \dots 30$ Figure 6.19 The wall shear stress of  $\text{Al}_2\text{O}_3$  nanofluid along the downstream wall for  $\Delta T=0 \dots 30$ Figure 6.20 The average heat transfer rate along the downstream wall for various  $\Delta T$  and  $\text{Al}_2\text{O}_3$

Bianco et al. [116] gave the normalized average heat transfer for  $\text{Al}_2\text{O}_3$ -water obtained by CFD using different methods such as two-phase (DPM) and single-phase (NSP) models with temperature-dependent (Var.) and constant (Cst.) thermo-physical properties. Table 6.4 shows the comparison of our results with those published in [116]. The present model with temperature-dependent properties reported higher transfer rate prediction in comparison with constant thermo-physical property models. For concentrations, 1 % and 4 %, the prediction of increase of heat transfer rate was higher than for NSP (Cst.) and lower for two-phase constant method DPM (Cst.) and variable properties DPM (Var.). However, the model has excellent agreement at volume fraction 4% for both constant and temperature-dependent thermophysical properties. The normalized average wall shear stress values for  $\text{Al}_2\text{O}_3$ -water along the downstream wall are presented in the Table 6.5 at volume concentrations 0, 0.01, and 0.04. The average wall shear stress has the lowest value for water and as the volume concentrations increases the wall shear stress values increases. For all volume fractions, the predictions of the wall shear stress are higher than for single phase with constant properties. Table 6.5 presents a comparison of the increase for the average wall shear rate with the volume fraction for  $\text{Al}_2\text{O}_3$ -water. Applying the present model, the prediction of the average wall shear stress values is higher for variable properties than for constant properties and the single-phase model provides lower values than the two-phase model either with constant or with temperature-dependent properties for volume fraction 1%. However, at 4 %, all models provide similar values except the DPM (Cst.), i.e., these models underestimate the average wall shear stress values.

Table 6.4.Comparison of our result on the normalized heat transfer with [116]

$\varphi$	Present work	NSP (CSt.)	NSP (Var.)	DPM (CSt.)	DPM (Var.) [116]
0	1	1	1	1	1
0.01	1.049	1.037	1.059	1.130	1.120
0.04	1.188	1.180	1.181	1.205	1.183

Table 6.5.Comparison of our result on the normalized wall shear stress with [116]

$\varphi$	Present work	NSP (CSt.)	NSP (Var.)	DPM (CSt.)	DPM (Var.) [116]
0	1	1	1	1	1
0.01	1.146	1.145	1.180	1.380	1.419
0.04	2.000	1.987	2.000	1.791	1.920



## 6.7 PERFORMANCE EFFICIENCY INDEX

The application of nanofluids and the performance of the system can be evaluated with different volume fractions for different Reynolds numbers. The evaluation of nanofluids is based on a comparison with pure water to monitor the changes in heat transfer and friction coefficient. The addition of nanoparticles has shown an improvement in enhancing the heat transfer but also increases the coefficient of friction, which can significantly affect the efficiency of the use of such fluids. The performance index is applied to analyse the efficiency of using nanoparticles in the backward-facing step channel for different volume fractions. We consider the same performance evaluation criteria as in [117]. Thus, the performance efficiency index PEI is defined with the formula

$$PEI = \frac{Nu_{nf}}{Nu_b} \left( \frac{f_{nf}}{f_b} \right)^{-\frac{1}{3}}, \quad (6.4)$$

where  $Nu_{nf}$  denotes the Nusselt number of the nanofluid,  $Nu_b$  the Nusselt number of the base-fluid (water),  $f_{nf}$  and  $f_b$  are the friction factors obtained for the nanofluid and the base fluid, respectively. Fig. 6.21 a shows the variation of the performance efficiency index in the range of the Reynolds number (280, 470). The change in PEI for different quantities of additives related to the base fluid is displayed. Since the heat transfer and pressure drop enhancement ratios determine the performance factor of nanofluids, adding nanoparticles to the base fluid increases the thermal conductivity and increases the Heat Transfer Coefficient (HTC). However, because the nanoparticles are heavier than the base fluid, the pressure drop also increases. As a result, the total effect of adding nanoparticles to the base fluid can be calculated. Fig. 6.21 b. Shows the performance factor results for different nanofluids. A performance factor of more than one is generally regarded as reasonable. The following are the key conclusions made from 9.21:

- As illustrated in Fig. 9.21, the performance factor was determined to be unsatisfactory for some of the nanofluids, independent of the comparison criterion. This could be due to the fact that nanofluids have a higher fraction of viscosity increment than HTC.
- The greatest performance factor value for  $Al_2O_3$  nanofluid at 1% volume fraction was found to be above 1 across all tested situations. The  $Al_2O_3$  nanofluid of 1 % volume fraction has lower pressure drop and due to lower viscosity rise compared to other nanofluids.

- Fig. 9.21 presents the PEI at different volume fractions for  $Re = 280$  for  $Al_2O_3$  and  $TiO_2$ . The result reported that increasing the volume fraction can lead to decreases in the PEI of the fluid.
- According to Fig. 9.21-b, the performance efficiency index for  $Al_2O_3$  and  $TiO_2$  can be approximated as a function of the volume fraction:

$$PEI(TiO_2) = 1240.7\varphi^3 - 116.31\varphi^2 + 1.6322\varphi + 1.0017 \text{ with } R^2 = 0.9957$$

$$PEI(Al_2O_3) = 1324.7\varphi^3 - 119.76\varphi^2 + 1.2082\varphi + 1.0018 \text{ with } R^2 = 0.9972$$

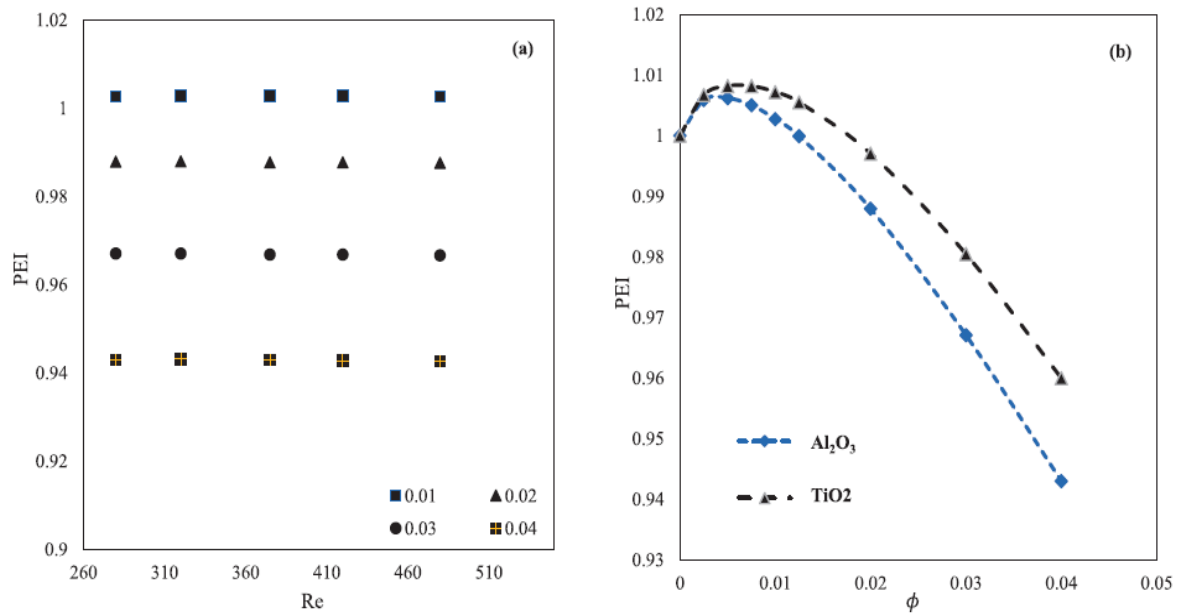


Figure 6.21. Performance efficiency index and  $\varphi = 0.01, 0.02, 0.03, 0.04$  (a) for  $Al_2O_3$  (b) for  $Al_2O_3$  and  $TiO_2$

## 7 COMPARISON OF DIFFERENT NANOFLUID MODELINGS

We investigate and compare the results obtained by different CFD nanofluid modeling techniques.

### 7.1 NEWTONIAN AND NON-NEWTONIAN SINGLE-PHASE MODELS

In this section, we analyse the enhancement of heat transfer in both Newtonian and non-Newtonian nanofluid models at different volume fractions. In this section, we present predictions of the hydrodynamic and thermal characteristics of nanofluid flow in a channel and analyze the parameters that can be affected by the addition of nanoparticles to the base fluid in the 0-4% volume fraction range, taking into account the temperature dependence of the thermophysical properties of the fluid.

A comparison with experimental results is analyzed using a single-phase model for the behavior of both Newtonian and non-Newtonian fluids in the range of 280 to 470 Reynolds numbers. Applying temperature-dependent in modeling the thermophysical properties of the nanofluids with different volume fractions 0-4% of nanoparticles are considered.

Calculated and experimental results for the friction coefficient of  $\text{Al}_2\text{O}_3$ - water nanofluid at 1% concentration  $280 < \text{Re} < 470$  are shown in Figure 7.1. When the Non-NSP method is used, the coefficient of friction is lower compared to the Newtonian single-phase method. Nevertheless, both models show acceptable accuracy when compared with experimental results [110]. The Nusselt coefficient results along the bottom wall for the application of Newtonian and non-Newtonian models are shown in Figure 7.2 when compared with experimental results. The Newtonian model prediction shows higher Nusselt number values than the non-Newtonian model.

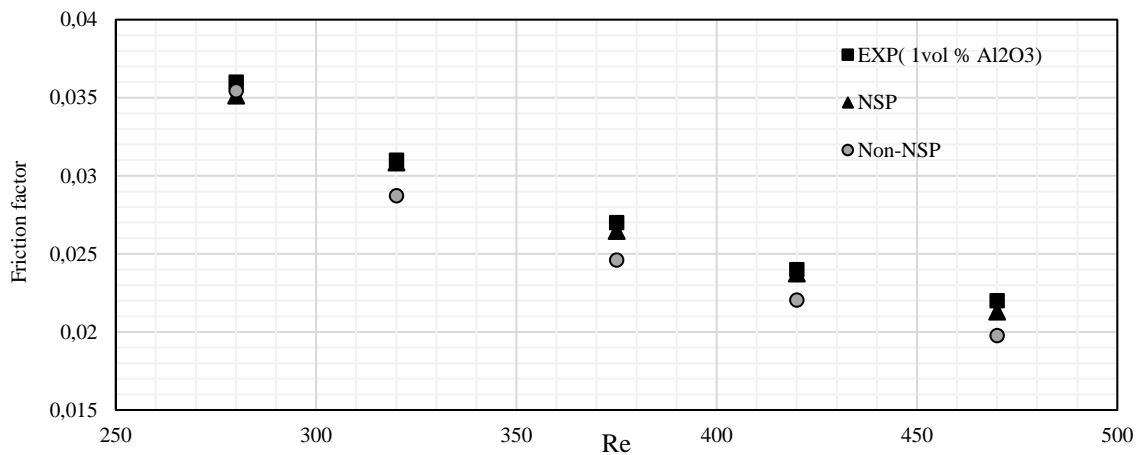


Figure 7.1. Comparison of the friction factors with experimental data for  $\text{Al}_2\text{O}_3$

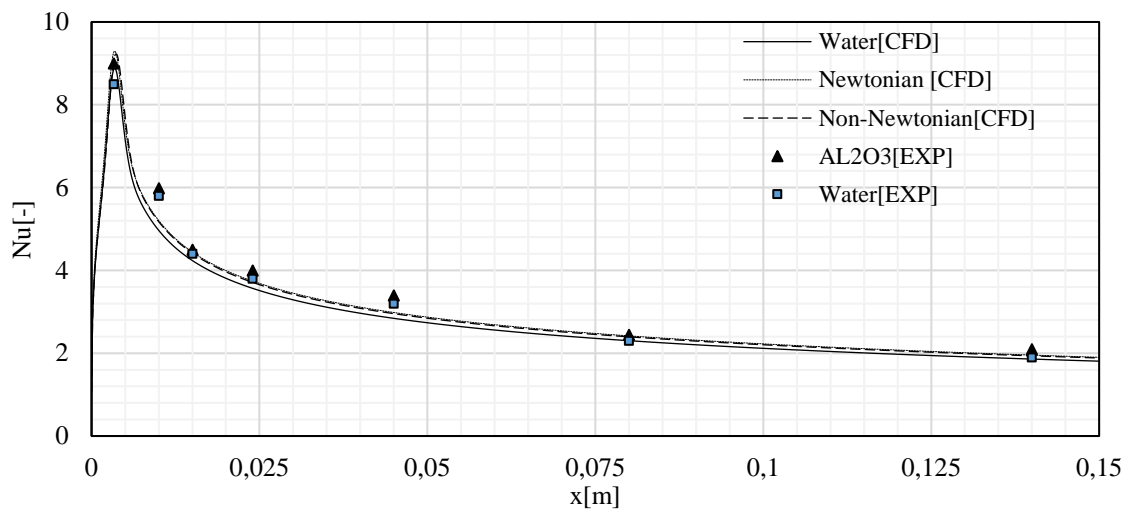


Figure 7.2. Comparison of Nu obtained by NSP, Non-NSP and experimental data for  $\text{Al}_2\text{O}_3$

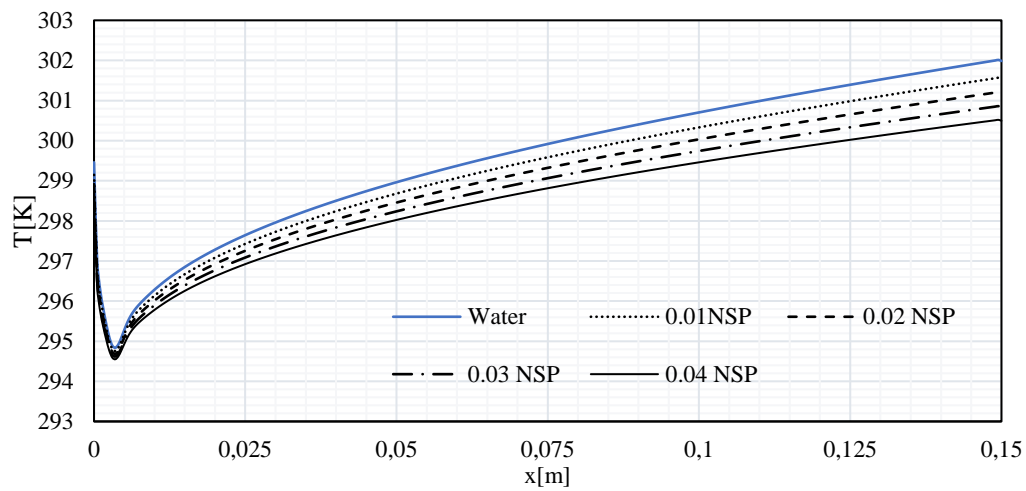


Figure 7.3. Profiles of  $T$  along the downstream wall for NSP for different concentrations and  $\text{Al}_2\text{O}_3$

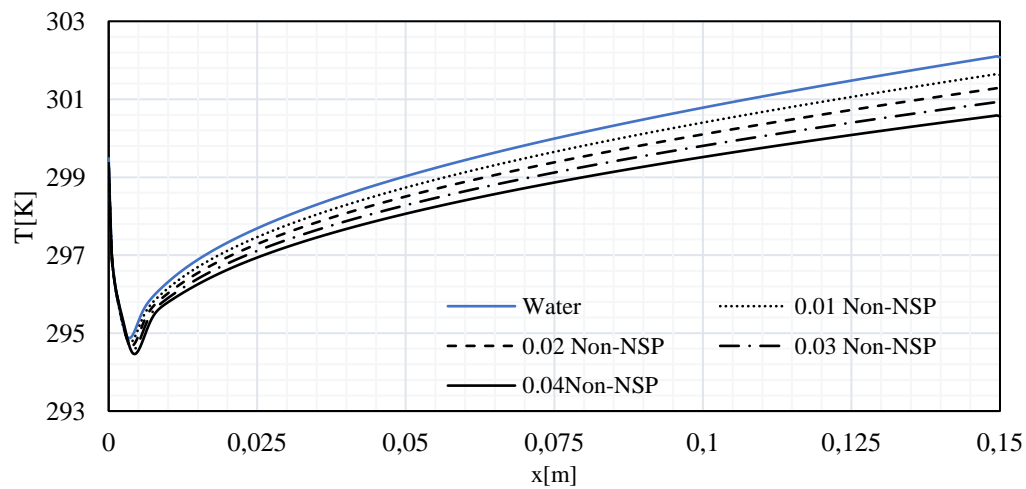


Figure 7.4. The temperature along the downstream wall obtained by Non-NSP for different concentrations and  $\text{Al}_2\text{O}_3$

In Fig. 7.3, the axial temperature variation along the downstream wall is plotted for  $Re=280$ . Using NSP, the obtained results for different volume fractions show that the temperature distribution is strongly affected by the addition of nanoparticles. The increase in concentration shows a significant decrease in temperature in the direction of flow along the wall. Furthermore, as you move further along the wall, the temperature values increase, indicating that as the volume fraction increases, greater heat transfer is achieved.

The results of the non-Newtonian model are reported on Fig.7.4 for 1-4% concentrations. The observation on the effect of adding nanoparticles was similar to the Newtonian model. Increasing the volume fraction showed a significant effect on temperature. However, the use of the Newtonian model resulted in colder temperatures than the non-Newtonian model for all fluids tested, as shown in Fig. 7.5. It can be observed that the temperature gradually decreases after the step where the recirculation zone is formed, reaching minimum values and then starts to rise again downstream of the wall. The temperatures show that the temperature of the non-Newtonian fluids is colder than that of the Newtonian fluid before the recirculation point. Apart from this, a colder temperature profile is obtained with the NSP model.

The results of the temperatures using both models showed a positive effect of increasing the nanoparticle concentration. Increasing the nanoparticle concentration leads to an improvement in the thermo-physical properties of the mixture. The heat transfer coefficients of  $Al_2O_3$ -water nanofluids for different volume fractions are presented in Fig. 7.6 for Newtonian and non-Newtonian models. The results show an extraordinary increase after the step in the recirculation zone. Then the heat transfer coefficient (HTC) decreases along the wall in the downstream direction. A comparison of the two models indicates a larger gradient of HTC along the downstream wall for the NSP than for the non-Newtonian model. However, the non-Newtonian model shows colder temperatures in the recirculation zone, resulting in higher HTC values in this zone. The average heat transfer ( $h_{av}$ ) along the downstream wall and the ratio  $h_{nf}/h_{bf}$  for both models are compared for the 0-4% range of the volume fraction at  $Re=280$  in Table 7.1.

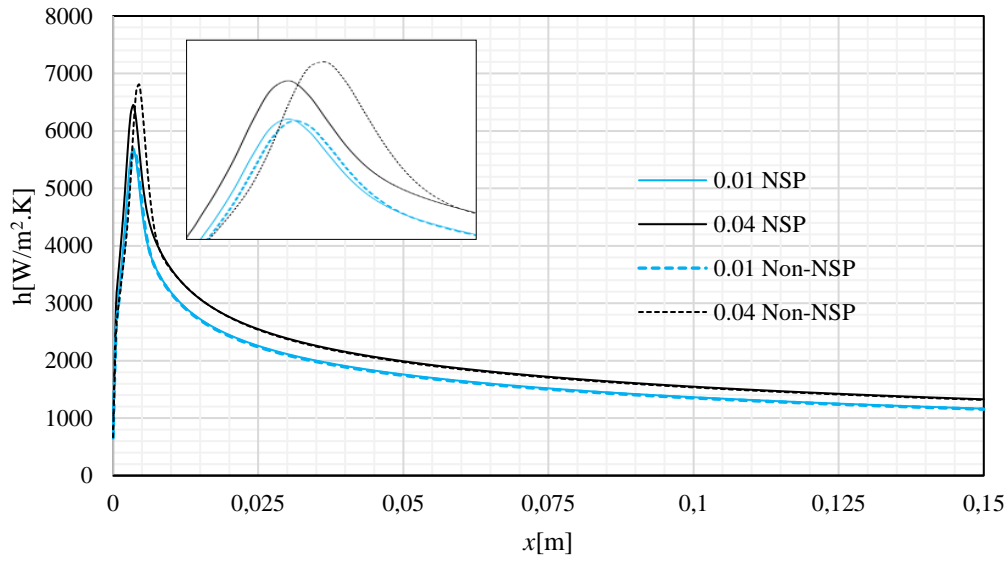


Figure 7.5. Comparison of the heat transfer rate along the downstream wall for Non-NSP and NSP for  $\text{Al}_2\text{O}_3$  and  $\varphi = 0.01$  and  $0.04$

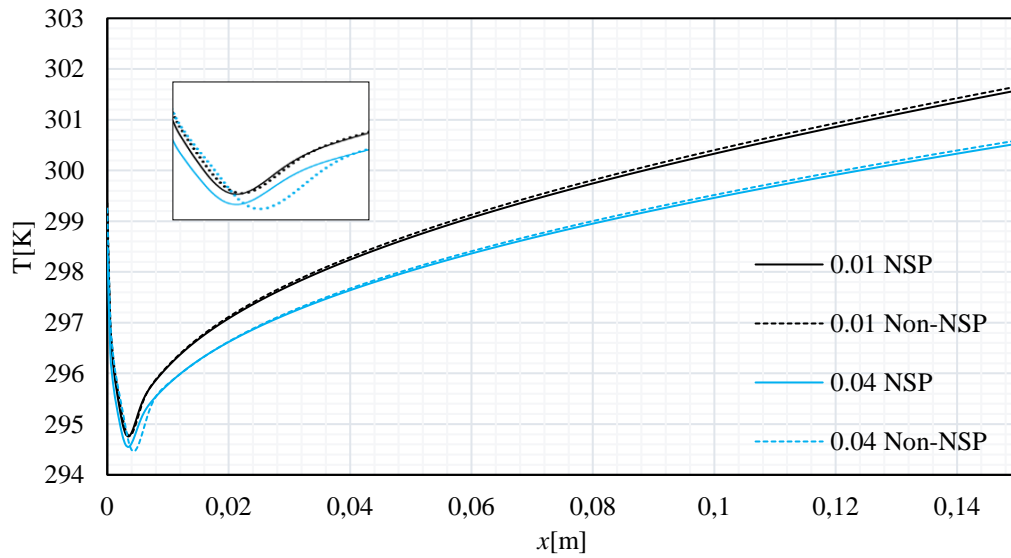


Figure 7.6. Comparison of the temperatures along the downstream wall for Non-NSP and NSP for  $\text{Al}_2\text{O}_3$  and  $\varphi = 0.01$  and  $0.04$

Since non-Newtonian fluid implies higher HTC values in the recirculation zone, the average heat transfer ( $h_{av}$ ) along the downstream wall and the  $h_{nf}/h_{bf}$  rate at  $\text{Re}=280$  in the 0-4% volume fraction interval for both models are compared in Table 7.1.

Table 7.1. Average heat transfer and the rate and  $h_{nf}/h_{bf}$  for NSP and Non-NSP

$\phi$	NSP $h_{av}$	Non-NSP $h_{av}$	NSP $h_{nf}/h_{bf}$	Non-NSP $h_{nf}/h_{bf}$
0	1703.25	1686.14	1	1
0.01	1787.87	1771.36	1.0496	1.0505
0.02	1861.95	1845.97	1.0931	1.0947
0.03	1940.64	1925.79	1.1393	1.1421
0.04	2024.16	2010.64	1.1884	1.1924

Table 7.2. The comparison of the heat transfer rates obtained by different models [116]

$\frac{h_{nf}}{h_{bf}}$ $\phi$	NSP (Var.) Present work	Non-NSP (Var.) Present work	NSP (CSt.) [116]	NSP (Var.) [116]	DPM (CSt.) [116]	DPM (Var.) [116]
0	1	1	1	1	1	1
0.01	1.049	1.050	1.037	1.059	1.130	1.120
0.04	1.188	1.192	1.180	1.181	1.205	1.183

Table 7.3. The comparison of the shear and the rate of the shear stresses obtained by NSP and Non-NSP

$\phi$	$\tau_{av}$ [Pa]		$\tau_{nf}/\tau_{bf}$	
	NSP	Non-NSP	NSP	Non-NSP
0	0.6138	0.6515	1	1
0.01	0.7036	0.6868	1.1463	1.1189
0.02	0.8313	0.7353	1.3542	1.1980
0.03	1.0033	0.7969	1.6345	1.2982
0.04	1.2276	0.8702	2.0000	1.4177

The Newtonian model shows higher  $h_{av}$  values than the non-Newtonian model for all volume fractions tested. However, the rate of increase of the heat transfer coefficient  $h_{nf}/h_{bf}$  for the base fluid is higher for non-NSP than for NSP for all concentrations. Different approaches were used to compare the growth rate of the heat transfer coefficient for  $Al_2O_3$ , such as the two-phase method (DPM) and the one-phase method using temperature-dependent (Var.) and constant (Cst.) thermophysical properties. Table 7.2 compares the results of the single-phase approaches with those of other methods [116]. For the 1 and 4 % concentrations, models with temperature-dependent properties predicted higher transfer rates than models with constant thermophysical parameters for the single-phase cases. In the two-phase

case this is the reverse. Furthermore, the rates obtained with the two-phase model are larger in both the Var. and Cst. cases.

At  $Re=280$  and a volume concentration of 0-4%, Table 7.3 shows a comparison of average wall shear stress values along the downstream wall using Newtonian and non-Newtonian models. For both Newtonian and non-Newtonian fluid behaviour, the average wall shear stress values are lowest for water, and the wall shear stress values increase with increasing volume concentration. The increase in values was larger in the Newtonian model than in the non-Newtonian model.

Table 7.4 shows a comparison of the average wall shear rate growth rates for NSP, Non-NSP and DPM models for constant and temperature dependent cases. The predictions of the average wall shear stress rate using Newtonian behavior are higher than for Non-NSP. Lower values are obtained using the constant properties. For a 1% volume fraction, the two-phase model also gives higher values for constant or dependent properties. However, all models show similar values for dependent fluid properties varying at 4%. Non-NSP underestimates  $\tau_{av}$ .

Table 7.4. Single-phase comparison wall shear stress with other methods

$\varphi$ $\frac{\tau_{nf}}{\tau_{bf}}$	NSP Present work	Non-NSP Present work	NSP (Cst.) [116]	NSP (Var.) [116]	DPM (Cst.) [116]	DPM (Var.) [116]
0	1	1	1	1	1	1
0.01	1.146	1.1189	1.145	1.180	1.380	1.419
0.04	2.000	1.4177	1.987	2.000	1.791	1.920

The single-phase method with two types of fluid behaviour - Newtonian and non-Newtonian - was considered for simulating  $Al_2O_3$  at different volume fractions. The results of the analysis are summarized below:

- The result shows a higher prediction for the HTC for the Newtonian model than for the non-Newtonian model. The validity of the models were tested with the results published in [18].
- The results obtained using these models were compared with the data in [116]. With an increase in particle loading for all tested situations, the wall shear stress was found to increase.
- For the Nusselt number estimation, both NSP and non-NSP underestimate the Nu.



## 7.2 COMPARISON OF CFD RESULTS WITH EXPERIMENTAL DATA

The numerical values  $Nu$  obtained by the five models with the experimental data for  $Re=280$  are compared for temperature dependent fluid properties. In comparison to pure water, all single-phase models predict considerable increase in  $Nu$  number with addition of nanoparticles

### 7.2.1 RESULTS USING TEMPERATURE DEPENDENT THERMO-PHYSICAL PROPERTIES

The Nusselt number is calculated using temperature-dependent fluid properties at different positions  $X_1, X_2, \dots, X_7$  (see Fig. 6.2). The differences with respect to the experimental data are determined using the results of [110]. Comparing NSP and Non-NSP models with the experimental study, both models underestimate the Nusselt number, and the error decreases as the distance from the step increases. The underestimation of  $Nu$  is due to the neglect of slip mechanisms between ultrafine nanoparticles and the base fluid in the single-phase modelling. The error for non-Newtonian fluid is higher than for Newtonian fluid, the average errors are -10.77% and -10.21%, respectively (see Table 7.5). It can be seen that the single-phase model gives significantly lower estimates than the experimental data for  $\phi = 0.01$ .

Predictions of the local Nusselt number using two-phase models are shown in Figure 7.7. Mixture and VOF overestimate the Nusselt number. Of all the two-phase models, the Eulerian model gives the highest prediction accuracy for the  $Nu$  number along the channel.

For each of the two-phase models, we obtained smaller errors than for the single-phase Newtonian or non-Newtonian models in the recirculation zone. The average error for the two-phase models in estimating  $Nu$  using the Mixture models was 13.506% and the error for VOF was 12.571%. The values closest to the experimental values were obtained for the Eulerian model with an average error of -1.0420 %.

Table 7.5. Nusselt number error obtained for temperature-dependent properties at distances  $X_i$  ( $i=1 \dots 7$ ) for comparison with the experimental results of [110] in %

<b>Models position</b>	<b>NSP</b>	<b>Non-NSP</b>	<b>Eulerian</b>	<b>VOF</b>	<b>Mixture</b>
$X_1$	-18.884	-18.388	-12.969	+5.965	+6.036
$X_2$	-15.847	-16.219	+8.310	+9.695	+10.878
$X_3$	-1.8147	-2.518	-6.718	+22.307	+22.552
$X_4$	-9.136	-9.918	0.610	+14.830	+15.625
$X_5$	-12.171	-13.003	+2.339	+10.669	+11.518
$X_6$	-4.064	-4.9982	-8.283	+16.651	+17.824
$X_7$	-9.574	-10.408	-1.932	+7.8855	+10.106
Ave-Error	-10.213	-10.779	1.0420	+12.571	+13.506

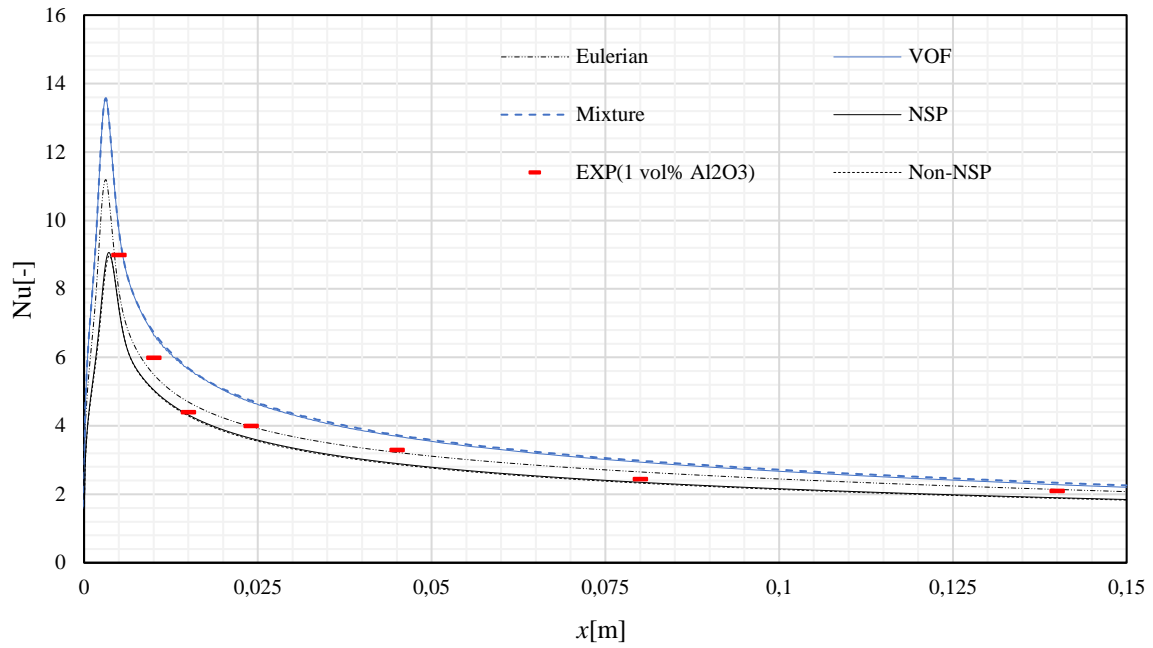


Figure 7.7. Comparison Nu for temperature-dependent fluid properties with experimental data [110]

Table 7.6. Nusselt number error in % for constant fluid properties

<b>Models position</b>	<b>NSP</b>	<b>Non-NSP</b>	<b>Eulerian</b>	<b>Mixture</b>	<b>VOF</b>
X <sub>1</sub>	-20.759	-22.0992	-15.6696	+2.7785	+2.7648
X <sub>2</sub>	-18.487	-18.5893	+10.6395	+7.32334	+7.3985
X <sub>3</sub>	-5.265	-5.3665	-3.9881	+19.9723	+20.0297
X <sub>4</sub>	-12.583	-12.6308	3.19662	+12.3466	+12.4741
X <sub>5</sub>	-15.796	-15.8216	4.95797	+7.93882	+7.8766
X <sub>6</sub>	-8.351	-8.3703	-5.2707	+13.7369	+13.6509
X <sub>7</sub>	-14.012	-14.0243	-1.04989	+4.78896	+4.7507
Ave-Error	-13.608	-13.843	-3.7506	+9.8408	+9.8493

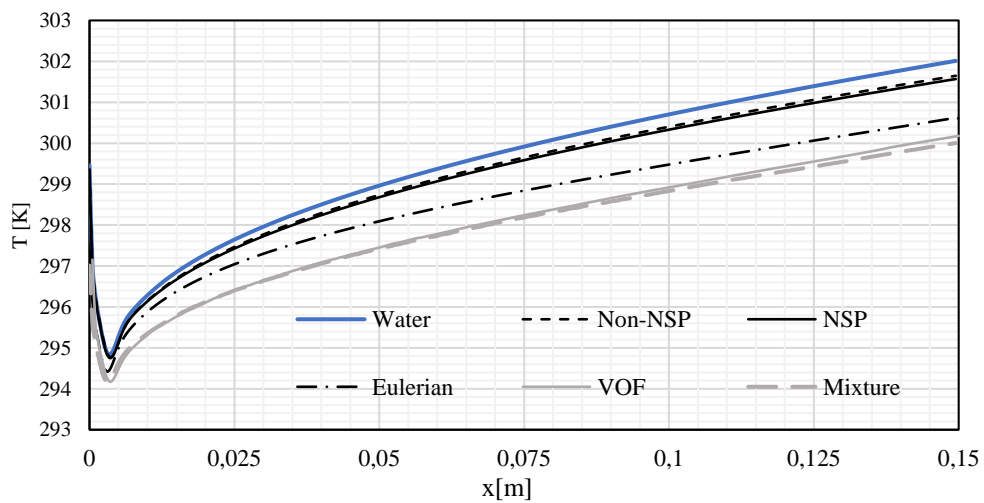


Figure 7.8. Temperature profiles along the downstream wall for different models

Table 7.5 shows the % difference in Nu amounts compared to the experimental results. For all models, the Eulerian two-phase model gives the values closest to the experimental data, and is the most accurate. The evolution of the temperature at the downstream wall predicted by the different models is shown in Fig. 7.8. The single-phase predictions are higher than the two-phase predictions, but the Mixture and VOF two-phase models are nearly identical. The Eulerian model gives higher temperature estimates than the other two-phase models and lower than both single-phase models.

## 7.2.2 RESULTS USING CONSTANT THERMO-PHYSICAL PROPERTIES

In this section, constant fluid properties are used in CFD simulations. The values of the Nusselt number using the constant (Cst) fluid properties, which are not temperature dependent in the five models, are compared in Fig. 7.9. The single-phase models report an increase in Nu number with the application of nanoparticles. For the NSP and Non-NSP models, the Nusselt number is smaller than the experimental ad. The error increases to -13.843% for non-Newtonian and -13.608% for Newtonian (see Table 7.6).

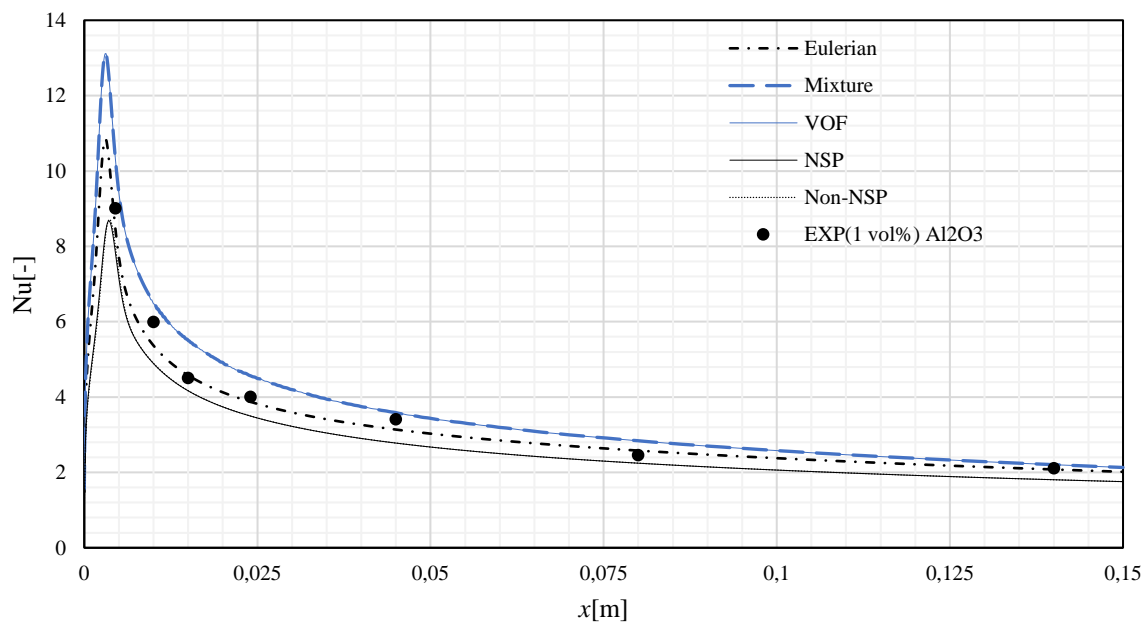


Figure 7.9. Comparison of Nu obtained with CFD using constant properties with experimental data [110]

Figure 7.10 shows the temperature profiles of the tested models for constant fluid properties. The temperature is highly dependent on the value of  $\phi$ . The fluid temperature decreases rapidly with increasing concentration, especially near the downstream wall; in addition, the difference between the base fluid and nanofluid temperatures increases with increasing  $x$ , suggesting that a higher heat transfer rate is achieved for the nanofluid. The two-phase model results in lower temperatures than the single-phase model. Furthermore, the temperature difference between the

base fluid and the nanofluid is smaller for the single-phase model. For the Eulerian model, the lack of temperature dependent properties affects the accuracy and the average error increases to -3.7506%.

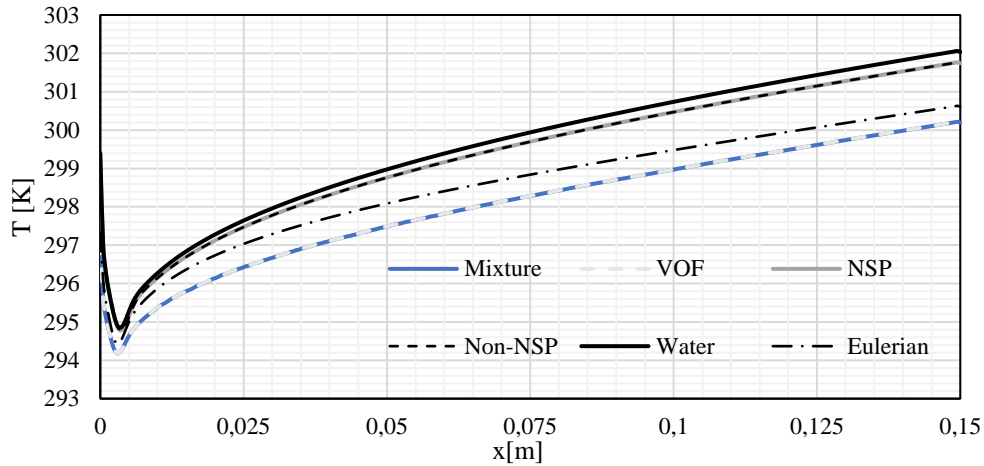


Figure 7.10 Profiles of the temperature along downstream wall for constant fluid properties and  $\varphi = 0.01$

A comparison of the constant (Cst.) and temperature dependent (Var.) properties for the temperature profiles is shown in Fig. 7.11. The temperature profiles are higher for the constant fluid properties than for the temperature dependent properties. It is observed that the difference increases with  $x$ . This is because the thermal conductivity increases linearly with temperature and the density, viscosity and heat capacity decrease with increasing temperature.

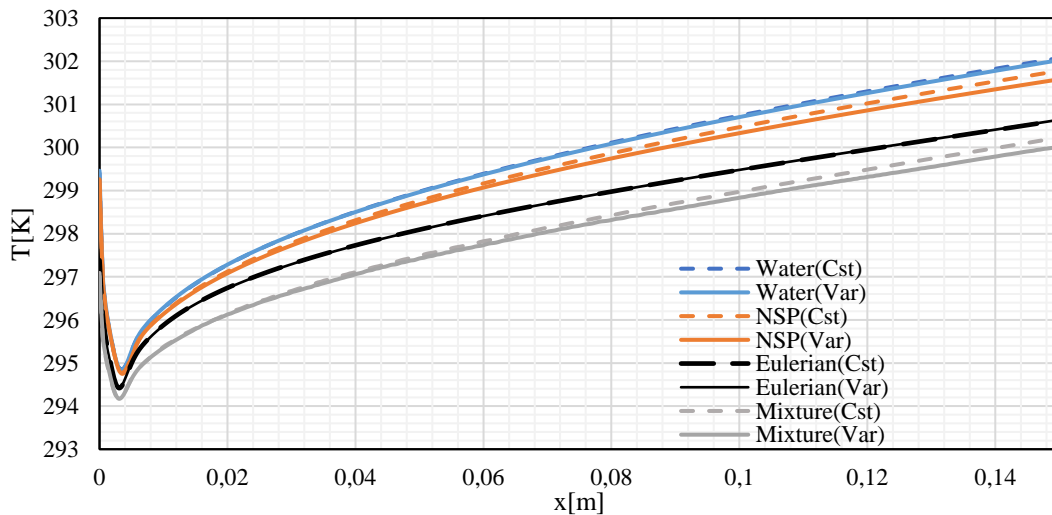


Figure 7.11 Comparison of the temperature along the downstream wall for temperature-dependent and constant properties and  $\varphi = 0.01$

Temperature-based models can be said to provide higher heat transfer coefficients and Nusselt numbers. A comparison of temperature profiles for temperature-dependent and constant fluid properties reported that this was lower for the temperature-dependent properties than for constant properties. On the other hand, this higher Nusselt number prediction increased the accuracy of the

single-phase models. The accuracy increased to 3.395% for NSP and 3.07% for Non-NSP. The Eulerian model using temperature-dependent formulas is significantly more accurate with an average error of 1.0420%. However, the use of the temperature-dependent formula overestimated the Nusselt number, with an increase in average error of more than 10%.

Figures 7.12 and 7.13 display the velocity and temperature profiles for the five models using temperature-dependent properties for  $\text{Al}_2\text{O}_3$ -water of 1% volume fraction at the outlet. It can be observed that all the five models' prediction of the velocity are quite similar. However, the output temperature profiles differ significantly. The analysis in Fig. 7.12 shows that when the model used predicts a higher temperature, it results in a higher velocity. As can be seen, at the downstream wall ( $x=0$ ), the temperatures predicted by the Non-NSP and NSP are higher than for all two-phase models, which result in lower velocities. This may be due to a decrease in viscosity with increasing temperature.

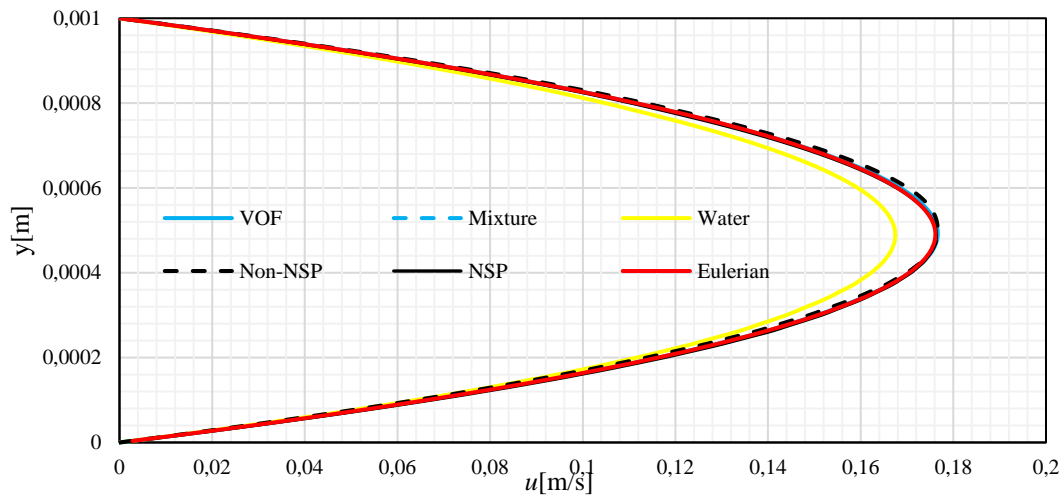


Figure 7.12 Different velocity profiles at the outlet

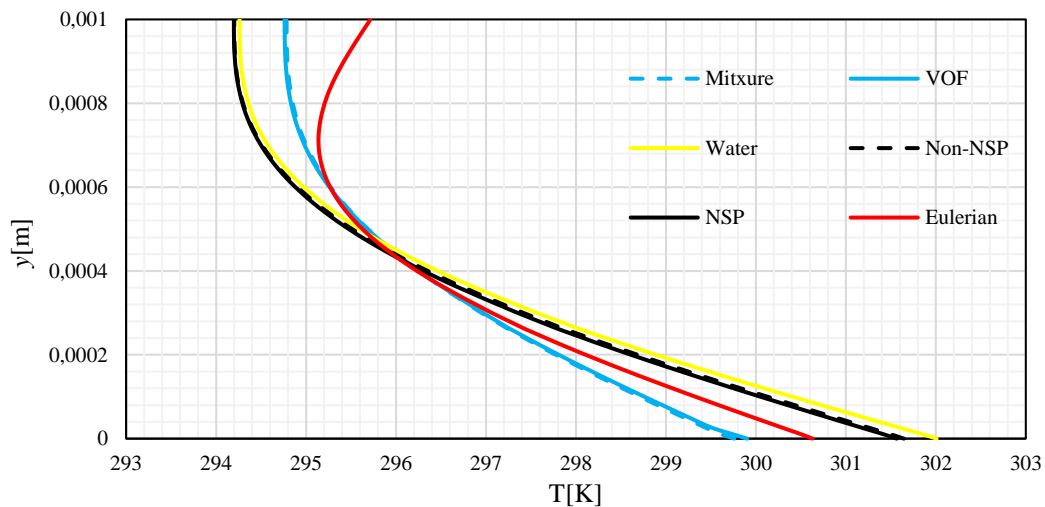


Figure. 7.13 Different temperature profiles at the outlet

## 8 A NEW VISCOSITY EQUATION FOR NANOFLUIDS

In this section, we propose an empirical relationship for the effective viscosity of nanofluid. The new equation for the effective dynamic viscosity of nanofluid, which is normalized to the dynamic viscosity of the base fluid, is developed from a large number of experimental data from the literature.

### 8.1 METHODOLOGY

The effective viscosity of the nanofluid is determined with the viscosity of the base fluid, the volume fraction of the nanoparticle, the temperature of the nanoparticle, and the density of the nanoparticles. The new formula is compared with experimental data on nanofluid viscosities in the literature. Various types of nanoparticles such as  $\text{Al}_2\text{O}_3$ ,  $\text{CuO}$ ,  $\text{Fe}$ ,  $\text{Fe}_3\text{O}_4$ ,  $\text{SiC}$ ,  $\text{ZnO}$ ,  $\text{AlN}$  (Aluminium Nitride),  $\text{TiO}_2$ , SWCNT (Single-Wall Carbon Nanotube),  $\text{Zr}$ ,  $\text{Ag}$ ,  $\text{SiO}_2$ , CNT (Carbon Nanotube),  $\text{Cu}$ , hBN (hexagonal Boron Nitride), MWCNT (Multi-Wall Carbon Nanotube), DWCNT (Double-Wall Carbon Nanotube),  $\text{Zr}$ , graphite,  $\text{CaCO}_3$ , and the size of nanoparticles varies between 2 nm and 300 nm in diameter and is suspended in various base fluids, like water, propylene glycol, kerosene, etc. An experimental database of the applied nanofluids is shown in Table 8.1.

For the description of the new correlation, we introduce the effective viscosity with two parts:

$$\mu_{eff} = \mu_{static} + \mu_{Brownian}, \quad (8.1)$$

where the static viscosity consists of the viscosity values of mixtures  $\mu_{m\,nf}$  and the viscosity  $\mu_{NL}$  due to the nanolayer

$$\mu_{static} = \mu_{m\,nf} + \mu_{NL\,nf}. \quad (8.2)$$

Viscosity values of the mixtures can be calculated as

$$\mu_{m\,nf} = \mu_{bf}(1 + \mu\varphi), \quad (8.3)$$

with  $\mu = 2.5$  (see the Einstein's formula). The viscosity effect due to nanolayer is counted in the form

$$\mu_{NL} = \mu_{bf}(\mu\varphi_e - \mu\varphi). \quad (8.4)$$

Therefore, one gets from (8.3)-(8.4) that the static viscosity is

$$\mu_{static} = \mu_{bf}(1 + \mu\varphi) + \mu_{bf}(\mu\varphi_e - \mu\varphi), \quad (8.5)$$

i.e, the static viscosity has the form

$$\mu_{static} = \mu_{bf}(1 + \mu\varphi_e) \quad (8.6)$$

and for  $\mu$  we assume a second order approximation with  $\varphi_e$

$$\mu = A_1 + A_2\varphi_e + A_3\varphi_e^2, \quad (8.7)$$

then

$$\mu_{static} = \mu_{bf}(1 + A_1\varphi_e + A_2\varphi_e^2 + A_3\varphi_e^3). \quad (8.8)$$

The values of  $A_1$ ,  $A_2$  and  $A_3$  in (8.7) are determined using regression analysis based on 21 viscosity models depending on  $\varphi$ , listed in Table 8.1, all together 4,000 data in the volume fraction range 0...0.2 is considered. Therefore, the static viscosity has the form

$$\mu_{static} = \mu_{bf}(1 + 9.4974 \varphi_e + 77.811 \varphi_e^2 + 0.9514 \varphi_e^3). \quad (8.9)$$

In Fig. 8.1, the static viscosity calculated is compared with several viscosity models. It is observed that the gap in predictions of the effective viscosity depending on the volume fraction is big. As you can see, the ratio can vary from 1 to more than 10. The result of the proposed static viscosity shows that it is possible to overcome the shortcomings in the modelling of nanofluid viscosity. The equation is written in power form (see equation (8.9)).

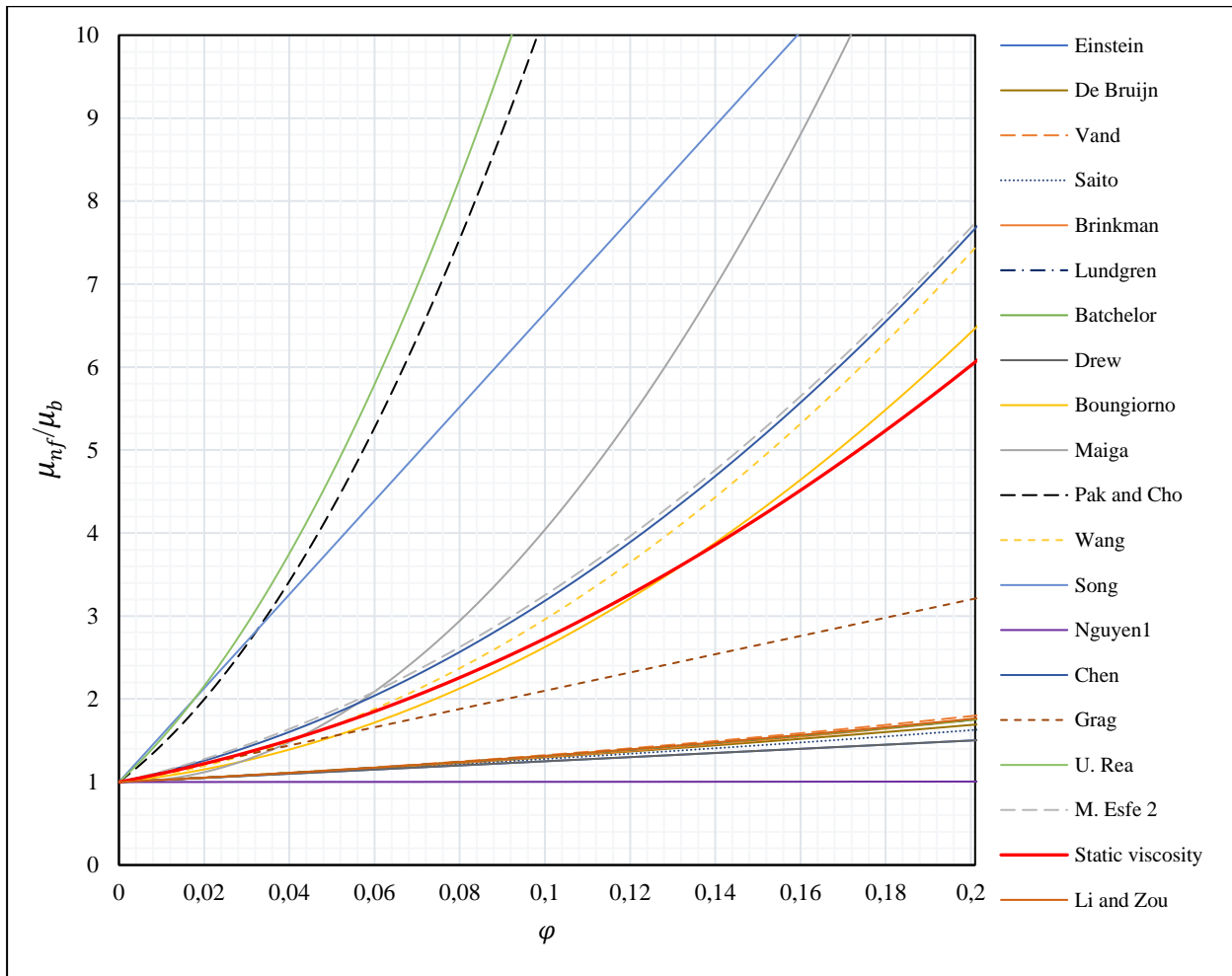


**Figure 8. 1.** The normalized static viscosity versus volume fraction  $\varphi$

In the new viscosity model, a  $\mu_{Brownian}$  term is added to the static viscosity due to the Brownian motion of the nanoparticles [39]:

$$\mu_{Brownian} = \frac{\rho_p V_B d_p^2}{72C\delta}. \quad (8.10)$$

Table 8.1 presents a list of papers on experimental viscosity results depending on the nanoparticles' volume fraction  $\varphi$ , the diameter in a temperature range, and the number of measurement data. By analysing the experimental data from Table 8.1, the correlation factor  $C$  in (8.11) is assumed as a function of  $\varphi$  and  $T$ . By evaluating the experimental results for the calculation of the correction factor  $C$ , and the following formula is suggested

$$C(T, \varphi) = c_1 + c_2, \quad (8.11)$$

with

$$c_1 = D_1 T^{-B_1}, \text{ and } c_2 = D_2 \varphi^{-B_2}, \quad (8.12)$$

where  $B_1$ ,  $B_2$  and  $D_1$ ,  $D_2$  are constants calculated from experimental data.

Applying (8.9) and (8.10), the final form of our proposed model is as follows:

$$\frac{\mu_{nf}}{\mu_{bf}} = 1 + 9.4974 \varphi_e + 77.811 \varphi_e^2 + 0.9514 \varphi_e^3 + \frac{\sqrt{\frac{18K_b T \rho_p}{\pi}}}{39.6231^3 \sqrt{\frac{\pi}{\varphi}} c \sqrt{d_p}}. \quad (8.13)$$

**Table 8.1.** Database of experimental results

Author	Base fluid	Nanoparticle types	Diameter	Volume fraction	Temperature rang	Data point
Turgut et al. [118]	Water	Al <sub>2</sub> O <sub>3</sub>	35 nm	0.5-1.5%	293-323K	14
Prasher et al. [51]	PG	Al <sub>2</sub> O <sub>3</sub>	27, 40, 50 nm	0-3%	303-333K	37
Nguyen et al. [41]	Water	Al <sub>2</sub> O <sub>3</sub>	36,47nm	1-12%	295-348K	40
Jarahnejed et al. [119]	Water	Al <sub>2</sub> O <sub>3</sub>	200, 250, 300 nm	1-4%	293-333K	20
Pastoriza-Gallego et al. [120]	EG	Al <sub>2</sub> O <sub>3</sub>	43 nm	0-0.66%	283.15-323.15K	64
Pastoriza-Gallego et al. [120]	EG	Al <sub>2</sub> O <sub>3</sub>	8 nm	0-0.31%	283.15-323.15K	48
Sundar et al. [121]	EG-water 20:80%	Al <sub>2</sub> O <sub>3</sub>	36 nm	0-1.5%	273-333K	24
Sundar et al. [121]	EG-water 40:60%	Al <sub>2</sub> O <sub>3</sub>	36 nm	0-1.5%	273-333K	24
Sundar et al. [121]	EG-water 60:40%	Al <sub>2</sub> O <sub>3</sub>	36 nm	0-1.5%	273-333K	24
Mena et al. [122]	Water	Al <sub>2</sub> O <sub>3</sub>	20-30 nm	0-4%	283-298K	18
Chevalier et al. [57]	Water	SiO <sub>2</sub>	35, 94, 190 nm	1.4%-7%	328K	19
Akbari et al. [76]	EG	SiO <sub>2</sub>	20–30 nm	0.1–3.0%	303-323K	39
Garg et al. [47]	EG	Cu	200 nm	0-2%	298K	27
Esfe et al. [45]	Water	MgO	40nm	0-1%	293K	8



Khodadadi et al. [123]	Water	MgO	20 nm	0-1.2%	298-333K	40
Xiaoke Li et al. [50]	Water-EG 60:40	SiC	30 nm	0-1%	283-308.15K	30
Lee et al. [124]	DIW	SiC	100<nm	0-2%	303-343K	45
Dalkilic et al. [125]	Water	Graphite	6-10 nm	0-2%	293-333K	25
Duangthongsuk, Wongwises [42]	Water	TiO <sub>2</sub>	21nm	0-2%	288-308K	15
Turgut et al. [126]	DIW	TiO <sub>2</sub>	21 nm	0-3%	286-328K	45
Ilhan et al. [127]	Water	hBN	70 nm	0-3%	298K	4
Ilhan et al. [127]	EG50/50	hBN	70 nm	0-3%	298K	4
Ilhan et al. [127]	EG	hBN	70 nm	0-3%	298K	4
Toghraie et al. [44]	Water	Fe <sub>3</sub> O <sub>4</sub>	20-30nm	0-3%	293-308K	18
Singh et al. [49]	Toluene	Fe <sub>3</sub> O <sub>4</sub>	10 nm	0-0.5%	298-338K	20
M. Nabeel et al [52]	Coconut oil	CuO	40nm	*wt(%)0.5,2.5	308K-328K	15
Pastoriza-Gallego et al. [58]	Water	CuO	D=33±13	*wt (%)1-10	283.15K- 323.15K	56
Pastoriza-Gallego et al. [58]	Water	CuO	D=11±3 nm	*wt(%)1- 10	283.15-323.15K	48
M. Nabeel et al [128]	Coconut oil	ZnO	26 nm.	*wt(%)0.-2.5	308,318,328K	35
Pastoriza-Gallego et al. [129]	EG	ZnO	100 nm	0-2.1%	283-328K	25
Lee et al. [46]	EG	ZnO	100 nm	0-5%	293-353K	30
Yu et al. [56]	EG	ZnO	210 nm,	0.002–0.05	283K–333K	25
Zyła and Fal [130]	EG	AlN	43 nm	0-0.02	293.6K	4
Godson at al. [131]	Water	Ag	60 nm	0.3–0.9%	323-363K	68
Esfe. et. al. [48]	EG	Fe	40 nm	0-1%	299-328K	16
Esfe. et. al. [48]	EG	Fe	70nm	0-1%	299-328K	16
Esfe. et. al. [48]	EG	Fe	100nm	0-1%	299-328K	16
Esfe. et. al. [80]	Water	Fe	37 nm	0-1%	298K	6
Esfe. et. al.[80]	Water	Fe	71 nm	0-1%	298K	6
Esfe. et. al.[80]	Water	Fe	98 nm	0-1%	298K	6
Ding et al. [132]	Water	CNT	100nm <	0-0.5%	293-303K	4
Halelfadl et al. [54]	Water	CNT	9.2 nm	0-6%	273-313K	35
Esfe. et. al. [43]	Water	MWCNT	5–10 nm	0.05-1%	298-328K	24
Esfe. et. al. [91]	Water	DWCNT	2-4 nm	0-0.04%	300-340K	5
Baratpour et al. [133]	EG	SWCNT	2-5 nm	0-0.1%	303-333K	28
Rea et al. [90]	Water	Zr	10 nm	0-3%	293-353K	50
Zhu et al. [134]	Water	CaCO <sub>3</sub>	20-50 nm	0-4.11%	293K	5

The constants in the correction factor  $C$  are determined on the base of experiments and are given for different groups of nanoparticles in Table 8.2. It can be seen that although  $D_1$ ,  $D_2$  values are the same for the listed materials,  $B_1$  and  $B_2$  values are different. However, the same values of  $B_1$ ,  $B_2$  are applicable to a very large group of materials ( $\text{Al}_2\text{O}_3$ ,  $\text{CuO}$ ,  $\text{Fe}$ ,  $\text{Fe}_3\text{O}_4$ ,  $\text{SiC}$ ,  $\text{ZnO}$ ,  $\text{AlN}$ ,  $\text{TiO}_2$ ,  $\text{SWCNT}$ ,  $\text{Ag}$ ,  $\text{SiO}_2$ ,  $\text{MWCNT}$ ,  $\text{DWCNT}$ ,  $\text{SWCNT}$ ,  $\text{CaCO}_3$ ,  $\text{hBN}$ , and  $\text{MgO}$  (40nm)). Note that  $D_1$ ,  $D_2$ ,  $B_1$ , and  $B_2$  are not dependent on the type of base fluid.

Table 8.2. Correction factor values for different nanoparticle types

Nanoparticle types	$B_1$	$B_2$	Correction factor parameters ( $c_1=D_1T^{-B_1}$ , $c_2=D_2\varphi^{-B_2}$ )
$\text{Al}_2\text{O}_3$ , $\text{CuO}$ , $\text{Fe}$ , $\text{Fe}_3\text{O}_4$ , $\text{SiC}$ , $\text{ZnO}$ , $\text{AlN}$ , $\text{TiO}_2$ , $\text{SWCNT}$ , $\text{Ag}$ , $\text{SiO}_2$ , $\text{MWCNT}$ , $\text{DWCNT}$ , $\text{SWCNT}$ , $\text{CaCO}_3$ , $\text{hBN}$ , and $\text{MgO}$ (40nm)	3.95	0.64	$D_1=2 \times 10^{-16}$ $D_2=3 \times 10^{-8}$
Zr, $\text{MgO}$ (20nm)	2	0.64	
CNT, graphite, Cu	3.95	69	

The expected results of the current method (PM) were compared with more than 1150 experimental data and found a high degree of agreement. Below we show how much more accurate this approximation is compared to the equations in the literature.

## 8.2 RESULTS AND DISCUSSION

It is evident that the viscosity of nanofluid is influenced by many factors, including volume concentration, temperature, and nanolayer thickness, as well as geometrical parameters of particles (size and shape), aspect ratio, and interparticle spacing. The effects of nanofluids on the viscosity of nanofluids have been studied in terms of electromagnetic fields, electro-viscosity, dispersion energy and settling time, and the effects of base fluid parameters such as density and polarity. Our research focuses on the six most significant properties: particle size, volume concentration, base fluid, particle density, base fluid viscosity, and temperature.

The comparison of the experimental results and the prediction of different theoretical models show an underestimation of the viscosity. Figures 8.2-8.20 provide examples of the discrepancy between experimental results and existing theoretical models. The effect of the type of the nanoparticle and base fluid is investigated. Differences between the relevant experimental data and the present model (8.13) are identified.

A large number of studies show that there is no viscosity model that can predict the effect of a wide range of nanoparticle types on the viscosity of nanofluids. Comparison of different nanoparticle types and different base fluids shows that the viscosity of a nanofluid is affected by the density of the nanoparticles. It is found that the viscosity of the nanofluid increases as the density of the nanoparticles increases. In (8.13), the presence of nanoparticle density appears only in the Brownian viscosity, which is proportional to  $\sqrt{\rho_p}$ .

Firstly, the proposed model for different nanoparticle types is analysed and the viscosity values are compared with the experimental data in Table 8.1 for the corresponding volume fraction to investigate the suitability of the model for each nanoparticle type. Secondly, we investigate the effect of the base fluid on the effective viscosity as follows:

$$\mu_{nf} = (\mu_{static} + \mu_{Brownian}) \mu_{bf}.$$

Hence, the viscosity of the base fluid directly affects the effective viscosity. Thus, as the viscosity of the base fluid increases, so does the effective viscosity of the nanofluid.

### 8.2.1 WATER-BASED NANOFLUIDS

The experimental results [54] for the steady-state viscosity of CNT in water with an average diameter of 9.2 nm, for 0.0055% and 0.55% of the particle fraction, reported that the fluids were Newtonian at low particle concentrations. A comparison of the present method (PM) given by equation (8.13) and other viscosity models with the experimental results is shown in Fig. 8.2 at a temperature of 293.15 K and a particle size of 9.2 nm. The maximum error is less than 1%.

Experimental determinations of the viscosity for Fe<sub>3</sub>O<sub>4</sub>-water [44] measured in the temperature range of 293K to 328K for different volume fractions of 0.1%, 0.2%, 0.4%, 1%, 2%, and 3% showed that the viscosity significantly decreased with increasing temperature. In addition, the viscosity increases significantly with increasing solid's volume fraction. Using the experimental data, the calculated viscosity ratios showed that the maximum viscosity increase was 129.7% at 3.0% volume fraction and a temperature of 328 K. Comparison of the experimental results with the proposed models showed that the current model has excellent accuracy with an error of up to 2% (see Figure 8.3).

Turgut et al. [126] investigated the viscosity of TiO<sub>2</sub> nanoparticles in deionized water up to 3% concentration. Nanofluids were prepared by dispersing TiO<sub>2</sub> nanoparticles in water using ultrasonic devices. The nanoparticles had an average diameter of about 21 nm, and viscosity was measured at 286, 296, 313, 328 K. The experimental results reported an increase in the viscosity of the nanofluid with an increase in particle volume fraction and stated that the increase in viscosity was much larger than predicted from the Einstein equation. A comparison of the proposed model

and the results of [126] is shown in Fig.11. 4 at a particle size of 286 K and 21 nm. The maximum error did not exceed 4%.

Figure 8.5 presents the measured data of the dynamic viscosity of Zr-water normalized to the viscosity of the water base as a function of volume fraction at a particle size of 10 nm at 303K [90] and calculated by the proposed model. The maximum error was below 4%.

In [134], freeze etching replication transmission electron microscopy (FERTEM) was used to characterize the microstructures of  $\text{CaCO}_3$ -water nanofluids at different particle volume fractions. It was concluded that the effective viscosity of  $\text{CaCO}_3$ -water nanofluids is related to aggregates of nanoparticles. The viscosity of  $\text{CaCO}_3$ -water is well predicted by the proposed model, as shown in Fig.8.6, with a maximum error of 3%.

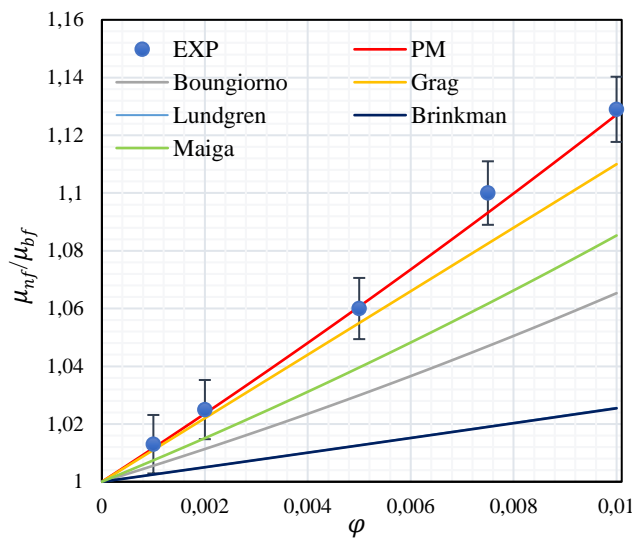


Figure 8.2. CNT-water (9.2nm, 293.15K) [54]

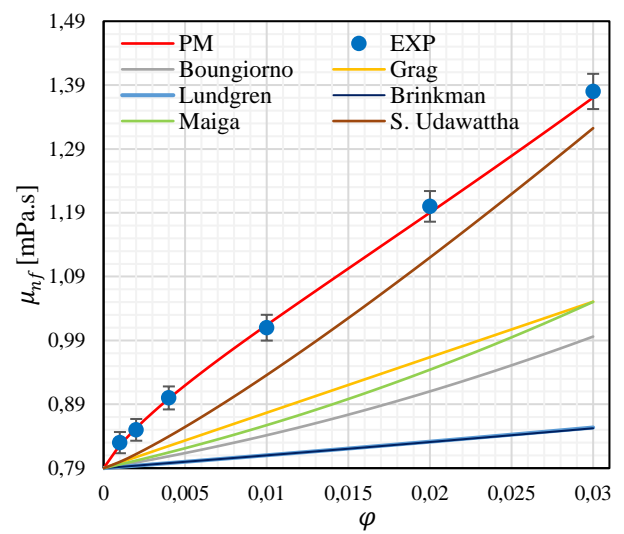


Figure 8.3.  $\text{Fe}_3\text{O}_4$ -water (25nm, 293K) [44]

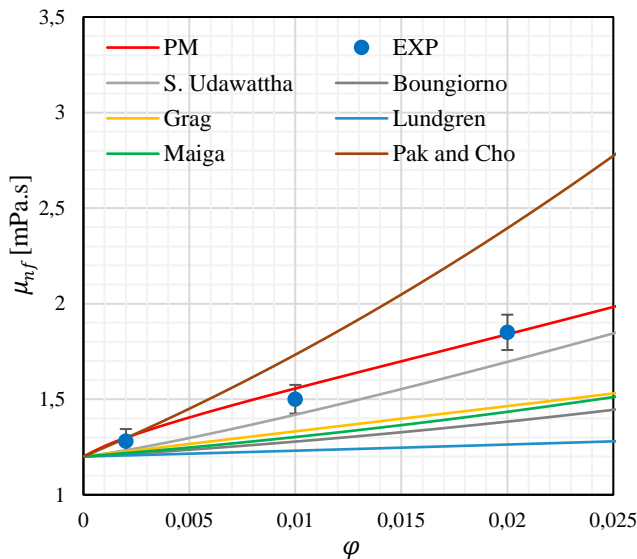


Figure 8.4.  $\text{TiO}_2$ -water nanofluids (21 nm, 286K) [126].

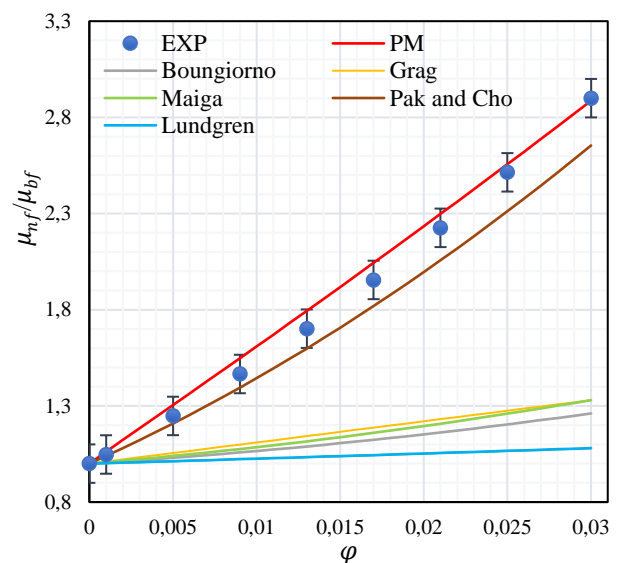


Figure 8.5. Zr-water (15 nm, 303K) [90]

Experimental work [43] was performed to investigate the viscosity of COOH-functionalized multiwalled carbon nanotubes with a water-based liquid using 22 concentrations as a function of

temperature. The main result shows that the increase in the volume fraction increased the viscosity of the water. The comparison of the authors' findings in [43] and the results of the proposed model is presented in Fig. 8.7. The maximum deviation is less than 2%.

To research the thermo-physical properties of nanofluids, Dalkilic et al. [125] produced graphite-pure water nanofluid with a particle size of 8 nm and a volumetric concentration ranging from 0 to 0.02 for temperatures between 293K and 333K for stabilized nanofluid produced with a sonicator and an ultrasonic bath. The authors presented an interesting comparison using an Artificial Neural Network (ANN) analysis with 32 empirical correlations. The variation of the viscosity models compared to the experimental result was between 3.507-127.151%. However, the maximum error with the proposed model is 5% on Fig. 11.8 for graphite-water with particle size 8 nm at 333K.

The effective viscosity of the SiO<sub>2</sub>-water nanofluid was determined between the volume fraction 0 to 5% in [57]. Figure 8.9 shows a comparison between the experimental work and the proposed model. The maximum error was less than 8%.

Khodadadi et al. [123] studied the rheological behavior of MgO dispersed in water nanofluid at various temperatures of 298-333 K and particle concentrations between 0.07% and 1.25%. The data obtained also showed that the viscosity increases with increasing volume fraction and decreases with increasing temperature. In Fig. 8.10, the experimental result for the viscosity of MgO-water with a particle diameter of 20 nm at 298K is compared with the proposed model, and the result shows an excellent agreement (<3 %) using the correction factor. Esfe et al [45] presented an equation for MgO-water with 40 nm particles that overestimates viscosity.

Mena et al. [122] presented experimental data for the nanofluid viscosity of Al<sub>2</sub>O<sub>3</sub>-water with a particle diameter of  $20 \leq d_p \leq 30$  nm, volume concentration of 0.5-4%, and a temperature between 283K and 298 K. A comparison of the viscosity models with the experimental result is shown in Fig. 11. The maximum error between the experimental data and the present model is less than 5%.

### 8.2.2 EG -BASED NANOFLUIDS

The stability of nanofluids prepared by dispersing Al<sub>2</sub>O<sub>3</sub> nanoparticles in ethylene glycol at various concentrations up to 25% by weight were studied in [120]. In the temperatures between 283.15 K and 323.15 K, the viscosity was evaluated experimentally. Viscosity increases with the increasing concentration of nanoparticles, while viscosity decreases with increasing temperature. The results of this experiment were compared with the results of the proposed model as shown in Fig. 8.12. The maximum error is less than 5%.

Copper nanoparticles dispersed in EG were prepared by a chemical reduction method. The nanoparticles were then dispersed in EG using a sonicator with a volume ratio of up to 2%.

Viscosity measurements show four times higher values than predicted by Einstein's correlation (see [47]). The error did not exceed 2% with the formula (8.13) we calculated. Figure 8.13 depicts the proposed model predictions against experimental data for Cu-EG with a particle size of 200 nm at 298K.

Various ZnO-EG nanofluids have been prepared using ZnO nanoparticles dispersed and synthesized in EG [129]. The result reported that the increase in volume fraction increased the interactions between nanoparticles and has an effect on volumetric trends. The rheological behavior was Newtonian, and the viscosity increased with concentration and decreased with temperature. Figure 8.14 represents the viscosity of ZnO-EG nanofluids at 100 nm and 293K [129]. The error is below 2%.

Akbari et al. [76] studied the viscosity of SiO<sub>2</sub> as a function of temperature and concentration. Experiments were performed on SiO<sub>2</sub> with a volume fraction of 0.1-3% and a temperature range of 303K to 323K. According to the experimental results, all nanofluid samples behaved as Newtonian fluids at all applied temperatures. Viscosity measurements show that the viscosity increases with increasing volume ratio of nanoparticles and decreases with increasing temperature; it gives a maximum increase of 116% of the viscosity at 3% concentration. The application of the proposed model to predict the viscosity of SiO<sub>2</sub>-EG (20-30 nm) at 313K is shown in Fig. 8.15. The maximum error is less than 4%.

Figure 8.16 shows the viscosity of hexagonal boron nitride (hBN)-EG nanofluids with a particle size of 70 nm at 298K [127]. In comparison, the proposed model shows excellent accuracy of less than 1%.

Figure 8.17 illustrates the dynamic viscosity of Fe normalized with EG-based fluid. Using the proposed model, the dynamic viscosity as a function of volume fraction was calculated and compared with the measurement points (35–45 nm) of Fe-EG nanofluids at 328K [48]. The maximum error is below 4%.

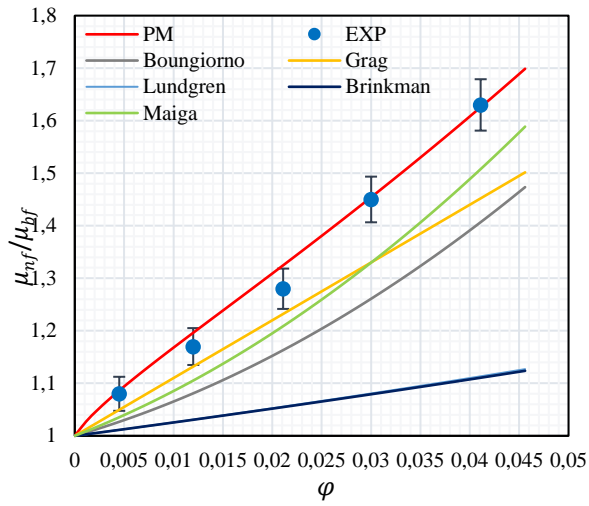
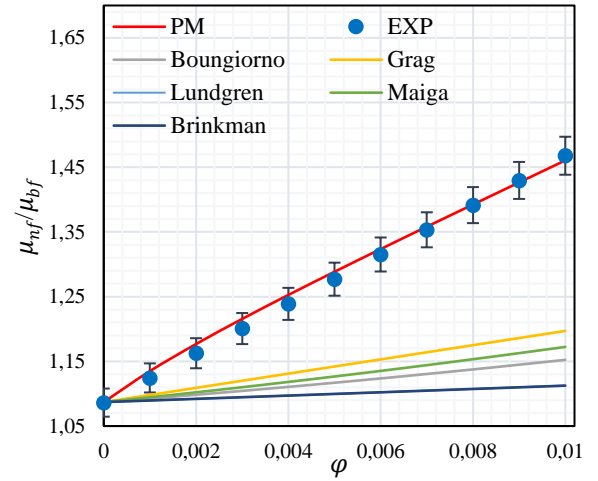
Figure 8.6. CaCO<sub>3</sub>-water (20–50 nm, 293K) [134]

Figure 8.7. MWCNT-water (5–10 nm, 293K) [43]

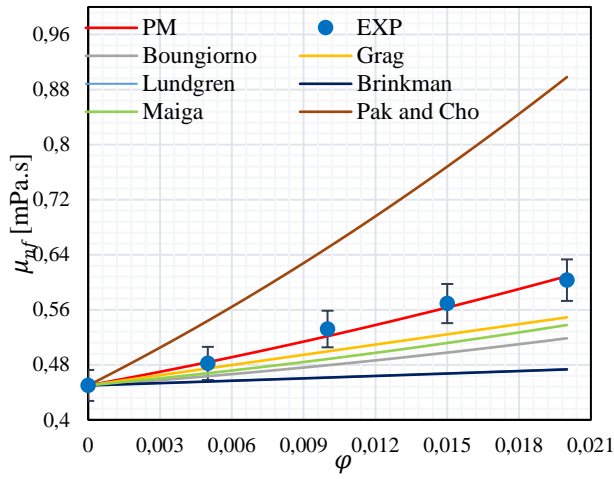


Figure 8.8. Graphite-water (10 nm, at 333K) [125]

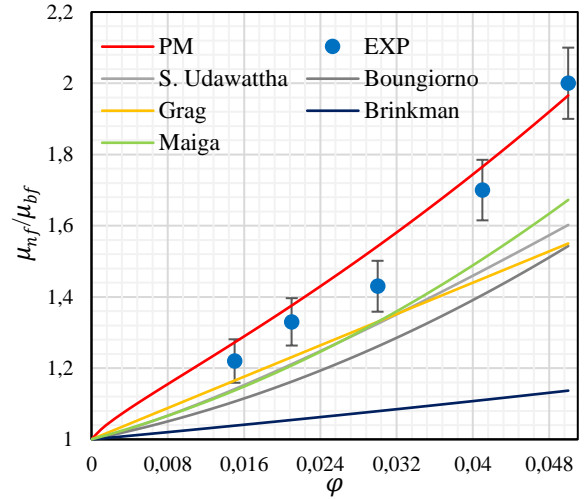
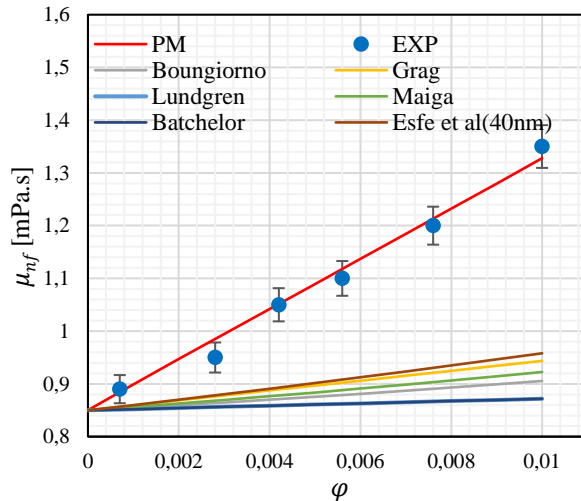
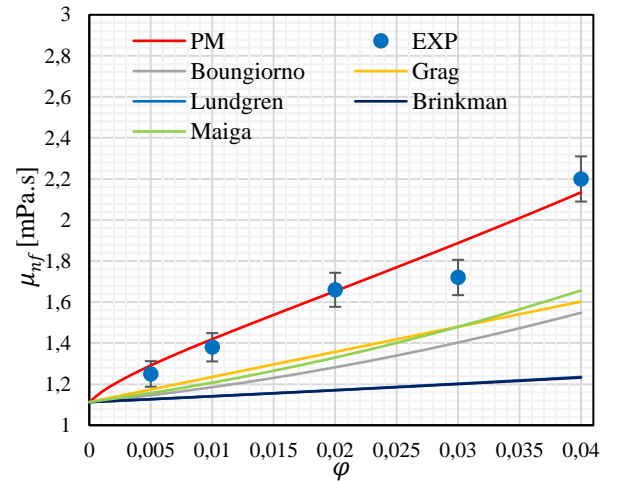
Figure 8.9. SiO<sub>2</sub>-water (35 nm, 328K) [57]

Figure 8.10. MgO-water (20 nm, 289K) [45]

Figure 8.11. Al<sub>2</sub>O<sub>3</sub>-water (20 nm, 288K) [122]

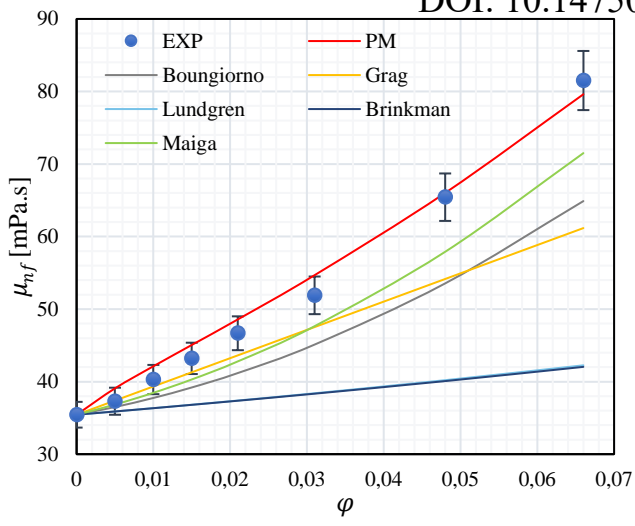
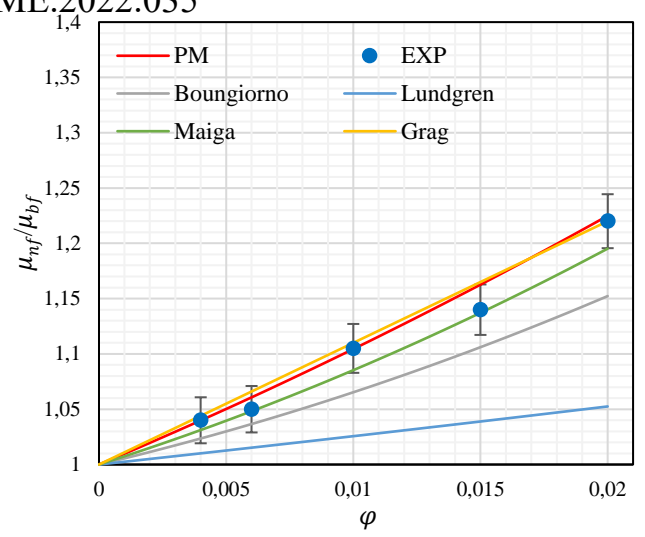
Figure 8.12. Al<sub>2</sub>O<sub>3</sub>-EG (43±23 nm, 283K) [120].

Figure 8.13. Cu-EG (200 nm, 298K) [47]

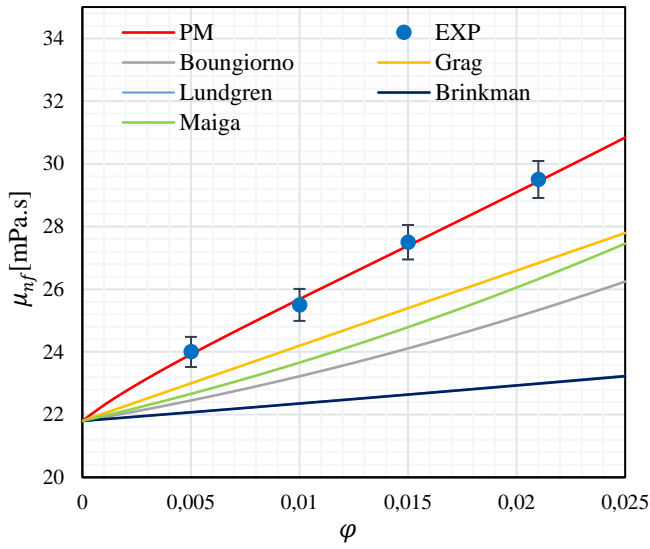


Figure 8.14. ZnO-EG (100nm, 293K) [129]

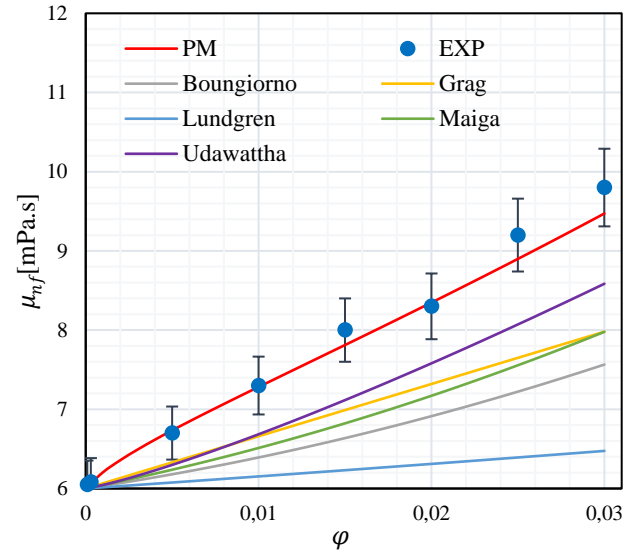
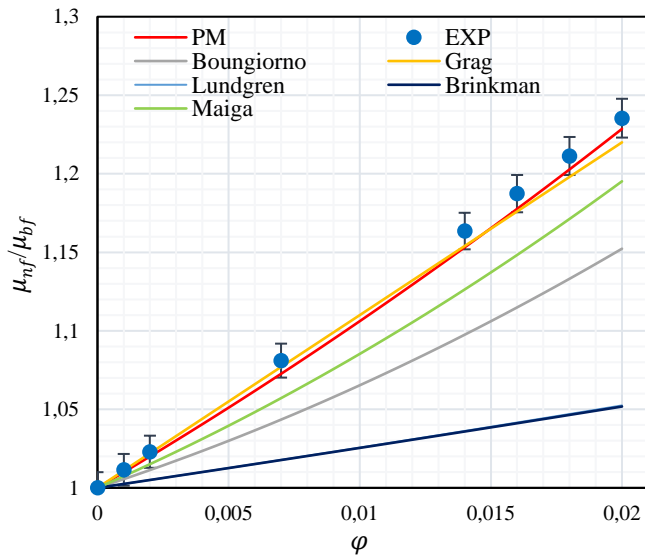
Figure 8.15. SiO<sub>2</sub>-EG (20-30 nm, 323K) [76]

Figure 8.16. hBN-EG (70nm, 298K) [127]

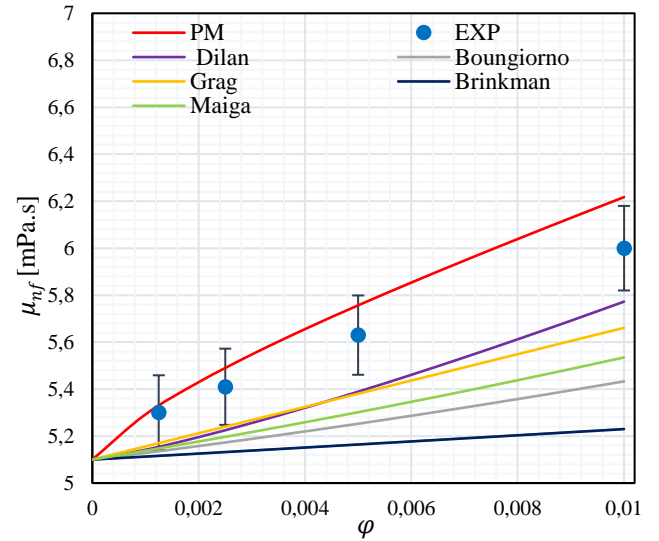


Figure 8.17. Fe-EG (35-45 nm, 328K) [48]



### 8.2.3 OTHER BASE FLUIDS

A mixture of 60% water and 40% EG has been investigated with the aim of finding the benefits of using two different conventional heat transfer fluids to improve energy system performance. In work [50], experimental data on the viscosity properties of SiC-EG water (60; 40) with a particle size of 30 nm and volume fractions of 0.002, 0.004, 0.006, 0.008, 0.01 were presented. The authors' finding for these viscosities was that the nanofluid behaves as a Newtonian fluid and the viscosity decreases with increasing temperature.

A comparison of the measured viscosity result with the proposed model is shown in Fig. 8.18 at 283 K, where the maximum error does not exceed 2%.

Figure 8.19 depicts the viscosity of Fe<sub>3</sub>O<sub>4</sub>-toluene at 293 K with a particle size of 10 nm as described in [49] for different particle concentrations. The viscosity of the nanofluid decreases with temperature, which is comparable to the properties of the carrier fluid. A comparison of (8.13) for Fe<sub>3</sub>O<sub>4</sub>-toluene with the experimental results shows a good agreement. The maximum error is less than 3%.

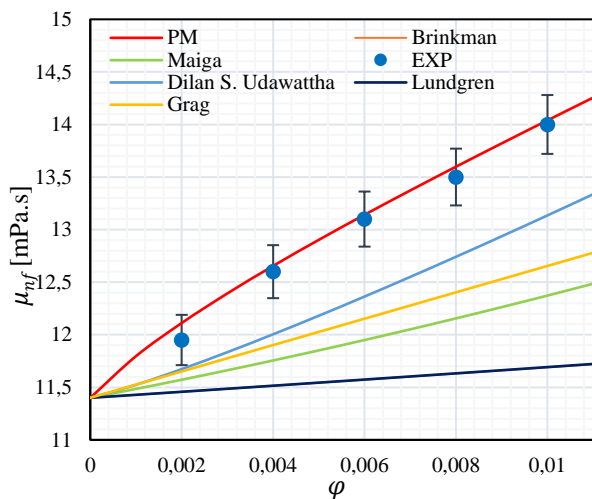


Figure 8.18. SiC-EG-water (60;40) (30 nm, 283K) [50]

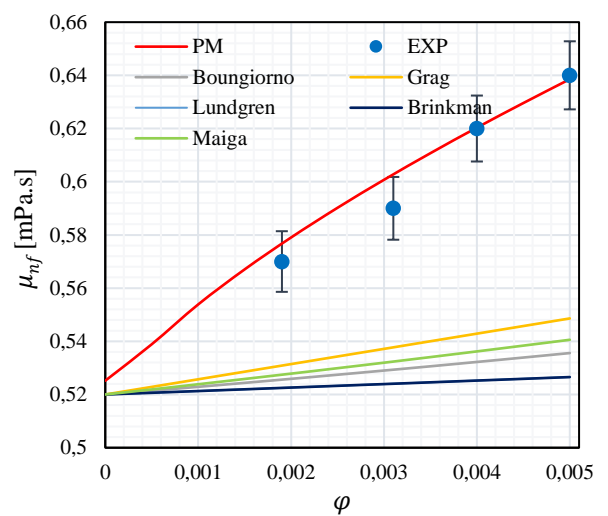


Figure 8.19. Fe<sub>3</sub>O<sub>4</sub>-toluene (10nm, 293K) [49]

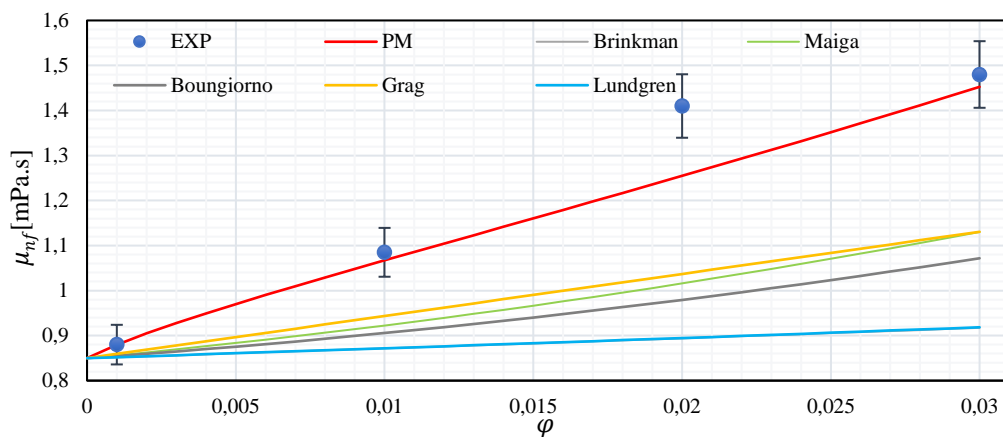


Figure 8.20. SiC-DIW (25 nm, 303K) [124]

The dispersion viscosity behaviour of SiC-DIW nanofluids as a function of volume fraction was studied in [124]. A comparison of the proposed model and the experimental results is shown in Fig. 8.20. The maximum error is less than 5%.

In the following, we analyse the impact of temperature on the viscosity of the nanofluid and examine the accuracy of the equation (8.13) for the prediction of the viscosity of the nanofluid. Experimental results on the effect of temperature on dynamic viscosity show that an increase in the temperature of the nanofluid leads to a decrease in the dynamic viscosity, and the declination of the dynamic viscosity can be attributed to a factor such as the motion of nanoparticles on micron scale. Studies show that micro-convection of nanoparticles in the base fluid reduces intermolecular forces between the base fluid molecules. The results of the proposed model also showed that with increasing temperature, the dynamic viscosity of nanofluid decreases significantly. As the temperature increases, the molecular velocity of the nanoparticles increases due to the Brownian motion of the nanoparticles [115]. Increasing the random velocity of the nanoparticles leads to a decrease in the intermolecular forces between the base fluid and the surface of the nanoparticles, resulting in higher viscosity at lower temperatures.

The viscosity change of the nanofluid with the temperature was investigated according to the model (8.13) and the accuracy of the proposed model was validated with the measured data. In the proposed model the last term is strongly influenced by temperature, the numerator is proportional to  $\sqrt{T}$  and the denominator is influenced by the correction factor  $C(T, \varphi) = D_1 T^{-B_1} + D_2 \varphi^{-B_2}$  with  $T^{-B_1}$  and  $\mu_{bf}$  is also dependent on  $T$ .

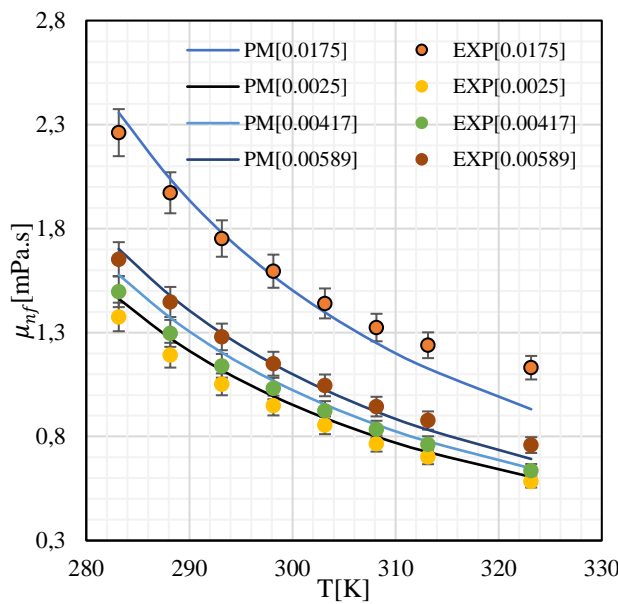


Figure 8.21. CuO-water 11±3 nm at different volume fractions [58]

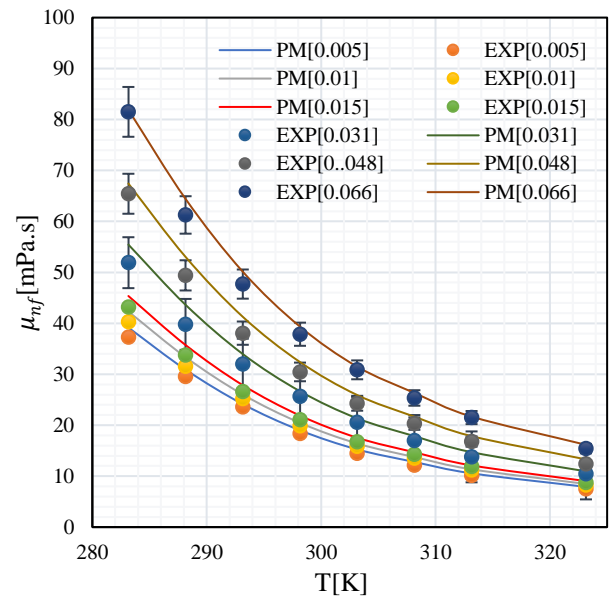


Figure 8.22. Al<sub>2</sub>O<sub>3</sub>-EG at different volume fractions [120]

As the temperature increases, the viscosity of the base fluid decreases. The two parameters, the viscosity of the base fluid and the Brownian viscosity affect the viscosity of the nanofluid. The nanofluid viscosity of CuO-water was determined according to the method of [58] with particle size  $11 \pm 3$  nm at the following temperatures: 283.15, 288.15, 293.15, 298.15, 303.15, 308.15, 313.15, and 323.15 K. Figure 8.21 shows a comparison of CuO-water at different temperatures and concentrations, and the comparison shows a good agreement between the published measurement results and the proposed model. The maximum error is less than 5%.

Nanofluids prepared by dispersing  $\text{Al}_2\text{O}_3$  nanoparticles in ethylene glycol have been tested at various concentrations up to 25% mass fraction [120]. At temperatures between 283.15 K and 323.15 K, the viscosity was determined experimentally with a rotational viscometer. They discovered that as the concentration of nanoparticles increases, viscosity increases, but as temperature increases, viscosity decreases. The new experimental viscosity values are more than double those of the base fluid. A comparison of the experimental results of  $\text{Al}_2\text{O}_3$ -EG with  $d_p = 43 \pm 23$  nm diameter is illustrated in Fig. 8.22.

Several researchers have published conflicting results regarding the relationship between temperature, nanoparticle diameter, nanoparticle volume concentration, and nanofluid viscosity. Mena et al. [122] attempted to obtain an approximate expression for the systematic evaluation of the viscosity of  $\text{Al}_2\text{O}_3$ -water in the simulation of heat transfer applications in the temperature range of 283–298 K and nanoparticle volume fractions below 1%. Their work presents a methodology for extrapolating a correlation in the validity range. Within this narrow temperature and volume percentage ranges, new experimental data were collected for the nanofluid viscosity of  $\text{Al}_2\text{O}_3$ -water. A comparison of the experimental data with the proposed  $\text{Al}_2\text{O}_3$ -water model for  $20 < d_p < 30$  nm diameter shows an excellent agreement as shown in Fig. 8.23.

Based on experimental data [125] for the nanofluid viscosity of graphite-water with a diameter of 6–10 nm at 293–333 K, it was found that the dynamic viscosity of nanofluid increases with decreasing temperature and increasing concentration. Figure 8.24 shows a comparison of the present model with the experimental results. The maximum error is less than 5%. Figure 8.25 shows the viscosity of  $\text{Fe}_3\text{O}_4$  water with a diameter range of 20–30 nm at different temperatures and a comparison of the present model with the experimental results published in [44], which gives an excellent agreement. Furthermore, the validation of the model with the experimental result [76] of  $\text{SiO}_2$ -EG with a particle size of 20 nm is shown in Fig. 8.26. The maximum error is less than 5%.

The diameter of the nanoparticles has a significant effect on the viscosity of the nanofluid, which requires an examination of the accuracy of the model for predicting the viscosity ratio and viscosity of the nanofluid. Examining the accuracy of the proposed model for the viscosity of nanofluids of different diameters, containing  $\text{Al}_2\text{O}_3$ ,  $\text{CuO}$ ,  $\text{Fe}$ ,  $\text{Fe}_3\text{O}_4$ ,  $\text{SiC}$ ,  $\text{ZnO}$ ,  $\text{AlN}$ ,  $\text{TiO}_2$ ,  $\text{SWCNT}$ ,  $\text{Ag}$ ,  $\text{SiO}_2$ ,  $\text{MWCNT}$ ,  $\text{DWCNT}$ ,  $\text{SWCNT}$ ,  $\text{CaCO}_3$ ,  $\text{hBN}$ ,  $\text{MgO}$  and graphite, our analyses show an excellent agreement.

Pastoriza-Gallego et al. in [18] studied the nanofluid viscosity of  $\text{CuO}$ -water. The viscosity of two different samples was experimentally measured. The researchers examined two separate samples, the first S1 with commercially available dry  $\text{CuO}$  nano-powder and the second S2 with

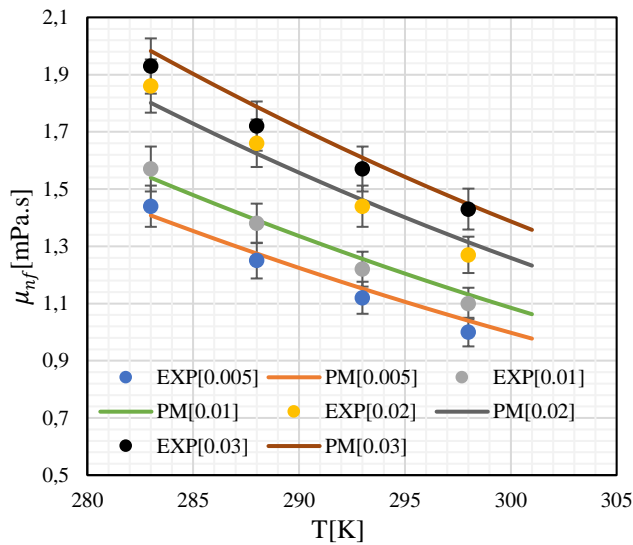


Figure 8.23.  $\text{Al}_2\text{O}_3$ -water at 20-30 nm at different volume fractions [122]

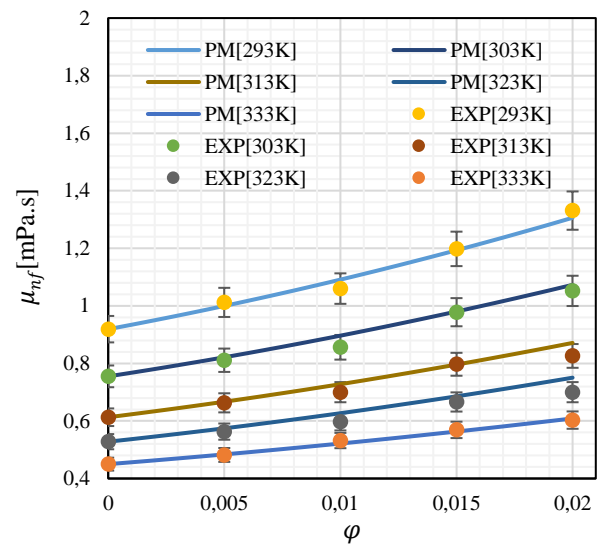


Figure 8.24. Graphite-water, particle size 6-10 nm at different temperatures [125]

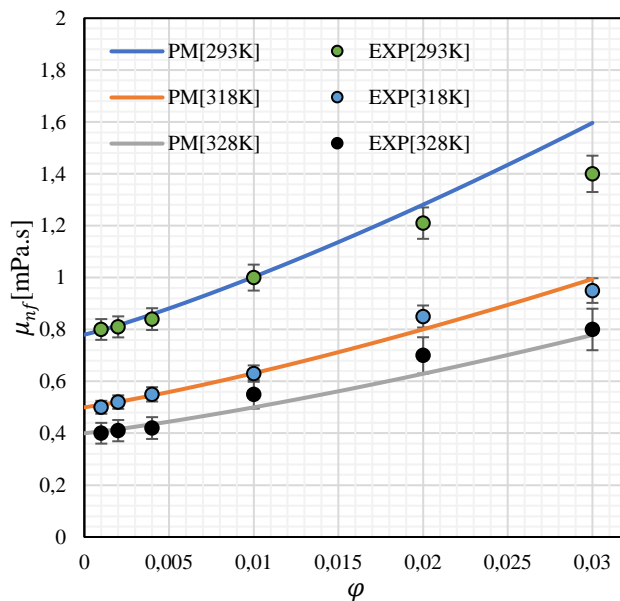


Figure 8.25.  $\text{Fe}_3\text{O}_4$ -water at 25nm at different temperatures [44]

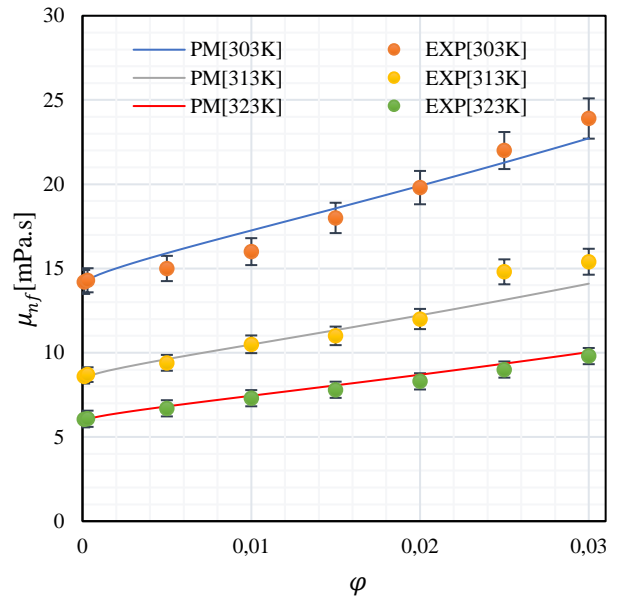


Figure8. 26.  $\text{SiO}_2$ -EG 20 nm at different temperatures [76]

synthesized CuO nanoparticles prepared by a precipitation method. The average diameter of S2 nanoparticles is smaller than that of S<sub>1</sub>, and the particle size distribution of S2 is narrower than that of S<sub>1</sub>. Figure 8.27 presents the sensitivity of the model to the particle size and is based on the experimental results of the two samples. According to the experimental results, the increase of the particle size significantly affects the viscosity of the nanofluid, and the viscosity decreases with the increase of the particle size.

Pastoriza-Gallego et al. [120] reported experimental results for another Al<sub>2</sub>O<sub>3</sub>-EG tests for two samples with diameters S<sub>1</sub> = 8 ± 3 nm and S<sub>2</sub> = 43 ± 23 nm. The effect of this change in diameter is shown in Fig. 8.28. A comparison with the proposed model shows an excellent agreement.

Figure 8.29 illustrates the effect of particle size ranges on the viscosity. It can be seen that the viscosity of the nanofluid increases compared to the base fluid, and on the other hand, the particle size affects both the static and dynamic viscosity parts. The proportion of the part from the Brownian motion is significantly larger at small diameters than at larger particle sizes. It can be observed that according to the present model, the viscosity of the nanofluid increases with decreasing particle size. We found that the use of the average diameter is the most accurate in the present model.

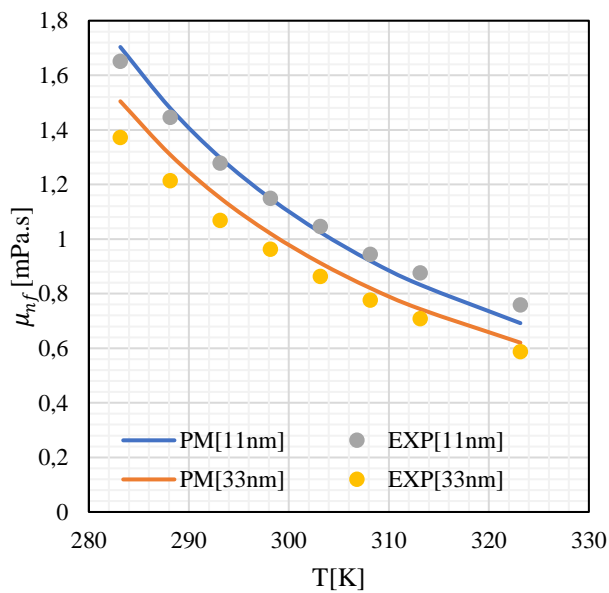


Figure 8.27. Experimental viscosity (0.00589) CuO-water [58]

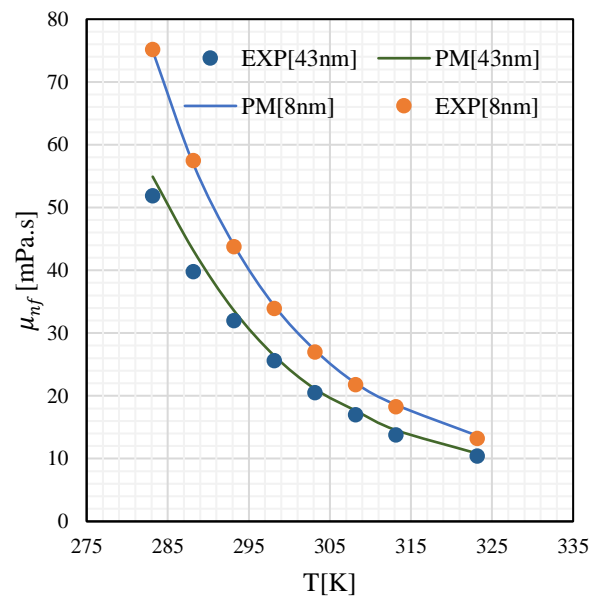


Figure 8.28. Al<sub>2</sub>O<sub>3</sub>-EG viscosity for different particle diameter [120]

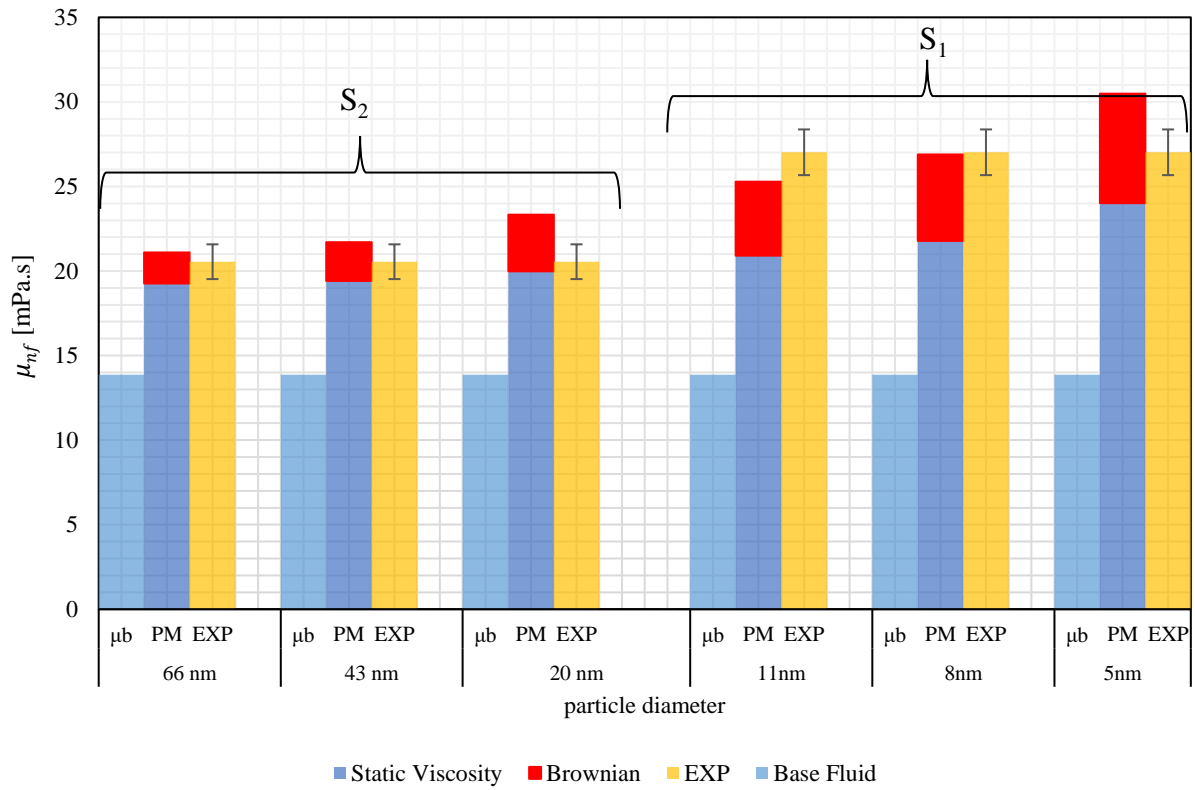


Figure 8.29. Al<sub>2</sub>O<sub>3</sub>-EG at volume fraction 0.031 and diameter range S<sub>1</sub>=8±3 and S<sub>2</sub>=43±23 at T=303K [120]

The study of the effective viscosity of nanofluids consists of two parts, static and dynamic viscosity and a novel viscosity equation is proposed. Static viscosity is a combination of different theoretical and experimental models, and the viscosity is affected due to the nanolayer. The concept of the impact of a nanolayer is that a nanolayer is formed around a particle and has a thickness of about 1 nm, and the dynamic part is due to the Brownian motion of the particles. We proposed for the Brownian motion viscosity a correction factor of two power forms with four parameters. The parameters are given in Table 8.4 and are independent of the type of the base fluid.

The size of the nanolayer has been investigated in [135], where Yu and Choi clearly demonstrated the effect of the assumption of the nanolayer thickness  $h$ . Since there is currently no method for estimating  $h$ , we determined  $a$  by fitting the experimental data. The predicted viscosity for the spherical shape is equal to 1 nm, and for the nanotube  $h = 2$  nm. However, the error does not exceed 5% for any of the 293K values of MWCNT-water nanofluids (5–10 nm) [43]. A comparison on the nanolayer thickness has been made for  $h = 1$  nm, and  $h = 2$  nm for graphite-water with particle size 10 nm at 333K, and the effect of the assumption was insignificant at low volume fraction and increased gradually with the increase of the volume fraction. The effect of the nanolayer assumption on the accuracy of the model was also studied for different spherical

nanoparticles at different temperatures. A comparison of CuO-water with a particle size of 45 nm at different temperatures was performed with [58]. The result shows that the effect of the size of the nanolayer is negligible on partly large particles.

The assumed effect of the nanolayer on the prediction of MWCNT-water nanofluids (5–10 nm) at 293K was compared with [3] at different volume fractions. The assumption  $h = 2$  has been overestimated the experimental results but  $h = 1$  underestimated them. The error is less than 2% for both cases.

In summary, equation (8.13) successfully predicts the viscosity of different nanofluids in different diameter ranges. The validated range was between 3 nm and 200 nm. The comparison between the experimental results and different existing models shows an underestimate of the viscosity. Examples for the gap between the experimental result and the existing models is presented in Fig. 8.30.

The parameters in the correction factor were determined using several experimental results, and the correction formula was tested with about 50 different nanofluids. Approximately 1,300 experimental viscosity values were used to test the new model, 87% of which are within the 0.9-0.99% correlation coefficient.

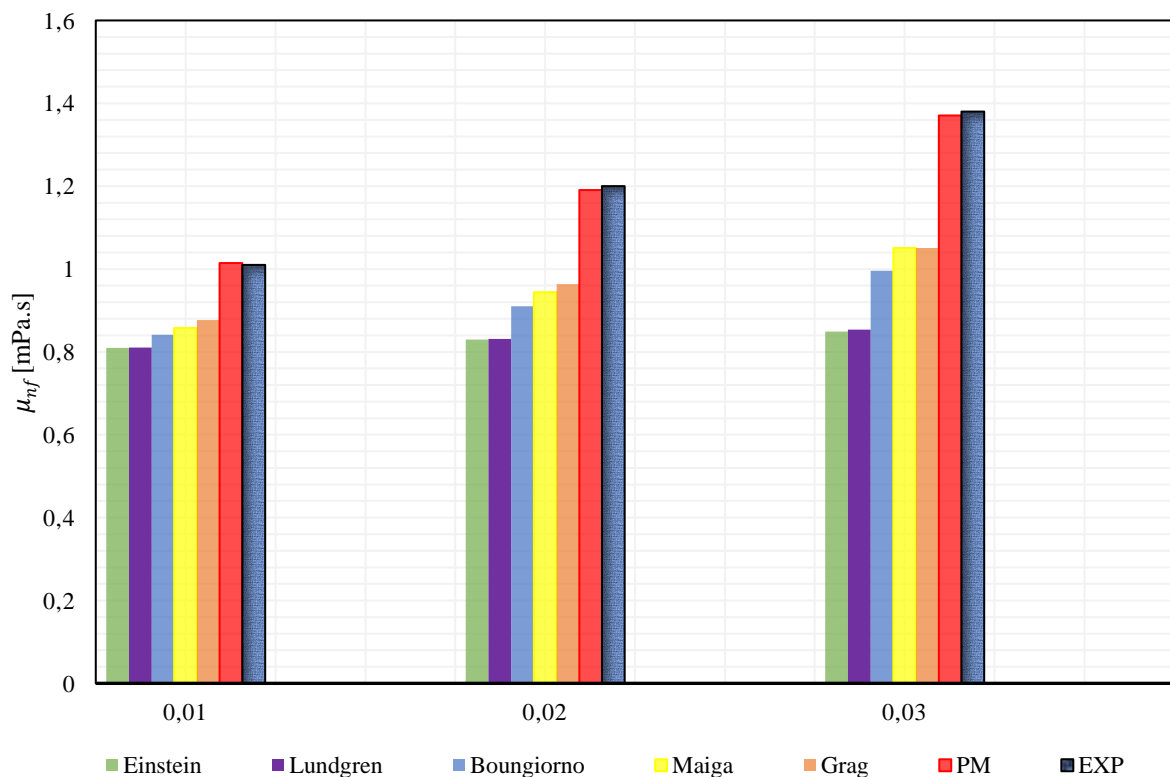


Figure 8.30. Comparison of the experimental results [44] and the existing models,  $\text{Fe}_3\text{O}_4$ -water (25nm, 293K)

### 8.3 APPLICATION OF THE NEW MODEL IN NUMERICAL SIMULATION

The two-dimensional flow geometry with BFS which presented in Figure 6.1. The applicability of the proposed equation is examined to verify how the accuracy of the proposed equation can effect the numerical solutions. The viscosity was modelled using the proposed viscosity equation in (8.13) as introduced in equation 8.13. Figure 8.31 present the result comparison of the proposed equation with the experimental result. It can be seen that the proposed equation has significantly more accurat viscosity value in comparison to Maiga et al. equation (see [27]).

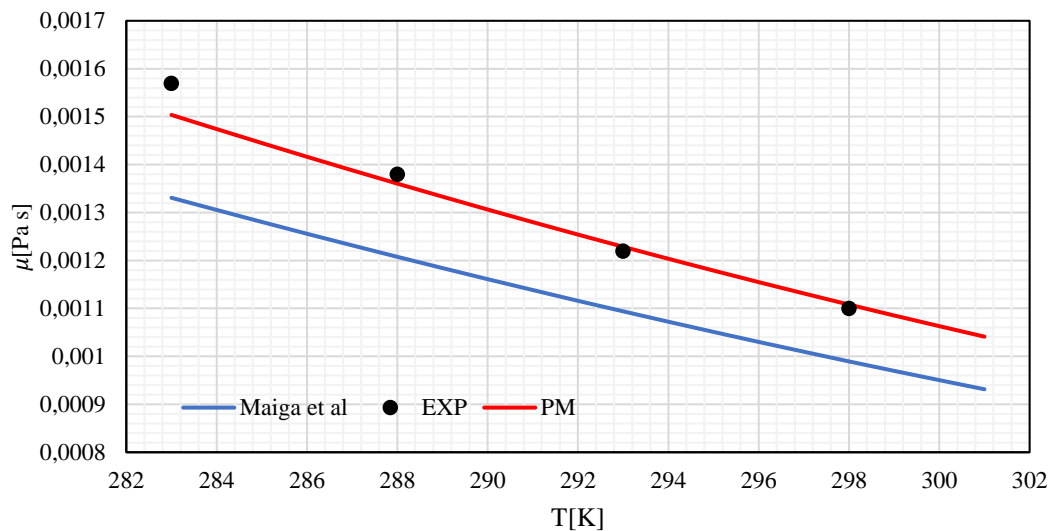


Figure 8.31. The viscosity obtained by the viscosity equation for  $\text{Al}_2\text{O}_3$  at 1% volume fraction

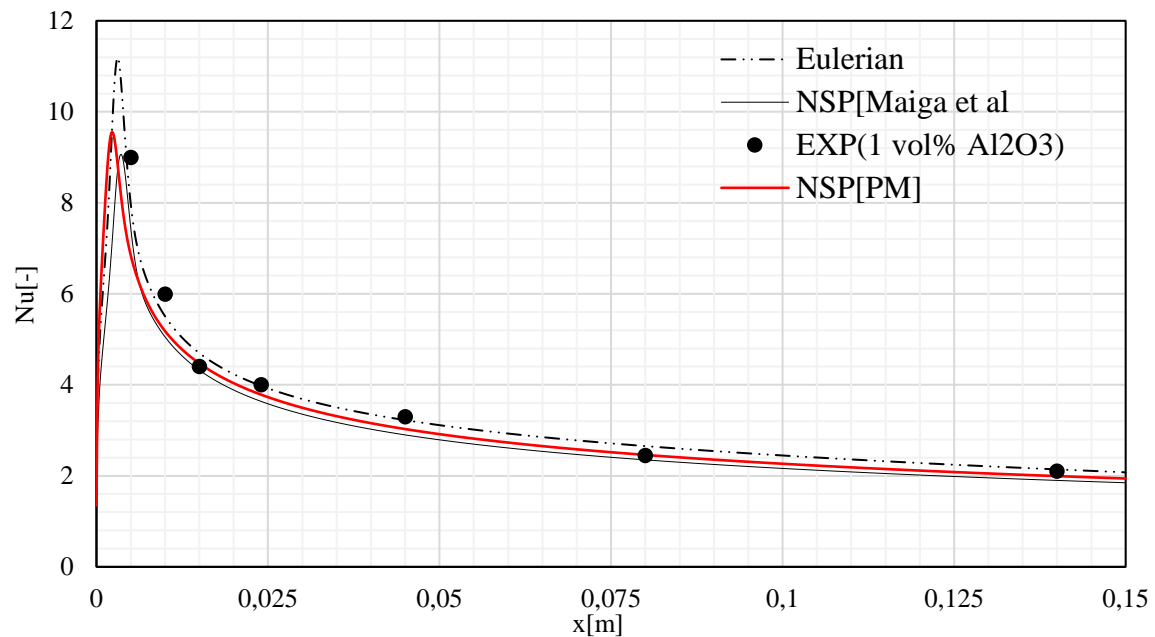


Figure 8.32. Comparison of Nusselt number using the proposed viscosity model



Figure 8.32 shows a comparison of the proposed viscosity equation with the single-phase method. As can be seen, the viscosity model improved the prediction of Nu number and reduced the discrepancies between the experimental data and the numerical solution. Table 8.3 gives the percentage difference between the Nu values obtained with the Maiga et al. viscosity model and the proposed equation compared to the measured values. The error decreases along the downward sloping wall, and the average error is reduced to 7.88% compared to the values obtained with the Maiga et al. model. Using the single-phase model, the reduction in error is reduced from 10.213% to 7.88% using the proposed viscosity equation.

Table 8.3. Comparison of the Nuselt number using the proposed viscosity equation

<b>Models position</b>	<b>NSP [27]</b>	<b>NSP Present Model</b>
X <sub>1</sub>	-18.884	-24.658
X <sub>2</sub>	-15.847	-13.718
X <sub>3</sub>	-1.8147	1.569
X <sub>4</sub>	-9.136	-5.443
X <sub>5</sub>	-12.171	-8.285
X <sub>6</sub>	-4.064	0.389
X <sub>7</sub>	-9.574	-5.0665
Ave-Error	-10.213	-7.8875

## NEW SCIENTIFIC RESULTS OF THE THESES

The main contributions from the research can be summarised as follows:

**TH1.** The comparison between solutions obtained by the similarity method and CFD is performed to determine the impact of neglect in the similarity procedure, the impact of the nanoparticle types, and volume fraction on the nanofluid flow properties. The results reported that the differences between the two solutions depending on the volume fraction. The simulation results obtained by CFD gave larger values for  $Re_x^{1/2} C_f$  and  $Re_x^{-1/2} Nu$ , which indicates that the skin friction should be slightly higher in reality than the value calculated according to boundary layer theory. The difference became more significant when the volume fraction increases. For water, the difference is less than 2.3% and the minimum is obtained as 0.177% for Fe<sub>3</sub>O<sub>4</sub>-water of volume fraction 4% in the range  $0 < \phi < 4\%$ . The comparison of the Nusselt number shows the same relation where the maximum error is 6.7% for water, and the minimum difference is 1.9% for Fe<sub>3</sub>O<sub>4</sub> -water at a 4% volume fraction [K10, K12].

**TH2.** In the Blasius and Sakiadis flow analysis with constant thermo-physical properties are considered. The study of thermal and hydrodynamic layers shows that the flow and heat transfer characteristics of the fluid are significantly affected by the volume fraction. My research reported that the dimensionless velocity, skin friction, Nusselt number, and dimensionless temperature increase with increasing volume fraction [K8].

**TH3.** For water-based nanofluids of Al<sub>2</sub>O<sub>3</sub>, Fe<sub>3</sub>O<sub>4</sub>, and TiO<sub>2</sub>, I investigated the effect of nanoparticle types on velocity, temperature distribution, Nusselt number, and skin friction in flow over a plane surface. For Blasius flow, flow over a steady surface, the highest velocity and skin friction are obtained for Fe<sub>3</sub>O<sub>4</sub> water. The Nusselt number is highest for Al<sub>2</sub>O<sub>3</sub> nanoparticles and lowest for TiO<sub>2</sub>. For a Sakiadis flow, flow over a moving surface, the highest velocity and temperature values are obtained for Al<sub>2</sub>O<sub>3</sub>-water fluid, followed by Fe<sub>3</sub>O<sub>4</sub> and TiO<sub>2</sub>. The skin friction coefficient for Al<sub>2</sub>O<sub>3</sub> is lower than for TiO<sub>2</sub> and Fe<sub>3</sub>O<sub>4</sub>. I found that the type of nanofluid is a critical factor in improving heat transfer, where the highest heat transfer improvement is reported for Al<sub>2</sub>O<sub>3</sub>, followed by Fe<sub>3</sub>O<sub>4</sub> and TiO<sub>2</sub> [K4, K5, K7].

**TH4.** I have investigated the application of  $\text{Al}_2\text{O}_3$  and  $\text{TiO}_2$ -water nanofluids in backward-facing step geometry with heat flow for different volume fractions and Reynolds numbers using the Performance Efficiency Index (PEI), and the PEI is approximated by the volume fraction as follows:

$$PEI(\text{TiO}_2) = 1240.7\varphi^3 - 116.31\varphi^2 + 1.6322\varphi + 1.0017 \text{ with } R^2 = 0.9957$$

$$PEI(\text{Al}_2\text{O}_3) = 1324.7\varphi^3 - 119.76\varphi^2 + 1.2082\varphi + 1.0018 \text{ with } R^2 = 0.9972$$

The comparison of  $\text{Al}_2\text{O}_3$  and  $\text{TiO}_2$  shows that  $\text{TiO}_2$  is more efficient than  $\text{Al}_2\text{O}_3$ , and the greatest performance is obtained at a volume fraction of 1% [K3, K6, K9, K11].

**TH5.** I compared the simulation results for single-phase and two-phase models with constant and temperature-dependent thermophysical properties for the heat flux of the BFS problem. My results showed that the temperature-dependent models resulted in higher heat transfer coefficients and Nusselt numbers and lower temperatures in  $\text{Al}_2\text{O}_3$ -water nanofluids. In addition to higher Nusselt number predictions, the accuracy of the single-phase models increased when the results of these models underpredicted the Nusselt number compared to the experimental results. In turn, the accuracy was 3.395% for NSP, while it improved to 3.07% for non-NSP and to 2.708% for the Eulerian model. When using temperature-dependent formulae, the accuracy of the Euler model was significantly better than the other two-phase models, with an average error of 1.0420%. However, when the temperature-dependent formula was applied, the VOF and mixture models overestimated the Nusselt number, with an increase in an average error of more than 10% [K2].

**TH6.** I proposed a new viscosity equation (1) to determine the effective viscosity of a fluid containing homogeneously dispersed rigid and spherical nanoparticles. I used about 1300 experimental viscosity values to test the new model, 87% of which are within the correlation coefficient of 0.9-0.99. The application of the new viscosity model has improved the prediction accuracy of nanofluid viscosity, and its use in numerical simulations increases the accuracy of the numerical simulation method results. The application of the proposed viscosity equation to the Newtonian single-phase model increased the accuracy by 2.32% when compared with the measured results of  $\text{Al}_2\text{O}_3$ -water nanofluid flow in BFS geometry [K1].

## **ACKNOWLEDGEMENTS**

Apart from my efforts, the success of this thesis depends largely on the encouragement and guidelines of many others. Therefore, I would like to take this opportunity to express my gratitude to the people who have been instrumental in completing this work.

To Prof. Dr. Gabriella Vadászné Bognár, my supervisor, and my second family in Hungary. Thank you for your precious guidance, advice, dynamism, and friendship. Without your help, this research would never have come to fruition. Your wisdom, insight, diligence, and research passion taught me a lot. It was an honor for me to work under your supervision. I am glad to meet you and collaborate with you,

To my family. For many years, they have offered everything possible to support me. Without their encouragement, I would not be here. This thesis is dedicated to them. I would also like to especially thank my dear sisters, who restored my hope in life during my long absence.

To Anca Dolhescu, thanks to my hero lady and biggest supporter who endured this long process with me, always offering support and love.

## REFERENCES

- [1] Y. I. C. Bock Choon Pak, "Hydrodynamic and Heat Transfer Study of Dispersed Fluids With Submicron Metallic Oxide," *Exp. Heat Transf. A J. , Therm. Energy Transp. , Storage , Convers.*, no. January 2013, pp. 37–41, 2013.
- [2] G. Bognár, M. Klazly, and K. Hriczó, "Nanofluid flow past a stretching plate," *Processes*, vol. 8, no. 7, 2020.
- [3] H. Blasius, "THE BOUNDAR LAYER IN FLUIDS WITH LITTLE FRICTION," *NACA TM 1266*, pp. 1–57, 1098.
- [4] G. Bognár, "Similarity solution of boundary layer flows for non-Newtonian fluids," *Int. J. Nonlinear Sci. Numer. Simul.*, vol. 10, no. 11–12, pp. 1555–1566, 2009.
- [5] G. National and H. Pillars, *Altan, T.; Oh, S.; Gegel, G. Metal Forming Fundamentals and Applications; ASM International: Cleveland, OH, USA, 1983.*
- [6] Sakiadis, B.C. Boundary-layer behaviour on continuous solid surfaces: I. Boundary-layer equations for two-dimensional and axisymmetric flow. *AIChE J* 1961, 7, 26–28.
- [7] Tsou, F.; Sparrow, E.; Goldstein, R. Flow and heat transfer in the boundary layer on a continuous moving surface. *Int. J. Heat Mass Transf.* 1967, 10, 219–235.
- [8] Crane, L.J. Flow past stretching plate. *Z. Angew. Math. Phys.* 1970, 21, 645–647.
- [9] Chakrabarti, A.; Gupta, A.S. Hydromagnetic flow and heat transfer over a stretching sheet. *Q. Appl. Math.* 1979, 37, 73–78.
- [10] Bognár, G.V.; Csáti, Z. Numerical Solution to Boundary Layer Problems over Moving Flat Plate in Non-Newtonian Media. *J. Appl. Math. Phys.* 2014, 2, 8–13.
- [11] Bognár, G.V. On similarity solutions of boundary layer problems with upstream moving wall in non-Newtonian power-law fluids. *IMA J. Appl. Math.* 2011, 77, 546–562.
- [12] Haider, S.; Butt, A.S.S.; Li, Y.-Z.; Imran, S.M.; Ahmad, B.; Tayyaba, A. Study of entropy generation with multi-slip effects in MHD unsteady flow of viscous fluid past an exponentially stretching surface. *Symmetry* 2020, 12, 426.
- [13] Mahabaleswar, U.S.; Kumar, P.V.; Nagaraju, K.R.; Bognár, G.; Nayakar, S.N.R. A new exact solution for the flow of a fluid through porous media for a variety of boundary conditions. *Fluids* 2019, 4, 125. [CrossRef].
- [14] Andersson, H.I.; Aarseth, J.B. Sakiadis flow with variable fluid properties revisited. *Int. J. Eng. Sci.* 2007, 45, 554–561.
- [15] Tonekaboni, S.A.M.; Abkar, R.; Khoeilar, R. On the Study of Viscoelastic Walters' B Fluid in Boundary Layer Flows. *Math. Probl. Eng.* 2012, 2012, 1–18. [CrossRef].
- [16] Siddheshwar, P.; Mahabaleswar, U.; Chan, A. MHD flow of walters' liquid b over a nonlinearly stretching sheet. *Int. J. Appl. Mech. Eng.* 2015, 20, 589–603.
- [17] Singh, J.; Mahabaleswar, U.S.; Bognar, G. Mass transpiration in nonlinear MHD flow due to

- porous stretching sheet. *Sci. Rep.* 2019, 9, 1–15. [CrossRef].
- [18] Takhar, H.S.; Nitu, S.; Pop, I. Boundary layer flow due to a moving plate: Variable fluid properties. *Acta Mech.* 1991, 90, 37–42.
- [19] Pop, I.; Gorla, R.S.R.; Rashidi, M. The effect of variable viscosity on flow and heat transfer to a continuous moving flat plate. *Int. J. Eng. Sci.* 1992, 30, 1–6.
- [20] M. M. Bhatti, H. F. Öztop, R. Ellahi, I. E. Sarris, and M. H. Doranehgard, “Insight into the investigation of diamond (C) and Silica (SiO<sub>2</sub>) nanoparticles suspended in water-based hybrid nanofluid with application in solar collector,” *J. Mol. Liq.*, vol. 357, p. 119134, 2022.
- [21] L. Chen, K. Asai, T. Nonomura, G. Xi, and T. Liu, “A review of Backward-Facing Step (BFS) flow mechanisms, heat transfer and control,” *Therm. Sci. Eng. Prog.*, vol. 6, no. January, pp. 194–216, 2018.
- [22] P. M. Nadge and R. N. Govardhan, “High Reynolds number flow over a backward-facing step: Structure of the mean separation bubble,” *Exp. Fluids*, vol. 55, no. 1, 2014.
- [23] R. Ruisi, H. Zare-Behtash, K. Kontis, and R. Erfani, “Active flow control over a backward-facing step using plasma actuation,” *Acta Astronaut.*, vol. 126, pp. 354–363, 2016.
- [24] Y. Xuan and Q. Li, “Investigation on convective heat transfer and flow features of nanofluids,” *J. Heat Transfer*, vol. 125, no. 1, pp. 151–155, 2003.
- [25] P. K. Namburu, D. K. Das, K. M. Tanguturi, and R. S. Vajjha, “Numerical study of turbulent flow and heat transfer characteristics of nanofluids considering variable properties,” *Int. J. Therm. Sci.*, vol. 48, no. 2, pp. 290–302, 2009.
- [26] A. A. Minea, “Simulation of nanofluids turbulent forced convection at high reynolds number: A comparison study of thermophysical properties influence on heat transfer enhancement,” *Flow, Turbul. Combust.*, vol. 94, no. 3, pp. 555–575, 2015.
- [27] S. El Bécaye Maïga, S. J. Palm, C. T. Nguyen, G. Roy, and N. Galanis, “Heat transfer enhancement by using nanofluids in forced convection flows,” *Int. J. Heat Fluid Flow*, vol. 26, no. 4 SPEC. ISS., pp. 530–546, 2005.
- [28] P. K. Pattnaik, M. M. Bhatti, S. R. Mishra, M. A. Abbas, and O. A. Bég, “Mixed Convective-Radiative Dissipative Magnetized Micropolar Nanofluid Flow over a Stretching Surface in Porous Media with Double Stratification and Chemical Reaction Effects: ADM-Padé Computation,” *J. Math.*, vol. 2022, 2022.
- [29] R. Mashayekhi, E. Khodabandeh, O. A. Akbari, D. Toghraie, M. Bahiraei, and M. Gholami, “CFD analysis of thermal and hydrodynamic characteristics of hybrid nanofluid in a new designed sinusoidal double-layered microchannel heat sink,” *J. Therm. Anal. Calorim.*, vol. 134, no. 3, pp. 2305–2315, 2018.
- [30] J. Koo and C. Kleinstreuer, “Laminar nanofluid flow in microheat-sinks,” *Int. J. Heat Mass Transf.*, vol. 48, no. 13, pp. 2652–2661, 2005.
- [31] M. K. Moraveji, M. Darabi, S. M. H. Haddad, and R. Davarnejad, “Modeling of convective heat transfer of a nanofluid in the developing region of tube flow with computational fluid dynamics,”

- Int. Commun. Heat Mass Transf.*, vol. 38, no. 9, pp. 1291–1295, 2011.
- [32] J. Niu, C. Fu, and W. Tan, “Slip-flow and heat transfer of a non-newtonian nanofluid in a microtube,” *PLoS One*, vol. 7, no. 5, 2012.
- [33] N. Putra, W. Roetzel, and S. K. Das, “Natural convection of nano-fluids,” *Heat Mass Transf. und Stoffuebertragung*, vol. 39, no. 8–9, pp. 775–784, 2003.
- [34] A. K. Santra, S. Sen, and N. Chakraborty, “Study of heat transfer augmentation in a differentially heated square cavity using copper-water nanofluid,” *Int. J. Therm. Sci.*, vol. 47, no. 9, pp. 1113–1122, 2008.
- [35] A. R. Rahmati, O. A. Akbari, A. Marzban, D. Toghraie, R. Karimi, and F. Pourfattah, “Simultaneous investigations the effects of non-Newtonian nanofluid flow in different volume fractions of solid nanoparticles with slip and no-slip boundary conditions,” *Therm. Sci. Eng. Prog.*, vol. 5, no. August 2017, pp. 263–277, 2018.
- [36] Z. Li, P. Barnoon, D. Toghraie, R. Balali Dehkordi, and M. Afrand, “Mixed convection of non-Newtonian nanofluid in an H-shaped cavity with cooler and heater cylinders filled by a porous material: Two phase approach,” *Adv. Powder Technol.*, vol. 30, no. 11, pp. 2666–2685, 2019.
- [37] R. Lotfi, Y. Saboohi, and A. M. Rashidi, “Numerical study of forced convective heat transfer of Nanofluids: Comparison of different approaches,” *Int. Commun. Heat Mass Transf.*, vol. 37, no. 1, pp. 74–78, 2010.
- [38] D. Wen and Y. Ding, “Experimental investigation into convective heat transfer of nanofluids at the entrance region under laminar flow conditions,” *Int. J. Heat Mass Transf.*, vol. 47, no. 24, pp. 5181–5188, 2004.
- [39] M. Akbari, N. Galanis, and A. Behzadmehr, “Comparative analysis of single and two-phase models for CFD studies of nanofluid heat transfer,” *Int. J. Therm. Sci.*, vol. 50, no. 8, pp. 1343–1354, 2011.
- [40] A. Behzadmehr, M. Saffar-Avval, and N. Galanis, “Prediction of turbulent forced convection of a nanofluid in a tube with uniform heat flux using a two phase approach,” *Int. J. Heat Fluid Flow*, vol. 28, no. 2, pp. 211–219, 2007.
- [41] C. T. Nguyen *et al.*, “Viscosity data for Al<sub>2</sub>O<sub>3</sub>-water nanofluid-hysteresis: is heat transfer enhancement using nanofluids reliable?,” *Int. J. Therm. Sci.*, vol. 47, no. 2, pp. 103–111, 2008.
- [42] W. Duangthongsuk and S. Wongwises, “An experimental study on the heat transfer performance and pressure drop of TiO<sub>2</sub>-water nanofluids flowing under a turbulent flow regime,” *Int. J. Heat Mass Transf.*, vol. 53, no. 1–3, pp. 334–344, 2010.
- [43] M. Hemmat Esfe, S. Saedodin, O. Mahian, and S. Wongwises, “Thermophysical properties, heat transfer and pressure drop of COOH-functionalized multi walled carbon nanotubes/water nanofluids,” *Int. Commun. Heat Mass Transf.*, vol. 58, pp. 176–183, 2014.
- [44] S. W. L. Godson, B. Raja, D. Mohan Lal, “Experimental determination of viscosity of water based magnetite nanofluid for application in heating and cooling systems,” *J. Magn. Magn. Mater.*, vol. 417, pp. 243–248, 2016.

- [45] M. Hemmat Esfe, S. Saedodin, and M. Mahmoodi, "Experimental studies on the convective heat transfer performance and thermophysical properties of MgO-water nanofluid under turbulent flow," *Exp. Therm. Fluid Sci.*, vol. 52, pp. 68–78, 2014.
- [46] G. J. Lee, C. K. Kim, M. K. Lee, C. K. Rhee, S. Kim, and C. Kim, "Thermal conductivity enhancement of ZnO nanofluid using a one-step physical method," *Thermochim. Acta*, vol. 542, pp. 24–27, 2012.
- [47] J. Garg *et al.*, "Enhanced thermal conductivity and viscosity of copper nanoparticles in ethylene glycol nanofluid," *J. Appl. Phys.*, vol. 103, no. 7, 2008.
- [48] M. Hemmat Esfe, S. Saedodin, O. Mahian, and S. Wongwises, "Efficiency of ferromagnetic nanoparticles suspended in ethylene glycol for applications in energy devices: Effects of particle size, temperature, and concentration," *Int. Commun. Heat Mass Transf.*, vol. 58, pp. 138–146, 2014.
- [49] R. Singh, O. Sanchez, S. Ghosh, N. Kadimcherla, S. Sen, and G. Balasubramanian, "Viscosity of magnetite-toluene nanofluids: Dependence on temperature and nanoparticle concentration," *Phys. Lett. Sect. A Gen. At. Solid State Phys.*, vol. 379, no. 40–41, pp. 2641–2644, 2015.
- [50] X. Li and C. Zou, "Thermo-physical properties of water and ethylene glycol mixture based SiC nanofluids: An experimental investigation," *Int. J. Heat Mass Transf.*, vol. 101, pp. 412–417, 2016.
- [51] R. Prasher, D. Song, J. Wang, and P. Phelan, "Measurements of nanofluid viscosity and its implications for thermal applications," *Appl. Phys. Lett.*, vol. 89, no. 13, pp. 67–70, 2006.
- [52] M. Nabeel Rashin and J. Hemalatha, "Viscosity studies on novel copper oxide-coconut oil nanofluid," *Exp. Therm. Fluid Sci.*, vol. 48, pp. 67–72, 2013.
- [53] M. Kole and T. K. Dey, "Effect of aggregation on the viscosity of copper oxide-gear oil nanofluids," *Int. J. Therm. Sci.*, vol. 50, no. 9, pp. 1741–1747, 2011.
- [54] S. Halelfadl *et al.*, "Viscosity of carbon nanotubes water based nanofluids : Influence of concentration and temperature," *Int. J. Therm. Sci.*, vol. 71, pp. 111–117, 2013.
- [55] A. Ahmadi Nadooshan, H. Eshgarf, and M. Afrand, "Measuring the viscosity of Fe<sub>3</sub>O<sub>4</sub>-MWCNTs/EG hybrid nanofluid for evaluation of thermal efficiency: Newtonian and non-Newtonian behavior," *J. Mol. Liq.*, vol. 253, no. 2017, pp. 169–177, 2018.
- [56] W. Yu, H. Xie, L. Chen, and Y. Li, "Investigation of thermal conductivity and viscosity of ethylene glycol based ZnO nanofluid," *Thermochim. Acta*, vol. 491, no. 1–2, pp. 92–96, 2009.
- [57] J. Chevalier, O. Tillement, and F. Ayela, "Rheological properties of nanofluids flowing through microchannels," *Appl. Phys. Lett.*, vol. 91, no. 23, pp. 1–4, 2007.
- [58] M. J. Pastoriza-Gallego, C. Casanova, J. L. Legido, and M. M. Piñeiro, "CuO in water nanofluid: Influence of particle size and polydispersity on volumetric behaviour and viscosity," *Fluid Phase Equilib.*, vol. 300, no. 1–2, pp. 188–196, 2011.
- [59] A. Einstein, "Eine neue Bestimmung der Moleküldimensionen," *Ann. Phys.*, vol. 324, no. 2, pp. 289–306, 1906.



- [60] H. C. Brinkman, "The viscosity of concentrated suspensions and solutions," *J. Chem. Phys.*, vol. 20, no. 4, p. 571, 1952.
- [61] I. M. Krieger and T. J. Dougherty, "A Mechanism for Non-Newtonian Flow in Suspensions of Rigid Spheres," *Trans. Soc. Rheol.*, vol. 3, no. 1, pp. 137–152, 1959.
- [62] H. Chen, Y. Ding, and C. Tan, "Rheological behaviour of nanofluids," *New J. Phys.*, vol. 9, 2007.
- [63] N. A. Frankel and A. Acrivos, "On the viscosity of a concentrated suspension of solid spheres," *Chem. Eng. Sci.*, vol. 22, no. 6, pp. 847–853, 1967.
- [64] B. T. S. Lundgren, "Slow flow through stationary random beds and suspensions of spheres," *J. Fluid Mech.*, vol. 51, no. 2, pp. 273–299, 1972.
- [65] G. K. Batchelor, "The effect of Brownian motion on the bulk stress in a suspension of spherical particles," *J. Fluid Mech.*, vol. 83, no. 127, pp. 97–117.
- [66] A.L. Graham, "On the viscosity of a concentrated suspension of solid spheres," *Appl. Sci. Res.*, vol. 37, no. 3, pp. 275–286, 1981.
- [67] Xinwei Wang and Xianfan Xu, "Thermal Conductivity of Nanoparticle–Fluid Mixture," *J. Thermophys. Heat Transf.*, vol. 13, no. 4, pp. 474–480, 1999.
- [68] W. J. Tseng and C. N. Chen, "Effect of polymeric dispersant on rheological behavior of nickel-terpineol suspensions," *Mater. Sci. Eng. A*, vol. 347, no. 1–2, pp. 145–153, 2003.
- [69] C. T. Nguyen *et al.*, "Temperature and particle-size dependent viscosity data for water-based nanofluids - Hysteresis phenomenon," *Int. J. Heat Fluid Flow*, vol. 28, no. 6, pp. 1492–1506, 2007.
- [70] J. Avsec and M. Oblak, "The calculation of thermal conductivity , viscosity and thermodynamic properties for nanofluids on the basis of statistical nanomechanics," *Int. J. Heat Mass Transf.*, vol. 50, no. 0, pp. 4331–4341, 2007.
- [71] N. Cheng and A. W. Law, "Exponential formula for computing effective viscosity," vol. 129, pp. 156–160, 2003.
- [72] N. Masoumi, N. Sohrabi, and A. Behzadmehr, "A new model for calculating the effective viscosity of nanofluids," *J. Phys. D. Appl. Phys.*, vol. 42, p. 055501, 2009.
- [73] D. P. Kulkarni, D. K. Das, and G. A. Chukwu, "Temperature dependent rheological property of copper oxide nanoparticles suspension (nanofluid)," *J. Nanosci. Nanotechnol.*, vol. 6, no. 4, pp. 1150–1154, 2006.
- [74] P. K. Namburu, D. K. Das, K. M. Tanguturi, and R. S. Vajjha, "Numerical study of turbulent flow and heat transfer characteristics of nanofluids considering variable properties," *Int. J. Therm. Sci.*, vol. 48, no. 2, pp. 290–302, 2009.
- [75] A. Karimipour *et al.*, "Synthesized CuFe<sub>2</sub>O<sub>4</sub>/SiO<sub>2</sub> nanocomposites added to water/EG: Evaluation of the thermophysical properties beside sensitivity analysis & EANN," *Int. J. Heat Mass Transf.*, vol. 127, pp. 1169–1179, 2018.
- [76] M. Akbari, M. Afrand, A. Arshi, and A. Karimipour, "An experimental study on rheological behavior of ethylene glycol based nanofluid: Proposing a new correlation as a function of silica

- concentration and temperature,” *J. Mol. Liq.*, vol. 233, pp. 352–357, 2017.
- [77] A. A. A. Alrashed, A. Karimipour, S. A. Bagherzadeh, M. R. Safaei, and M. Afrand, “Electro- and thermophysical properties of water-based nanofluids containing copper ferrite nanoparticles coated with silica: Experimental data, modeling through enhanced ANN and curve fitting,” *Int. J. Heat Mass Transf.*, vol. 127, pp. 925–935, 2018.
- [78] S. Ghasemi and A. Karimipour, “Experimental investigation of the effects of temperature and mass fraction on the dynamic viscosity of CuO-paraffin nanofluid,” *Appl. Therm. Eng.*, vol. 128, pp. 189–197, 2018.
- [79] E. Abu-Nada, “Effects of variable viscosity and thermal conductivity of Al<sub>2</sub>O<sub>3</sub>-water nanofluid on heat transfer enhancement in natural convection,” *Int. J. Heat Fluid Flow*, vol. 30, no. 4, pp. 679–690, 2009.
- [80] M. Hemmat Esfe, S. Saedodin, S. Wongwises, and D. Toghraie, “An experimental study on the effect of diameter on thermal conductivity and dynamic viscosity of Fe/water nanofluids,” *J. Therm. Anal. Calorim.*, vol. 119, no. 3, pp. 1817–1824, 2015.
- [81] W. H. Azmi, K. V. Sharma, R. Mamat, A. B. S. Alias, and I. Izwan Misnon, “Correlations for thermal conductivity and viscosity of water based nanofluids,” *IOP Conf. Ser. Mater. Sci. Eng.*, vol. 36, no. 1, 2012.
- [82] K. Khanafer and K. Vafai, “A critical synthesis of thermophysical characteristics of nanofluid,” *Int. J. Heat Mass Transf.*, vol. 54, no. 19–20, pp. 4410–4428, 2011.
- [83] H. de Bruijn, “The viscosity of suspensions of spherical particles. (The fundamental  $\eta$ - $c$  and  $\phi$  relations),” *Recl. des Trav. Chim. des Pays-Bas*, vol. 61, no. 12, pp. 863–874, 1942.
- [84] V. Vand, “Viscosity of solutions and suspensions. I: Theory,” *J. Phys. Colloid Chem.*, vol. 52, no. 2, pp. 277–299, 1948.
- [85] N. Saitô, “Concentration Dependence of the Viscosity of High Polymer Solutions. I,” *Journal of the Physical Society of Japan*, vol. 5, no. 1, pp. 4–8, 1950.
- [86] D. A. D. and S. L. Passman, “*Theory of multicomponent fluids.*,” Springer Science, 1999.
- [87] J. Buongiorno, “Convective transport in nanofluids,” *J. Heat Transfer*, vol. 128, no. 3, pp. 240–250, 2006.
- [88] B. C. Pak and Y. I. Cho, “Hydrodynamic and heat transfer study of dispersed fluids with submicron metallic oxide particles,” *Exp. Heat Transf.*, vol. 11, no. 2, pp. 151–170, 1998.
- [89] J. Garg *et al.*, “Enhanced thermal conductivity and viscosity of copper nanoparticles in ethylene glycol nanofluid,” *J. Appl. Phys.*, vol. 103, no. 7, pp. 1–6, 2008.
- [90] U. Rea, T. McKrell, L. wen Hu, and J. Buongiorno, “Laminar convective heat transfer and viscous pressure loss of alumina-water and zirconia-water nanofluids,” *Int. J. Heat Mass Transf.*, vol. 52, no. 7–8, pp. 2042–2048, 2009.
- [91] M. Hemmat Esfe, S. Saedodin, O. Mahian, and S. Wongwises, “Heat transfer characteristics and pressure drop of of COOH-functionalized DWCNTs/water nanofluid in turbulent flow at low concentrations,” *Int. J. Heat Mass Transf.*, vol. 73, pp. 186–194, 2014.

- [92] D. A. Anderson, J. C. Tannehill, and R. H. Pletcher, 'Computational fluid mechanics and heat transfer,' 1984." .
- [93] H. K. Versteeg and W. Malalasekera, An introduction to computational fluid dynamics: the finite volume method: Pearson Education, 2007." .
- [94] R. H. Pletcher, J. C. Tannehill, and D. Anderson, Computational fluid mechanics and heat transfer: CRC Press, 2012. .
- [95] J. H. Ferziger and M. Peric, Computational methods for fluid dynamics: Springer Science & Business Media, 2012. .
- [96] Inc ANSYS, "ANSYS Fluent release 15 User ' s Guide," vol. 15317, no. November, pp. 724–746, 2013.
- [97] E. N. Lightfoot, J. Wiley, and A. Ch, "Transport Phenomena," *Psychophysiology*, vol. 16, no. 3. pp. 325–325, 1979.
- [98] A. K. Santra, S. Sen, and N. Chakraborty, "Study of heat transfer due to laminar flow of copper-water nanofluid through two isothermally heated parallel plates," *Int. J. Therm. Sci.*, vol. 48, no. 2, pp. 391–400, 2009.
- [99] I. Behroyan, S. M. Vanaki, P. Ganesan, and R. Saidur, "A comprehensive comparison of various CFD models for convective heat transfer of Al<sub>2</sub>O<sub>3</sub> nano fl uid inside a heated tube ☆," *Int. Commun. Heat Mass Transf.*, vol. 70, pp. 27–37, 2016.
- [100] S. M. Vanaki, P. Ganesan, and H. A. Mohammed, "Numerical study of convective heat transfer of nanofluids: A review," *Renew. Sustain. Energy Rev.*, vol. 54, pp. 1212–1239, 2016.
- [101] S. Kakaç and A. Pramuanjaroenkij, "Review of convective heat transfer enhancement with nanofluids," *Int. J. Heat Mass Transf.*, vol. 52, no. 13–14, pp. 3187–3196, 2009.
- [102] N. Purohit, V. A. Purohit, and K. Purohit, "Assessment of nanofluids for laminar convective heat transfer: A numerical study," *Eng. Sci. Technol. an Int. J.*, vol. 19, no. 1, pp. 574–586, 2016.
- [103] W. J. Minkowycz, E. M. Sparrow, and J. P. Abraham, *NaNoparticle Heat traNsfer aNd fluid flow*, vol. IV. .
- [104] M. Corcione, "Empirical correlating equations for predicting the effective thermal conductivity and dynamic viscosity of nanofluids," *Energy Convers. Manag.*, vol. 52, no. 1, pp. 789–793, 2011.
- [105] "Prandtl, L., in Leipzig: Teubner (in Ludvig Prandtl, Albert Betz: Vier Abhandlungen zur Hydromechanik und Aerodynamik, Go" ttingen: Universitatsverlag, 2010." .
- [106] "Kuznetsov, A.V. and Nield, D.A., Natural Convective Boundary-Layer Flow of a Nanofluid past a Vertical Plate, *Int. J. Thermal Sci.*, 2010, vol. 49, pp. 243–247." .
- [107] "Gingold, H. Modelling fluid flow over solid surfaces. *Int. J. Model. Identif. Control.* 2014, 21, 237." .
- [108] S. Ahmad, A. M. Rohni, and I. Pop, "Blasius and Sakiadis problems in nanofluids," vol. 204, no. November 2010, pp. 195–204, 2011.
- [109] "Bachok, N.; Ishak, A.; Pop, I. Flow and heat transfer characteristics on a moving plate in a nanofluid. *Int. J. Heat Mass Transf.* 2012, 55, 642–648." .

- [110] A. S. Kherbeet, H. A. Mohammed, B. H. Salman, H. E. Ahmed, and O. A. Alawi, "Experimental and numerical study of nanofluid flow and heat transfer over microscale backward-facing step," *Int. J. Heat Mass Transf.*, vol. 79, pp. 858–867, 2014.
- [111] A. M. Abed, M. A. Alghoul, K. Sopian, H. A. Mohammed, H. sh Majdi, and A. N. Al-Shamani, "Design characteristics of corrugated trapezoidal plate heat exchangers using nanofluids," *Chem. Eng. Process. Process Intensif.*, vol. 87, pp. 88–103, 2015.
- [112] K. Lajos, "A.S.H.R.A.E. Handbook, Fundamentals, 111 American Society of Heating, Refrigerating and Air Conditioning Engineers, Atlanta, 2001."
- [113] J. H. Lee *et al.*, "Effective viscosities and thermal conductivities of aqueous nanofluids containing low volume concentrations of Al<sub>2</sub>O<sub>3</sub> nanoparticles," *Int. J. Heat Mass Transf.*, vol. 51, no. 11–12, pp. 2651–2656, 2008.
- [114] A. A. Al-aswadi, H. A. Mohammed, N. H. Shuaib, and A. Campo, "Laminar forced convection flow over a backward facing step using nanofluids," *Int. Commun. Heat Mass Transf.*, vol. 37, no. 8, pp. 950–957, 2010.
- [115] J. Koo and C. Kleinstreuer, "A new thermal conductivity model for nanofluids," *J. Nanoparticle Res.*, vol. 6, no. 6, pp. 577–588, 2004.
- [116] V. Bianco, F. Chiacchio, O. Manca, and S. Nardini, "Numerical investigation of nanofluids forced convection in circular tubes," *Appl. Therm. Eng.*, vol. 29, no. 17–18, pp. 3632–3642, 2009.
- [117] A. K. Hilo, A. R. A. Talib, A. A. Iborra, M. T. H. Sultan, and M. F. A. Hamid, "Experimental study of nanofluids flow and heat transfer over a backward-facing step channel," *Powder Technol.*, vol. 372, pp. 497–505, 2020.
- [118] I. Tavman, A. Turgut, M. Chirtoc, H. P. Schuchmann, and S. Tavman, "Experimental investigation of viscosity and thermal conductivity of suspensions containing nanosized ceramic particles," *Arch. Mater. Sci.*, vol. 34, no. 2, pp. 99–104, 2008.
- [119] M. Jarahnejad *et al.*, "Experimental investigation on viscosity of water-based Al<sub>2</sub>O<sub>3</sub> and TiO<sub>2</sub> nanofluids," *Rheol. Acta*, vol. 54, no. 5, pp. 411–422, 2015.
- [120] M. J. Pastoriza-Gallego, L. Lugo, J. L. Legido, and M. M. Piñeiro, "Thermal conductivity and viscosity measurements of ethylene glycol-based al<sub>2</sub>o<sub>3</sub> nanofluids," *Nanoscale Res. Lett.*, vol. 6, no. 1, pp. 1–11, 2011.
- [121] L. Syam Sundar, E. Venkata Ramana, M. K. Singh, and A. C. M. Sousa, "Thermal conductivity and viscosity of stabilized ethylene glycol and water mixture Al<sub>2</sub>O<sub>3</sub> nanofluids for heat transfer applications: An experimental study," *Int. Commun. Heat Mass Transf.*, vol. 56, pp. 86–95, 2014.
- [122] J. B. Mena, A. A. Ubices De Moraes, Y. R. Benito, G. Ribatski, and J. A. R. Parise, "Extrapolation of Al<sub>2</sub>O<sub>3</sub>-water nanofluid viscosity for temperatures and volume concentrations beyond the range of validity of existing correlations," *Appl. Therm. Eng.*, vol. 51, no. 1–2, pp. 1092–1097, 2013.
- [123] H. Khodadadi, D. Toghraie, and A. Karimipour, "Effects of nanoparticles to present a statistical model for the viscosity of MgO-Water nanofluid," *Powder Technol.*, vol. 342, pp. 166–180, 2019.

- [124] S. W. Lee, S. D. Park, S. Kang, I. C. Bang, and J. H. Kim, “Investigation of viscosity and thermal conductivity of SiC nanofluids for heat transfer applications,” *Int. J. Heat Mass Transf.*, vol. 54, no. 1–3, pp. 433–438, 2011.
- [125] A. S. Dalkilic *et al.*, “Prediction of graphite nanofluids’ dynamic viscosity by means of artificial neural networks,” *Int. Commun. Heat Mass Transf.*, vol. 73, pp. 33–42, 2016.
- [126] A. Turgut, I. Tavman, M. Chirtoc, H. P. Schuchmann, C. Sauter, and S. Tavman, “Thermal conductivity and viscosity measurements of water-based TiO<sub>2</sub> nanofluids,” *Int. J. Thermophys.*, vol. 30, no. 4, pp. 1213–1226, 2009.
- [127] B. Ilhan, M. Kurt, and H. Ertürk, “Experimental investigation of heat transfer enhancement and viscosity change of hBN nanofluids,” *Exp. Therm. Fluid Sci.*, vol. 77, pp. 272–283, 2016.
- [128] M. Nabeel Rashin and J. Hemalatha, “Synthesis and viscosity studies of novel ecofriendly ZnO-coconut oil nanofluid,” *Exp. Therm. Fluid Sci.*, vol. 51, pp. 312–318, 2013.
- [129] M. J. Pastoriza-Gallego, L. Lugo, D. Cabaleiro, J. L. Legido, and M. M. Piñeiro, “Thermophysical profile of ethylene glycol-based ZnO nanofluids,” *J. Chem. Thermodyn.*, vol. 73, no. February, pp. 23–30, 2014.
- [130] G. Zyla and J. Fal, “Experimental studies on viscosity, thermal and electrical conductivity of aluminum nitride-ethylene glycol (AlN-EG) nanofluids,” *Thermochim. Acta*, vol. 637, pp. 11–16, 2016.
- [131] L. Godson, B. Raja, D. M. Lal, And, and S. Wongwises, “Experimental investigation on the thermal conductivity and viscosity of silver-deionized water nanofluid,” *Exp. Heat Transf. A J. Therm. Energy Gener. Transp. Storage, Convers.*, no. March, pp. 37–41, 2015.
- [132] Y. Ding, H. Alias, D. Wen, and R. A. Williams, “Heat transfer of aqueous suspensions of carbon nanotubes (CNT nanofluids),” *Int. J. Heat Mass Transf.*, vol. 49, no. 1–2, pp. 240–250, 2006.
- [133] M. Baratpour, A. Karimipour, M. Afrand, and S. Wongwises, “Effects of temperature and concentration on the viscosity of nanofluids made of single-wall carbon nanotubes in ethylene glycol,” *Int. Commun. Heat Mass Transf.*, vol. 74, pp. 108–113, 2016.
- [134] H. Zhu, C. Li, D. Wu, C. Zhang, and Y. Yin, “Preparation, characterization, viscosity and thermal conductivity of CaCO<sub>3</sub> aqueous nanofluids,” *Sci. China Technol. Sci.*, vol. 53, no. 2, pp. 360–368, 2010.
- [135] W. Yu and S. U. S. Choi, “The role of interfacial layers in the enhanced thermal conductivity of nanofluids: A renovated Hamilton-Crosser model,” *J. Nanoparticle Res.*, vol. 6, no. 4, pp. 355–361, 2004.

## LIST OF PUBLICATIONS RELATED TO THE TOPIC OF THE RESEARCH FIELD

**LIST OF PUBLICATIONS RELATED TO THE TOPIC OF THE RESEARCH FIELD**

- K1.** M. Klazly and G. Bognár, A novel empirical equation for the effective viscosity of nanofluids based on theoretical and empirical results. *International Communications in Heat and Mass Transfer*, vol. 135, 106054, 2022.
- K2.** M. Klazly and G. Bognár, Quantitative comparison of CFD models for convective heat transfer of nanofluid in backward facing step, *Journal of Molecular Liquids*, 119607, 2022.
- K3.** M. Klazly and G. Bognár, Heat transfer enhancement for nanofluid flows over a microscale backward-facing step, *Alexandria Eng. J.*, vol. 61, no. 10, pp. 8161–8176, 2022.
- K4.** G. Bognár, M. Klazly, and K. Hriczó, Nanofluid flow past a stretching plate, *Processes*, vol. 8, no. 7, 2020.
- K5.** M. Klazly and Hriczó K., The heat and mass transfer in blasius and sakiadis nanofluid flows, *AIP Conference Proceedings* vol. 2425, 290004, 2022.
- K6.** M. M. Klazly, G. Bognár and K. Hriczó, Heat and mass transfer for Al<sub>2</sub>O<sub>3</sub> nanofluid in a duct, *AIP Conference Proceedings* vol. 2425, 290005, 564–574, 2022.
- K7.** G. Bognár, M. Klazly, U. S. Mahabaleshwar, G. Lorenzini, and K. Hriczó, Comparison of Similarity and Computational Fluid Dynamics Solutions for Blasius Flow of Nanofluid, *J. Eng. Thermophys.*, vol. 30, no. 3, pp. 461–475, 2021.
- K8.** M. Klazly and G. Bognár, CFD study for the flow behaviour of nanofluid flow over flat plate, *Int. J. Mech.*, vol. 14, pp. 49–57, 2020.
- K9.** M. Klazly and G. Bognár, CFD investigation of backward - Facing step nanofluid flow, *J. Phys. Conf. Ser.*, vol. 1564, no. 1, 2020.
- K10.** M. Klazly and G. Bognár, Investigation of convective heat transfer enhancement for nanofluid flow over flat plate, *J. Phys. Conf. Ser.*, vol. 1564, no. 1, 2020.
- K11.** M. Klazly and G. Bognár, Comparison of Sakiadis and Blasius flows using Computational Fluid Dynamic. In *Solutions for Sustainable Development: Proceedings of the 1st International Conference on Engineering Solutions for Sustainable D.* ICES2D 2019, pp. 129–138, 2019.
- K12.** M. Klazly and G. Bognár, Computational Fluid Dynamic Simulation of Laminar Flow Over a Flat Plate, *Design Machines Structures*, vol. 9, no. 1, pp. 29–47,